High-resolution model studies of the circulation in coastal areas of the Tyrrhenian Sea (including the Gulf of Naples)

PH.D. THESIS

UNIVERSITÁ DEGLI STUDI DI NAPOLI "FEDERICO II"
SCUOLA DI DOTTORATO IN SCIENZE DELLA TERRA "GIUSEPPE DE LORENZO"

Jointly with:

Universitá degli Studi di Napoli "Parthenope"
Seconda Universitá di Napoli

In collaboration with:

Istituto per l'Ambiente Marino Costiero - C. N. R.
Stazione Zoologica Anton Dohrn

Ph.D. Candidate: Paola de Ruggiero

Tutor: Prof. Stefano Pierini

Co-tutor: Prof. Giancarlo Spezie

Ph.D. School Director: Prof. Alberto Incoronato

April, 2013

Di questo mare amo piú di ogni
altra cosa la parte tirrenica,
quella che va dalle coste della
Sardegna, tocca il Circeo e le Pontine,
e balza a Miseno, e da lí, dopo
Ischia Procida e Capri,
lungo la penisola sorrentina arriva
fino a Palinuro e fino alle isole Eolie.
É il mare di Odisseo, il mare
divino piú grego del greco mare.
É questa la mia regione
dell'anima, qui sono stato smemorato,
felice di non essere niente, qui mi
sono sentito come il ciottolo
che rotola sulla spiaggia
e di cui nessuno sa.

Raffaele La Capria, L'armonia perduta

Contents

Preface

Understanding the dynamics of coastal waters is a very relevant issue not only from the physical oceanographic viewpoint, but also in a more general environmental perspective, as coherent and turbulent motions near the coasts affect the dispersion of pollutants, the water quality, the local ecology and, indirectly, social and economic aspects, especially in highly populated coastal zones. The application of state-of-the-art ocean circulation models to coastal environments is fundamental to this respect. If properly implemented, these theoretical tools can provide a synoptic picture of the local ocean climate and can describe typical dynamic scenarios; moreover, models can even allow to forecast the sea state, especially if data assimilation is included in the treatment.

In this context, the implementation of a high-resolution general circulation model (the Princeton Ocean Model) in a significant Mediterranean coastal site, and its experimental validation have been the main objects of this PhD research activity.

The main scientific aim is to simulate the circulation in the Gulf of Naples with a high-resolution model nested with a Tyrrhenian Sea circulation model. This is a highly innovative approach compared to previous studies on the same coastal area. This work aims at investigating the local role played by the wind forcing and by the remote forcing provided by the Tyrrhenian Sea

circulation. This in turn will allow us to improve our understanding of the marine dynamics in the Gulf of Naples.

This modeling approach is a good starting point to describe and analyze in detail a series of dynamical scenarios, to identify typical circulation patterns and variability for the different seasons, and to investigate the sensitivity of the model response to changes in several parameters, setups and forcing. In addition, the analysis of the role played by the large-scale circulation in the coastal area, and the study of the model sensitivity to the use of different wind products are other important tasks that have been achieved.

The test site chosen for this study is a coastal area located in the Tyrrhenian Sea, a western Mediterranean sub-basin where very relevant oceanographic processes take place. The basin scale circulation yields an important interannual variability shaped by a strong seasonal cycle and energetic mesoscale features (e.g., Artale et al., 1994; Pierini and Simioli, 1998; Schroeder et al., 2008; Vetrano et al., 2010). Local driving mechanisms are the heat, evaporative and momentum fluxes at the air-sea interface, while an important remote forcing is provided by the fluxes of modified Atlantic and Levantine intermediate water masses through the Sardinia and Sicily straits (e.g., Pierini, 1996; Pierini and Rubino, 2001; Molcard et al., 2002; Napolitano et al., 2003; Béranger et al., 2004; Gabersek et al., 2007). In the southeastern Tyrrhenian Sea a small semi-enclosed basin, the Gulf of Naples, is present: this is a very interesting zone, not only because it is ideal in terms of physical processes occurring in such a regular geometry, but also from environmental, social and economic viewpoints. The local circulation was analyzed both through experimental (De Maio et al., 1983, 1985) and modeling studies (e.g., Gravili et al., 2001; Grieco et al., 2005; Pierini et al., 2004, 2005). In this context, the modeling study presented here applies to the same

coastal area: more precisely, it includes the adjacent gulfs of Gaeta, Naples and Salerno, plus a wide buffer zone of the Tyrrhenian Sea.

The content of this thesis is now briefly summarized.

- Chapter 1 is a review of the oceanographic knowledge of the circulation of the Tyrrhenian Sea, of its southern part and of the Gulf of Naples in particular. Both observational and modeling studies are reviewed.

- Chapter 2 focuses on the main physical, mathematical and numerical aspects of the Princeton Ocean Model.

- In Chapter 3 the properties of ECMWF surface wind data used to force the model are discussed. The retrieval of an alternative wind product derived from X-band COSMO-SkyMed Synthetic Aperture Radar data is also considered; comparison with ECMWF and satellite scatterometer (ASCAT) data is finally presented.

- In Chapter 4 the implementation of the model in our coastal test area is described. Several error tests and the one-way nesting with a large-scale Tyrrhenian Sea circulation model are also described in detail.

- In Chapter 5 several simulations in different circulation scenarios are presented. An analysis of COSMO-SkyMed SAR wind forcing capabilities is finally discussed.

- In Chapter 6 an experimental validation of our coastal circulation model with current meter measurements is described.
  This validation is achieved in a simulation that evidences the propagation of a Kelvin wave generated by the relaxation of an upwelling event. A preliminary validation with CODAR data is finally presented.

Chapter 1

The South Tyrrhenian Sea circulation

1.1 Introduction

In this chapter the problem of the marine circulation in the Tyrrhenian Sea in general, and in a southern Tyrrhenian coastal area in particular, will be considered. Both observations and modeling results will be presented and discussed. Particular attention will be devoted to the coastal area that is chosen as our test site for the subsequent modeling applications.

1.2 The Tyrrhenian Sea circulation: observation and modeling

The test site chosen for this study is a coastal area located in the Tyrrhenian Sea, a western Mediterranean sub-basin where very relevant oceanographic processes take place. The Tyrrhenian Sea (fig.1.1), the western arm of the Mediterranean Sea, exchanges water with the whole Mediterranean

basin through the Sardinia Channel, the Sicily Strait and the Corsica Channel, that represent morphologic constraints for the circulation of intermediate and deep water (Millot, 1987, Astraldi et al., 1994, and Artale et al., 1994). The surface water (0-200 m), entering the Tyrrhenian Sea through the

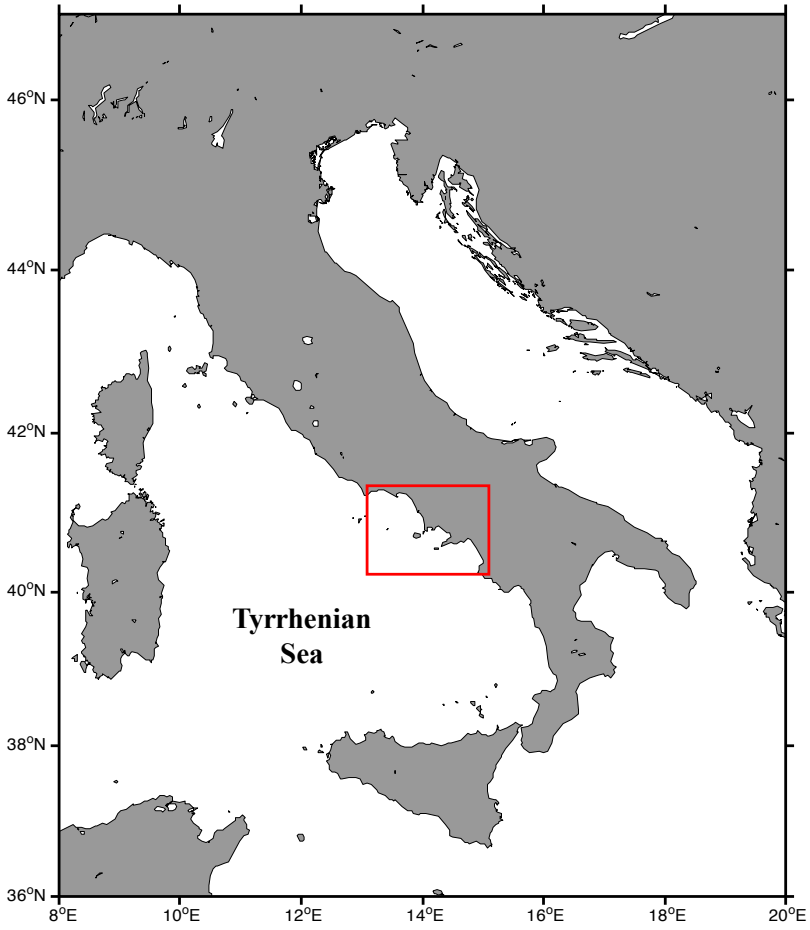

Figure 1.1: The Tyrrhenian Sea and the south Tyrrhenian coastal test area (red rectangle).

Sardinia Channel, is the Modified Atlantic Water (MAW) from the Algerian Current (AC). The MAW is characterized by low salinity (on average less than 38 psu), and flows cyclonically along the Italian coasts; through the Sicily Strait and deeper than 200 m down to about 700 m, the basin receives the Levantine Intermediate Water (LIW), which is marked by a subsurface

temperature maximum and by higher salinity (on average 38.8 psu), and mixes with the surface MAW and deeper water masses. From about 700 m to the bottom the Tyrrhenian Deep Water (TDW) is present, being the result of the modification of the West Mediterranean Deep Water (WMDW) that crosses the Sardinia Channel.

The basin scale circulation yields an important interannual variability shaped by a strong seasonal cycle and energetic mesoscale features (e.g., see Artale et al., 1994; Pierini and Simioli, 1998; Schroeder et al., 2008; Vetrano et al., 2010). Local driving mechanisms are the heat, evaporative and momentum fluxes at the air-sea interface, while an important remote forcing is provided by the fluxes of modified Atlantic and Levantine intermediate water masses through the Sardinia and Sicily straits (e.g., Pierini and Rubino, 2001; Molcard et al., 2002; Napolitano et al., 2003; Béranger et al., 2004; Gabersek et al., 2007).

In relation with the main circulation patterns, two broad regions can be defined on the basis of prevailing dynamic conditions. The northern and central parts of the basin are mostly influenced by the wind blowing year-round eastward from the Strait of Bonifacio. This jet-like force excites important quasi-stationary counter-rotating gyres that enhance the vertical component of motion in the sea. In contrast, apart from the direct atmospheric forcing, the southern part of the basin appears to be under the influence of forces outside of the sea, which are conveyed through the southern opening. The seasonal intrusions of the MAW appear to play a major role in this regard. In winter, the surface flow is seen to progress along the eastern Tyrrhenian coast as far as the Corsica Channel. Actually, translating through the channel into the Ligurian Provençal Sea and to the Gulf of Lions, this flow provides a strong link in the circulation of the two basins.

In addition, it modulates the effect of the wind-induced structures in the northern part. In summer the MAW does not leave the Tyrrhenian northward. Probably due to topographic effects, the LIW presents a much more complicated pattern, with a seasonal oscillation not as evident. While its circulation involves the whole basin, the inflow/outflow is mostly throughout the southern opening. Since it mixes with both the surface water and the deep water, the Levantine Intermediate Water plays an essential role in the vertical exchanges inside the basins. The lack of suitable data does not permit an adequate description of the Tyrrhenian deep water circulation pattern. Certainly its inflow is in the deepest part of the Sardinia-Sicily opening, while the outflow of a deep/intermediate mixed water occurs immediately above, throughout the same opening (Astraldi et al., 1994).

The Tyrrhenian Sea dynamics shows a pronounced barotropic component. An almost basin-wide cyclonic circulation at all depths is present during winter, accompanied by a highly barotropic northward flow through the Corsica Channel and by a northeastward flow of LIW through the Sicily channel joined by a flow of modified AW coming from the Sardinia channel, which then follows the same cyclonic motion; in late spring and in summer, a remarkable weakening and a local reversal of the flow is observed (e.g., Krivosheya and Ovchinnikov, 1973; Millot, 1987; Astraldi and Gasparini, 1992, 1994; Astraldi et al., 1994).

The importance of the barotropic component in the Tyrrhenian circulation suggests that the wind is likely to play a major role as a forcing agent; recent studies (Napolitano et al., 2013) show that the barotropic component also influences the intermediate circulation of the Tyrrhenian Sea. In the process-oriented model study of Pierini and Simioli, 1998 the interaction between the wind-driven dynamics in the straits of Corsica, Sicily and Sar-

dinia and that in the interior of the Tyrrhenian Sea was analyzed through the implementation of a shallow water model forced by "National Meteorological Center" (NMC) winds. The Tyrrhenian wind-driven dynamics appears to be mainly forced by the local winds; a predominant northward flux is found in the periods January-April and October-December, while a predominant but weaker southward flux can be observed in the rest of the year. To this respect, the seasonal variability is studied in a 'closed' Tyrrhenian Sea and is then compared with that obtained in the framework of the whole Mediterranean. Fig.s 1.2 and 1.3 show the comparison between the two responses on January 31 and June 30, respectively. The flows are virtually identical in the interior while they obviously differ near the straits.

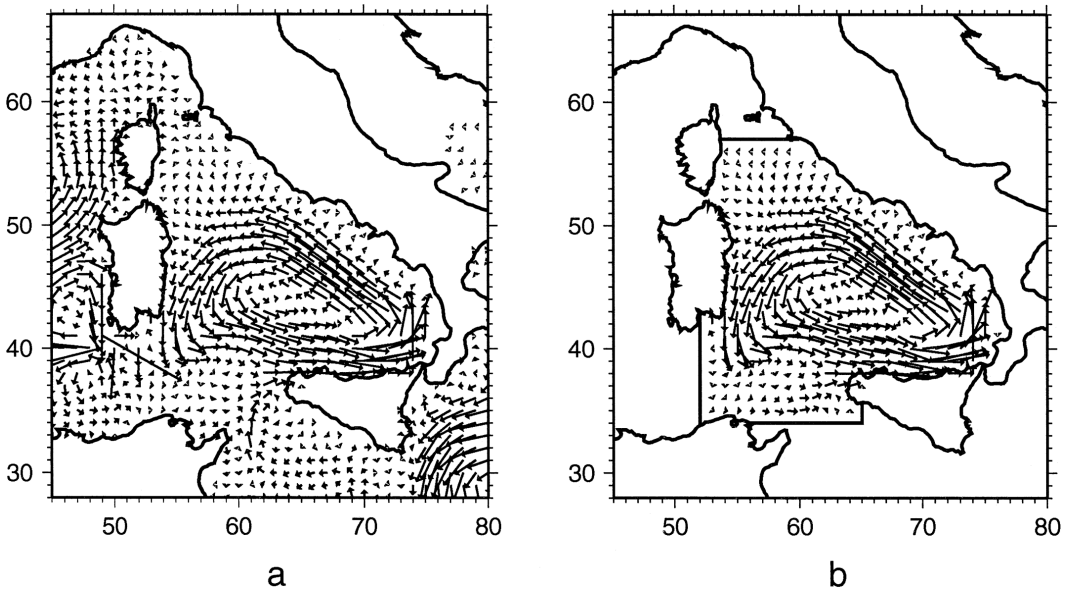

Figure 1.2: Filtered perpetual transports on June 30 for the open (a) and closed (b) Tyrrhenian Sea case (from Pierini and Simioli, 1998).

In the same model study the rapid fluctuations that the wind is able to induce in the ocean were analyzed as well. The instantaneous currents obtained by forcing the model with daily winds were found to be up to 10

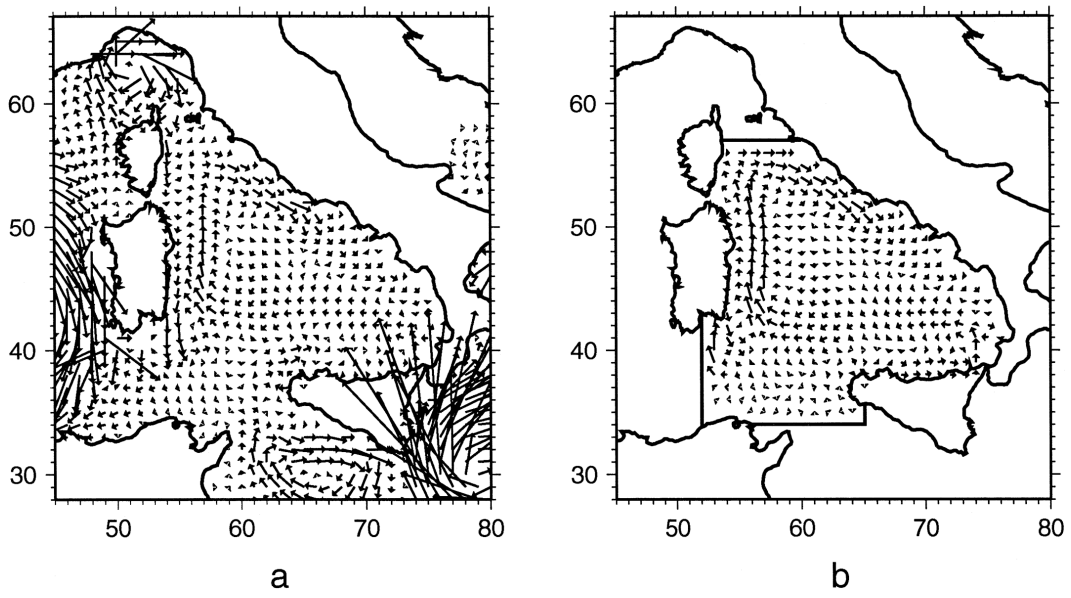

Figure 1.3: Filtered perpetual transports on January 31 for the open (a) and closed (b) Tyrrhenian Sea case (from Pierini and Simioli, 1998).

times larger than the corresponding climatological ones, with episodes of reversal over a period of few days (e.g., Fig.1.4). The experimental evidence of the existence of these rapid wind-driven fluctuations was also discussed. The analysis of the daily variability provides a realistic picture of the character of the wind-driven circulation in the Tyrrhenian Sea that differs considerably from the classical seasonal dynamics.

In order to analyze the remotely-forced baroclinic dynamics in the Tyrrhenian Sea, a high-resolution multilayer numerical model was implemented by Pierini and Rubino (2001) in a central Mediterranean region including the Tyrrhenian and the Ionian Seas. Three layers were considered representing waters of Atlantic origin (MAW), the LIW, and the Mediterranean deep waters. Quasi-stationary circulations representing the local manifestation of the large-scale Mediterranean conveyor belt are obtained [after an adjustment time of O(2 months)] by imposing steady fluxes along the remote open boundaries, in the absence of meteorological forcings (Fig.1.5).

These circulations can be interpreted as possible dynamic scenarios of the seasonal variability. In the numerical simulations an inflow of MAW and an outflow of LIW through the Strait of Sardinia, an outflow of MAW and an inflow of LIW through the Ionian boundary, and an outflow of MAW through the Corsica channel are imposed, resulting in a vanishing total net transport in each layer. For realistic values of these transports the model captures the main features of the observed circulation, such as (i) the separation of the Algerian Current into two branches, one directed toward the Tyrrhenian Sea and the other entering the strait; (ii) a secondary bifurcation of MAW within the strait giving rise to a southward-moving current that follows the Tunisian continental slope and to a current that flows southeastward along the southern Sicilian coast and then northward along the southern Italian coasts (the so-called Atlantic-Ionian Stream); (iii) a bifurcation of LIW at the strait level leading to a main current directed toward the Strait of Sardinia and to a weaker current that, after having crossed the strait, bends eastward and enters the Tyrrhenian Sea (e.g., Fig. 1.6).

Sensitivity experiments carried out by imposing different boundary fluxes have shed light on the functioning of the MAW and LIW bifurcations. First of all, for a given net transport of MAW and LIW through the strait (imposed indirectly by the boundary fluxes), the ratio R_{maw} between the transport of MAW entering the Tyrrhenian Sea and that entering the strait is found to be virtually independent of the boundary-imposed Algerian Current transport. It is, on the contrary, determined by a local dynamic control, which selects the value $R_{mav} \simeq 0.43$ for a net MAW/LIW strait transport of 61 Sv, in excellent agreement with observations. Second, for decreasing baroclinic transports the ratio R_{maw} is found to decrease up to the limiting value $R_{maw} \simeq 0.2$ (corresponding to the linear regime) for transports < O(0.1 Sv).

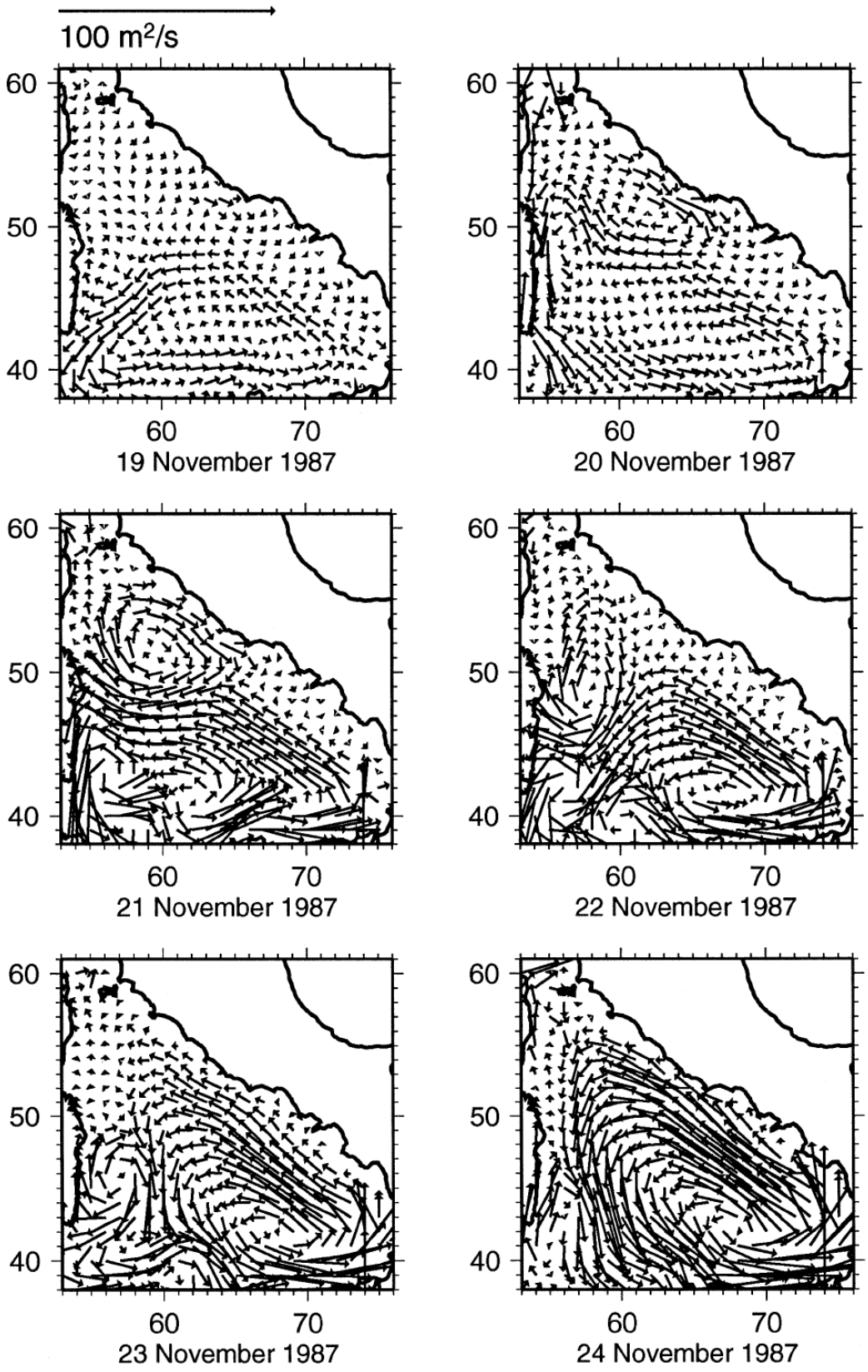

Figure 1.4: Snapshots of instantaneous transports during a week in Autumn 1987 (from Pierini and Simioli, 1998).

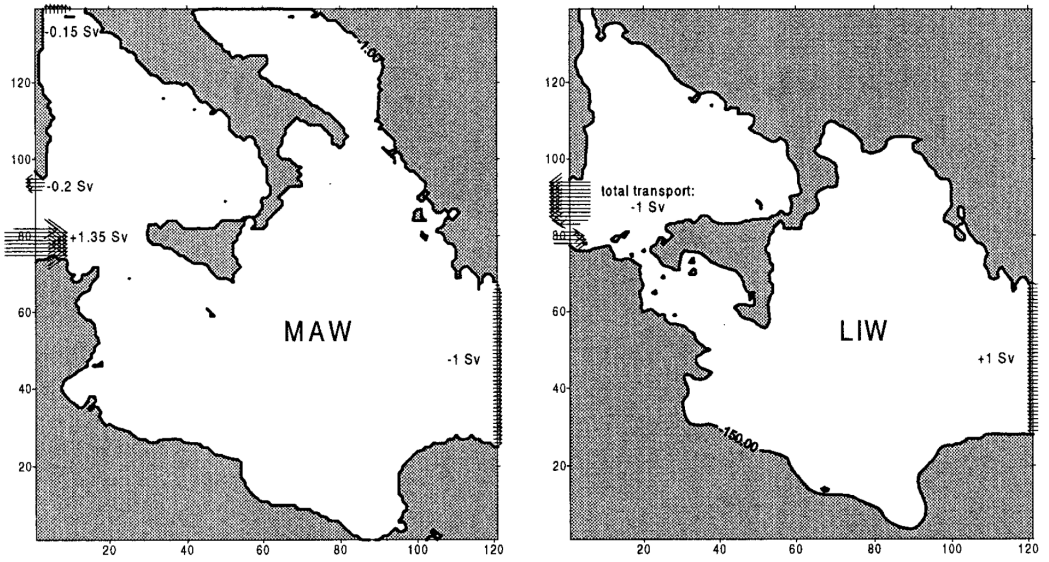

Figure 1.5: Boundary conditions imposed for the MAW and LIW layers (from Pierini and Rubino, 2001).

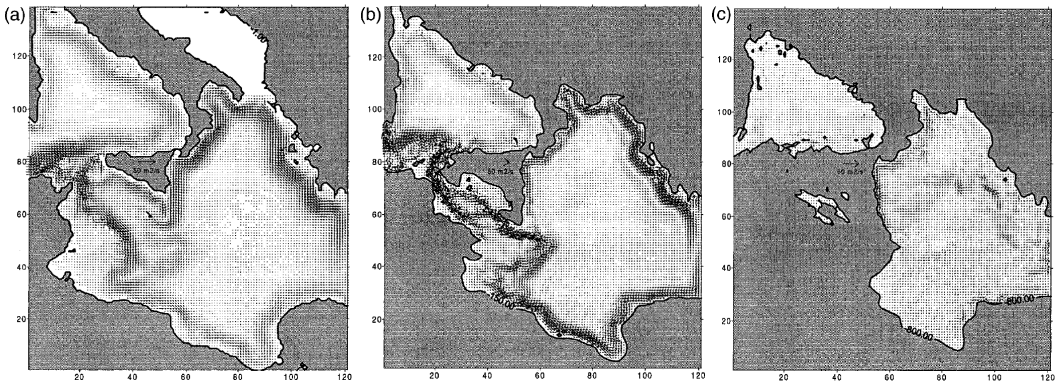

Figure 1.6: Typical MAW and LIW flows obtained with boundary forcing (from Pierini and Rubino, 2001).

Finally, R_{maw} is found to be very sensitive to the barotropic transport T through the strait, whereas the corresponding ratio for the LIW, Rliw, is virtually independent of T. For T = -0.5 Sv, $R_{maw} \simeq 1.1$ while for T = + 0.5 Sv, R_{maw} decreases by one order of magnitude: $R_{maw} \simeq 0.1$. In other words, a weakening of the LIW (or a strengthening of the MAW) net transport through the strait reduces the relative intensity of the Tyrrhenian branch of MAW, and vice versa. On the other hand, for values of T within the same range one always finds $R_{liw} \simeq -0.3$. It thus appears that the local control exerted by the topography through the LIW potential vorticity budget forces the transport of the Tyrrhenian branch of LIW to be always $\simeq 1/3$ of that directed toward the Strait of Sardinia.

The role of the remote forcing played by adjacent basins on the Tyrrhenian Sea circulation was also investigated by Napolitano et al. (2003). In particular, the effect of stratification in shaping the Tyrrhenian seasonal circulation was investigated through a high resolution, primitive equation, sigma coordinate model. The work focused on the purely baroclinic dynamics and on its sensitivity to seasonal stratification, thus no atmospheric forcing was used (as in Pierini and Rubino, 2001). Two numerical experiments were carried out, with initial conditions given by diagnostic velocity fields derived from the winter and summer climatological hydrologies.The quasi-steady state is characterized by circulation patterns (in the depth range of the MAW and the LIW) that are found to be strongly controlled by mesoscale eddies and topography. Seasonal difference is found in the surface current which exhibits the major variability on the African side, downstream of Adventure Bank and the Ionian Slope, where the absolute maximum occurs. The intermediate circulation instead does not show relevant seasonal differences. LIW enters through the two passages south of

Malta Plateau and preferentially flows along the Sicilian shelf edge exiting over the northern sill. Its pathway is strongly controlled by subsurface cyclonic and anticyclonic cells. The results are also found to be in good agreement with observations. Fig. 1.7 shows examples of prognostic circulation fields for winter and summer conditions.

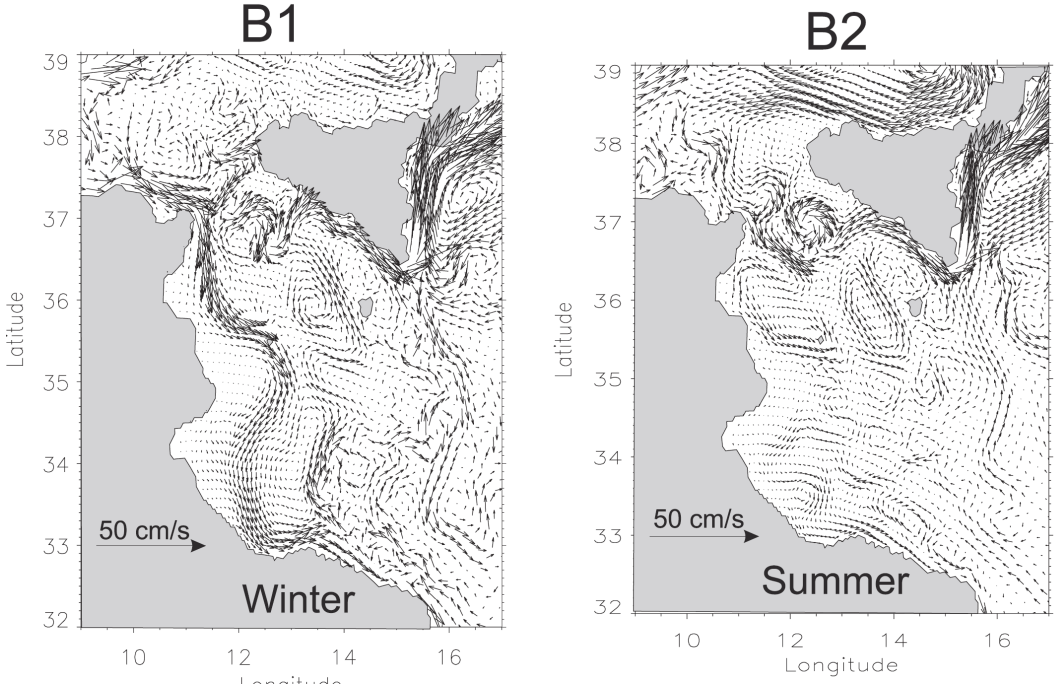

Figure 1.7: Quasi-steady prognostic circulation fields at 30 m-depth for winter (B1) and summer (B2) conditions (from Napolitano et al., 2003).

Hydrological and current measurements collected in the Tyrrhenian Sea during May-June 2004 were analyzed by Vetrano et al., 2010. with an inverse box model (IBM) to establish the mean circulation patterns of the basin during spring 2004. These patterns are compared with those provided by the POM implemented over the area to simulate the mean basin circulation during the survey. The results are in good agreement with the current measurements. In the modeling study conducted by Napolitano et al., 2013., the hindcasts relative to the year 2009 produced by a high-resolution operational ocean model show that the dynamics in the surface and interme-

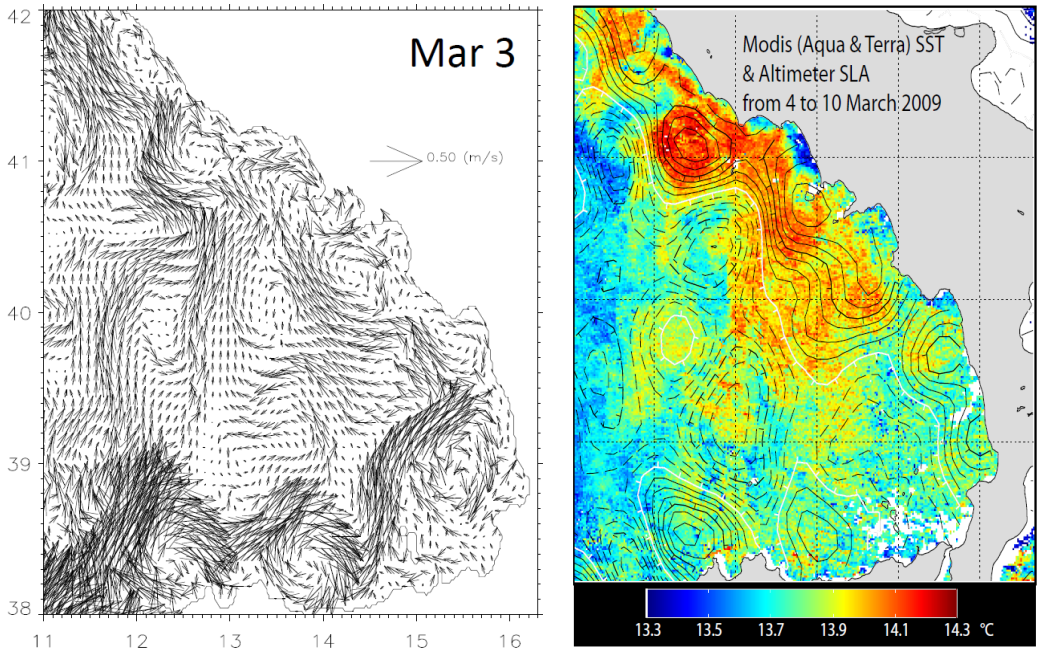

Figure 1.8: Left panel: weekly averaged simulated velocity fields at 10 m. Right panel: sea level anomaly as observed from altimetry for the week 4-10 March (contours), with the sea surface temperature (colors) of the same week superposed (adapted from Napolitano et al., 2013).

diate layers are strongly coupled, and display marked seasonal variations. The Tyrrhenian Sea circulation organizes around several well-defined quasi-permanent gyres (Fig. 1.8). Comparison with altimeter data suggests that these gyres are robust features, especially in winter and spring.

1.3 The South Tyrrhenian coastal area including the Gulf of Naples

Among the numerous coastal areas of the Mediterranean Sea, the South Tyrrhenian area shown in Fig. 1.1, which includes the Gulf of Naples and the nearby gulfs of Gaeta and Salerno, is probably one of the most challenging and fascinating coastal zones of the Mediterranean Sea. The Gulf of

Naples in particular (Fig. 1.9), is a very interesting zone, also already discussed. The marine dynamics in the Gulf of Naples determines the advec-

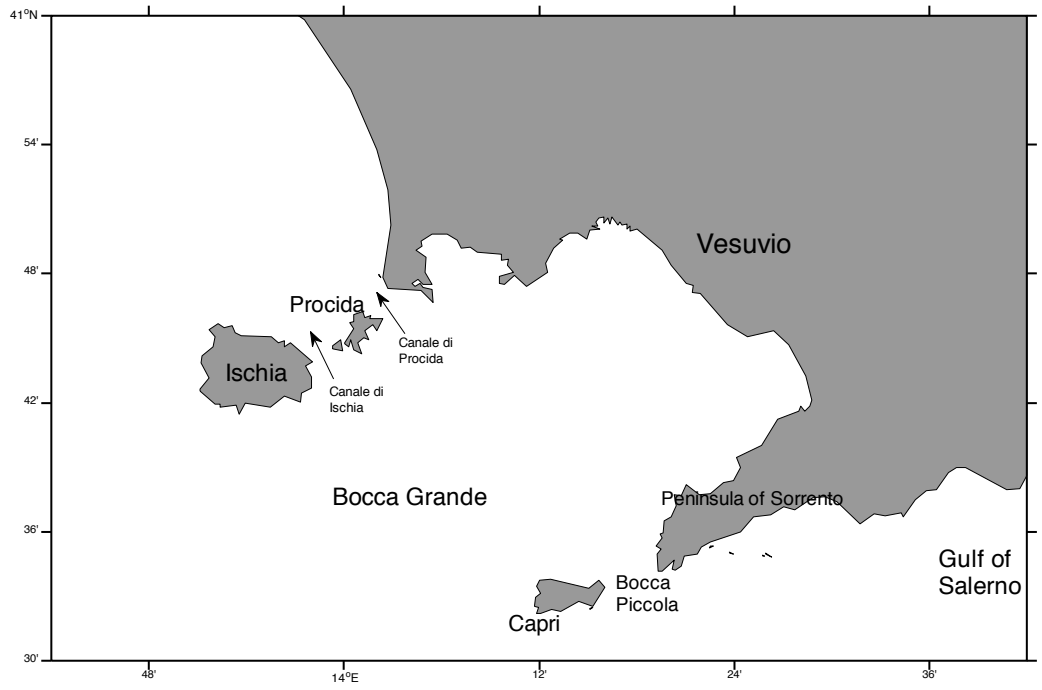

Figure 1.9: The Gulf of Naples, with its channels and islands.

tion and diffusion of marine pollutants, and therefore plays a fundamental role for the monitoring needs of the coastal marine environment, and for solving problems related to water basin pollution. The Gulf of Naples is affected by significant degradations, especially along the coast, that affect the local economy and environment; the strong pressure due to agricultural and industrial activities, in addition to the high population density, have resulted in the general deterioration of the marine environment, and have exacerbated problems such as coastal erosion, the pathogenic bacteria spread, toxic substances spills, and so on. To this respect, monitoring, understanding and modeling the circulation of waters in this gulf is of fundamental importance. This has led us to focus our attention on this specific coastal site, in which, moreover, many observations are available (see the remain-

ing part of the chapter) that allow one to validate model implementations.

The gulf is limited by the islands of Ischia and Procida and the Phlaegrean Fields in the northern part, and by the island of Capri and the Sorrento peninsula in the southern part, and covers an area of about 900 km^2 characterized by a mean depth of about 170 m. The interior waters of the Gulf of Naples are in direct communication with the Tyrrhenian Sea trough two main openings: the Bocca Grande, which separates Ischia Island from Capri Island, and the Bocca Piccola, a narrow opening located between Capri and Punta Campanella (the southernmost part of the Sorrento Peninsula). Two more openings are present: the Procida Channel (with a shallow sills of 12 m) separating Procida Island and the coast, and the Ischia Channel (with shallow sills of 22 m) separating the Ischia and Procida Islands. These two channels connect the Gulf of Naples with the Gulf of Gaeta to the North.

The Gulf of Naples bathymetry (Fig. 1.10) presents very specific features. The Bocca Grande is characterized by the presence of two canyons (Magnaghi and Dohrn) where the water depth reaches 800 m. The Bocca Piccola (whose depth is about 70 m) slopes down very sharply to 1000 m toward the Gulf of Salerno. The Magnaghi and Dohrn canyons engrave the continental slope and are located in the western and eastern sector respectively. Both canyons are NE-SW oriented: the Magnaghi canyon develops in the north-western volcanic zone between Capo Miseno and Ischia, while the Dohrn canyon (with a depth greater than 150 m, a length of about 25 km and a width of about 2 km) extends across the Bocca Grande, where it branches off towards the coast. The northern branch of the Dohrn canyon develops over the continental shelf originating the Ammontatura channel, while the southern one extends towards the Procida coastline. Both canyons control the vertical fluxes acting as a conduit for transport of sediment from

the shelf to the slope (e.g., Cianelli et al., 2011). In the region between the Magnaghi and the Dorn canyon there is a bank, the so-called "secca delle vedove", with a depth of about 150 m (Fig. 1.10).

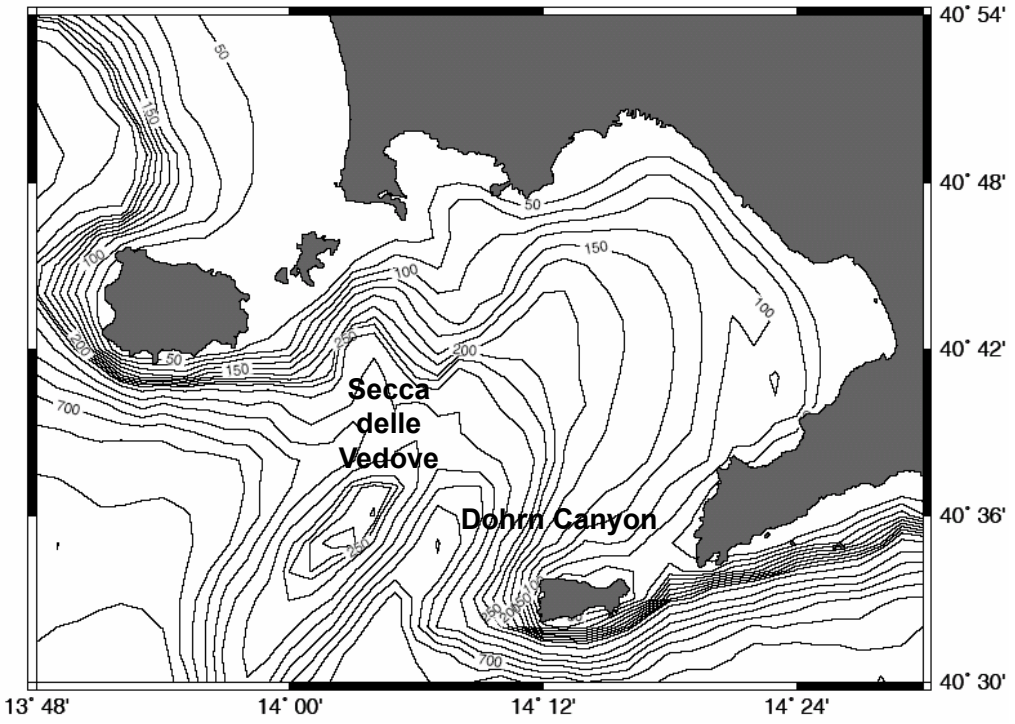

Figure 1.10: The Gulf of Naples bathymetry (Menna et al., 2008).

From the morphological viewpoint, the gulf can be divided into two sectors: the south-eastern part of carbonate (Sorrento peninsula and Capri) and alluvial (the mud flat of Sarno river) nature, and the north-western part of volcanic nature (Campi Flegrei, Ischia and Procida), characterized by the presence of banks and submarine canyons.

The study area is also characterized by peculiar orographic aspects influencing the wind and sea dynamics (Fig. 1.11). In the proximity of the NE coast of the gulf, the Vesuvius volcano is located (with an elevation of 1281 m), and the area around the city of Naples is punctuated by numerous hills

(Posillipo, Vomero, Camaldoli, Capodimonte, Pizzofalcone), with altitudes reaching values greater than 150 m. In the SE-S part of the Gulf of Naples, in the area of the Gulf of Castellammare and Sorrento peninsula, the Lattari Mountains are also present (Mount Faito is 1131 m high).

Finally, the morphology of the coastline around the gulf is very convoluted, and varies notably from N to S. In the northern part of the gulf sandy coasts smoothly degrade over the shelf, while in the Sorrento peninsula high calcareous cliffs rapidly decline at depths greater than 80 m (e.g., Cianelli et al., 2011).

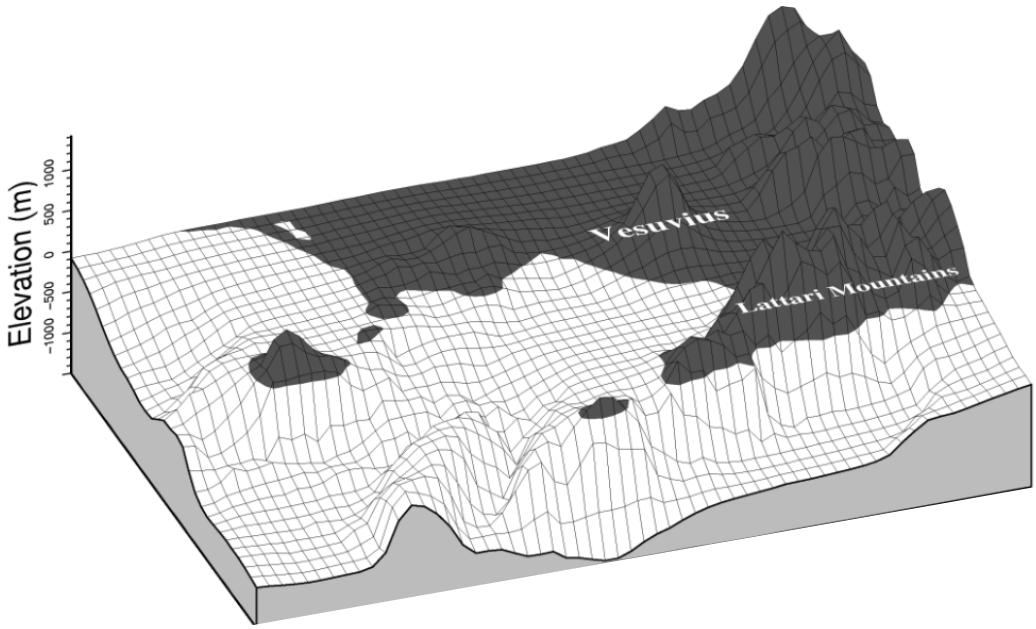

Figure 1.11: Orography of the area facing the Gulf of Naples (from Cianelli et al., 2011).

1.4 Observations of the hydrology and circulation in the Gulf of Naples

The first physical and hydrological data gathered in the Gulf of Naples date back to 1913 (Wendicke, 1916), when surveys were conducted during the summer months in 21 stations in the basin and adjacent waters. It then took almost fifty years before a complete set of records could be collected. During the 1957-1958 International Geophysical Year monthly data of numerous parameters (T, S, O2, pH and total phosphorous) were measured at 6 stations, including measurements of biochemical properties of the water (Hapgood, 1959). Soon after, current records began to be collected. De Maio (1959) measured subsurface currents using the parachute method. A few years later, Krauss and Düing (1963) obtained the first vertical current profiles collecting data at 28 stations, while Düing (1965) recorded currents in the Ischia channel and in the Bocca Piccola.

In the years 1966-67 the Institute of Meteorology and Oceanography of the Istituto Universitario Navale of Naples (now University ”Parthenope”) performed coastal current measurements with tracers around the Ischia, which provided data for about a year (De Maio et al. 1973). Several oceanographic campaigns have later been carried out to gather hydrological and current data in the gulf (e.g., Moretti et al., 1977; De Maio et al., 1985). This has undoubtedly contributed to achieve a fairly good understanding of the local regime of circulation. For many years these experimental results were the only ones on which our knowledge of the dynamics of the gulf could rely.

As far as the water masses are concerned, the main ones are present in the Gulf, deriving from the surface and intermediate branches of the

"Mediterranean conveyor belt" (Hopkins, 2001; Robinson et al., 2001): the MAW and the LIW. In the Gulf of Naples the MAW is located at depths around 50-100 m, with a salinity of 37.50 psu and temperatures that follow the seasonal variation, decreasing with the depth (in the winter the temperature assumes a virtually constant value of about 14^{o}C).

The second type of water mass, the LIW, is typically generated in the Rhodes gyre (in the eastern Mediterranean), where intense winds cause strong evaporation whose effect is a large increase of surface salinity (higher than 39.0 psu, e.g Lascaratos, 1993), and enters the western Mediterranean across the sills of the Strait of Sicily (e.g., Sparnocchia et al., 1999). In the gulf, the LIW flows in deepest layers in proximity of the Bocca Grande and is located below 200 m during summer and below 300 m during winter; the typical local hydrological values are T = 14.2^{o}C, S = 38.65 psu, σt = 29.0 kg/m^3 (De Maio et al., 1979). Other types of water masses can be found in different seasons. The winter mixing promotes the formation of the Tyrrhenian Intermediate Water (TIW), which is found in the homogeneous water column down to about 150 m and is characterized by temperature value around 14^{o}C and salinity value around 38.1 psu. Due to the summer warming and freshening, the TIW rises in the water column above 75 m, where it becomes Tyrrhenian Surface Water (TSW), its typical temperature and salinity values being 25.0^{o}C and 38.3 psu respectively (Hopkins, 1988). Another water mass similar to the TSW has been identified in the Gulf of Naples: the Coastal Surface Water (CSW). Its hydrological features are strongly affected by the Volturno and Sarno river discharges, as well as by the urban and industrial sewages, thus resulting in a water mass fresher and warmer than the TSW (Cianelli et al., 2011). In general, the local hydrology presents a seasonal variability characterized by a seasonal thermocline, with the summer

stratification of the water column determining the formation of a surface mixed layer 30-40 m thick; by contrast, the intense winter mixing involves the entire water column, which is homogeneous down to 150 m (e.g., Carrada et al., 1980).

We now pass to review the observations concerning the local dynamics of water masses. A first scheme of marine circulation within the gulf determined on the basis of current measurements and by tracers (Moretti et al., 1977) refers to stable NE winds (Fig. 1.12): a current flows away from the coast (from Torre del Greco) towards SW, forming a convergence zone. This flow pattern is attributed to the effect of the Vesuvius, that shelters the central part of the gulf from NE winds, that in turn find easy access to the sea along the Sarno river plain, so that the surface wind stress is remarkable on the sea surface in front of Castellammare and Torre Annunziata (divergence area). More northerly, the wind flows between the NW side of the Vesuvius and the Vomero hill, forming a coastal current that heads towards Cape Posillipo. In the modeling study of Gravili et al. (2001) the same circulation scheme has been reproduced with a barotropic model forced by idealized winds that simulated the shielding effect of the Vesuvius (see section 1.4 and Fig. 1.19).

During the years from 1977 to 1981 current measurements on 11 fixed points located along the coast in the two main openings and in the Ischia and Procida Channels were performed (De Maio et al., 1985). A spectral analysis of the obtained time series showed that currents with periods ≤ 24 h present a marked inertial component offshore and a breeze induced shift close to the coast, while motions evolving over periods > 24 h are responsible for long range transport (De Maio et al., 1985). Inertial phenomena are more evident in the warmer period of the year, when the higher tem-

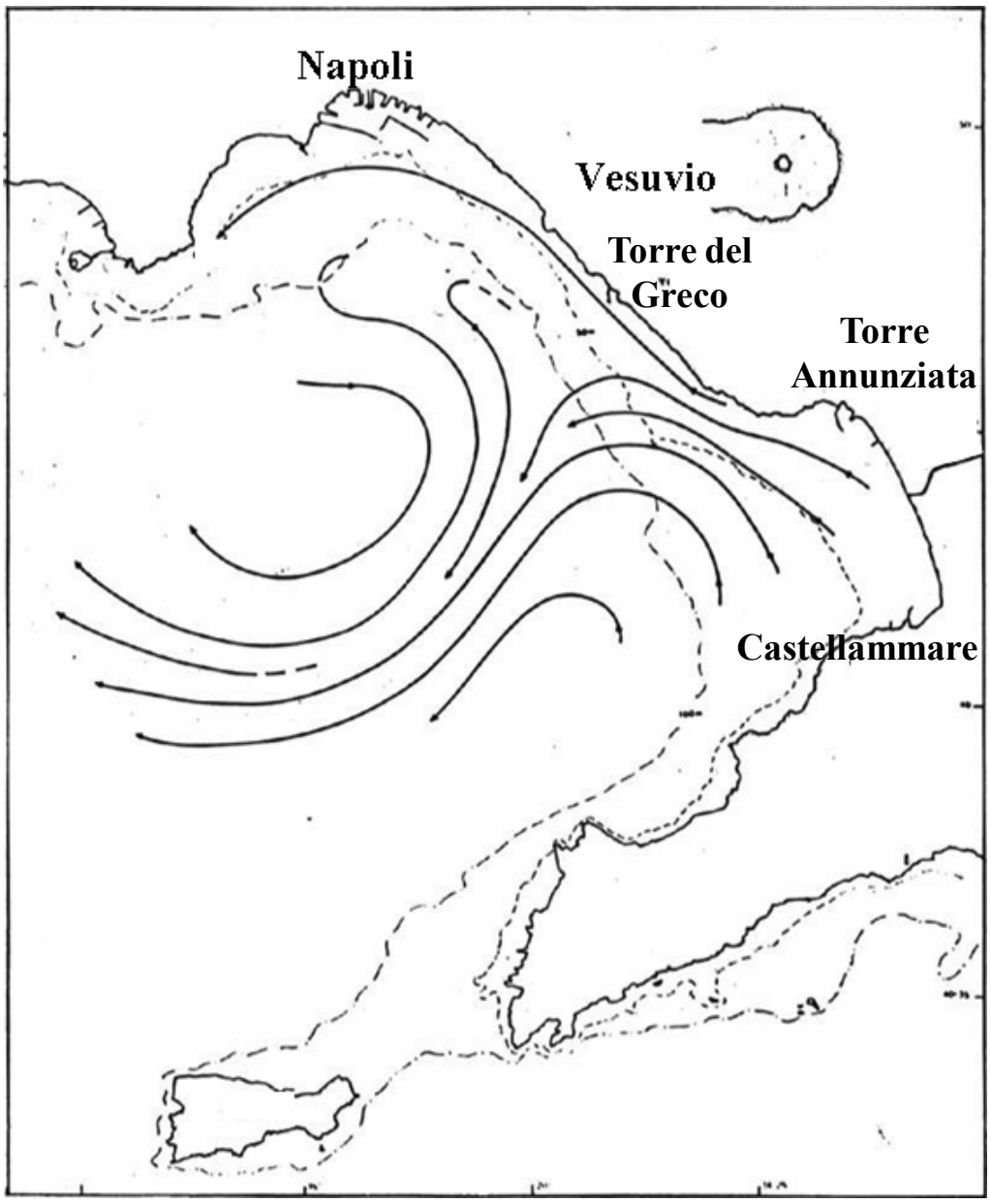

Figure 1.12: Surface marine circulation scheme produced by NE wind (from Moretti et al., 1977).

peratures produce a stable thermocline (Moretti et al., 1985). During winter, when storms are more frequent and energetic, inertial events are by contrast less recurrent (Moretti et al., 1985; Menna et al., 2008). Inertial oscillations are more evident in the outer part of the Gulf of Naples than close to the coast (Moretti et al., 1985). Roselli et al. (2007) observed that enhanced inertial oscillations might contribute to the resuspension of particles in the water column and enhance their sedimentation.

In the same work (De Maio et al., 1983) other typical surface circulation patterns are defined, which mainly depend on the wind direction (the wind is the main forcing surface circulation, producing currents of higher order than the average circulation of the basin). In particular, when the local winds are from NE (Fig. 1.13), the current enters the Gulf of Naples creating a basin-scale cyclonic gyre, whereas in the Gulf of Castellammare an anticyclonic vortex is formed (with this circulation structure, freshwaters coming from the Sarno river and from the city of Naples are transported offshore).

On the other hand, when the local winds are from S (Fig. 1.14), the inner basin remains isolated from the large-scale Tyrrhenian circulation, and a cyclonic gyre in the middle basin is observed, along with two smaller-scale anticyclonic vortices located in front of Naples and the Gulf of Castellammare. In this case the renovation of the coastal water is prevented and stagnation conditions are favoured; in the case of southerly winds the replacement of coastal waters is estimated to be much larger. As far as the role played by the large-scale Tyrrhenian Sea circulation is concerned, (De Maio et al., 1981) describe typical surface circulation patterns in the Gulf of Naples associated with strong northward (winter) or weaker southward (summer) Tyrrhenian currents just outside the gulf (Fig. 1.15). In conclusion, the circulation of water masses in the Gulf of Naples is affected by both the local wind and

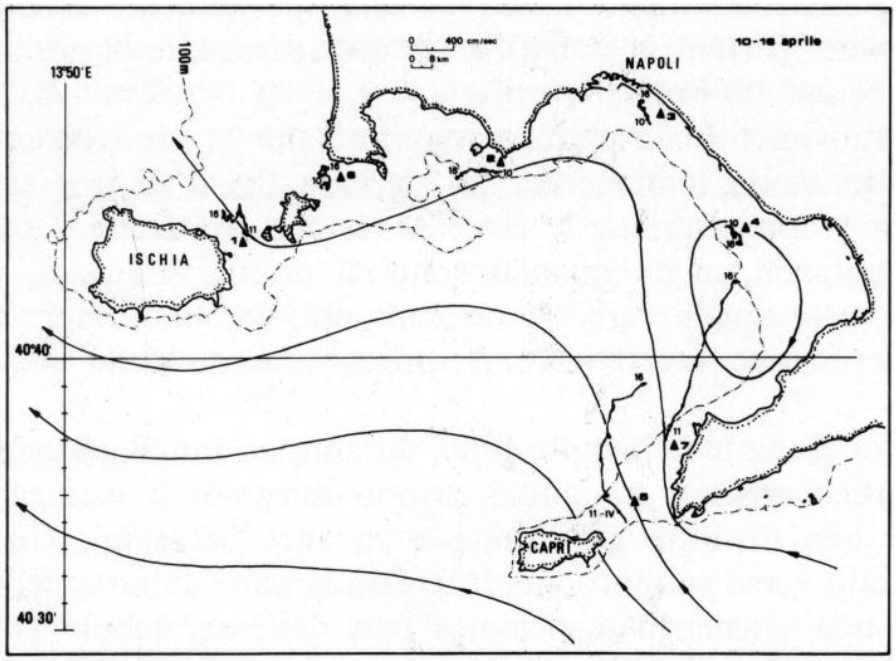

Figure 1.13: Northerly wind surface current circulation scheme (from De Maio et al., 1983).

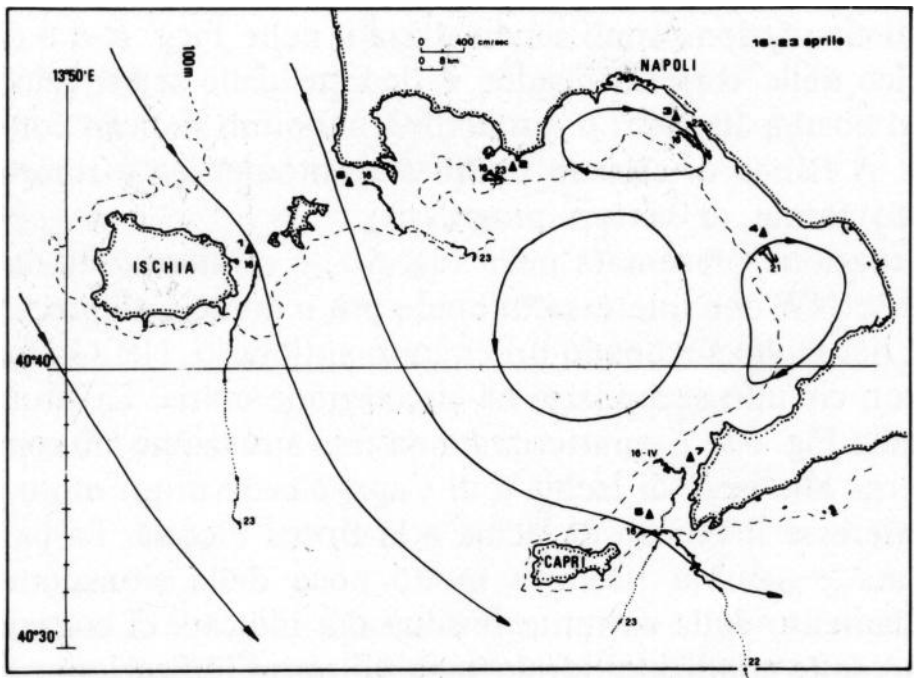

Figure 1.14: Southerly wind surface current circulation scheme (from De Maio et al., 1983).

the large-scale Tyrrhenian Sea circulation.

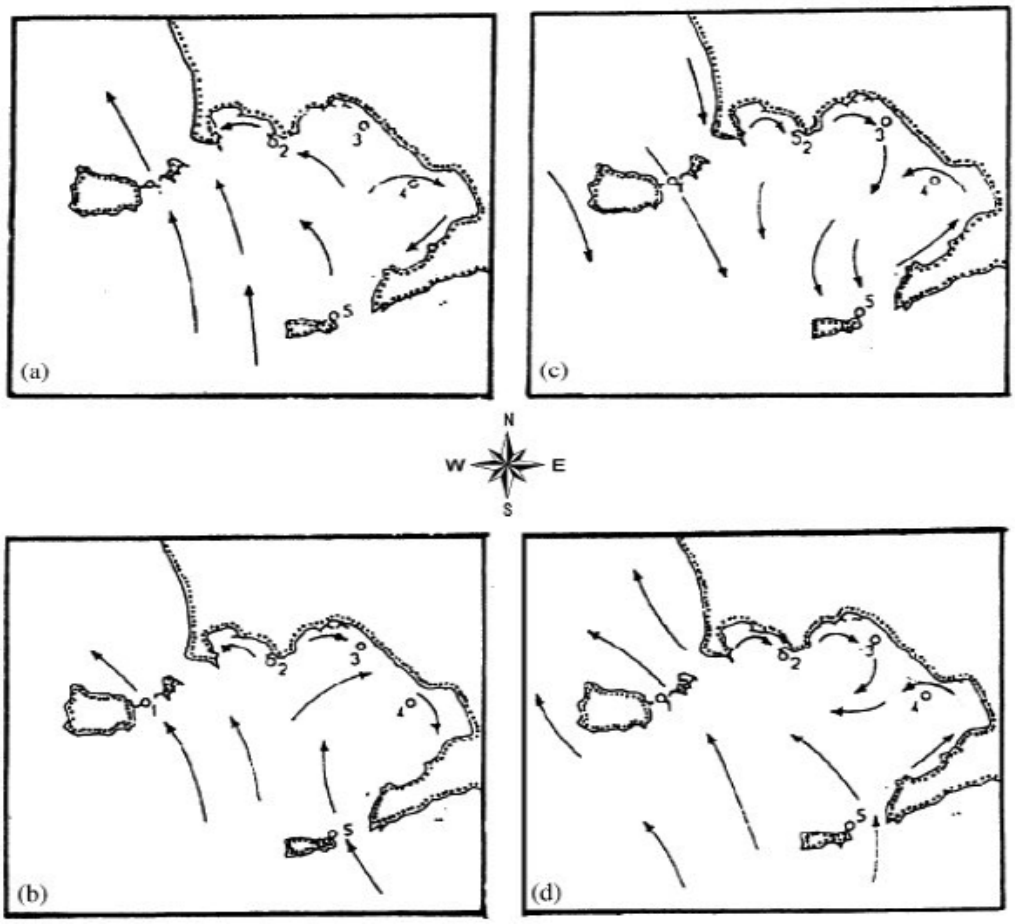

Figure 1.15: Schemes of some typical circulations in the Gulf of Naples (from De Maio et al., 1981).

More recently, the circulation schemes just described have been confirmed and analyzed more in detail thanks to an integrated monitoring system developed by the University of Naples Parthenope. An environmental monitoring system has been developed to acquire a thorough knowledge on the physical characteristics and dynamics in the gulf. This system consists of a series of instrumentations that perform measurements in the sea and in the atmosphere: 5 weather stations, a sea radar, that measures the sea surface current, and the Meteo Radar, that estimates rainfalls (Fig. 1.16).

Figure 1.16: Network monitoring of University Parthenope (http://ccmmma.uniparthenope.it).

The sea Radar system installed is a SeaSonde type manufactured by CODAR Ocean Sensors (Mountain View, California, USA); it works in the 25 MHz band, measuring surface currents relative to the first 1 m of the water column. The temporal resolution of the system is 1 h, while the range is approximately 35 Km from the coast. The original network installed in 2004 comprised two remote stations (in Portici and in Massa Lubrense); in this configuration the spatial resolution was 1250 m. In 2008 a third antenna was installed in Castellammare di Stabia (Cianelli et al., 2011); this implementation improved both the spatial coverage and resolution (1000 m).

Menna (2007) performed a detailed analysis of surface current observations in connection with local winds in the operating period 2002-2006. In section 6.1 an example of these surface current data will be presented. In winter, the dominant winds blow from NNE-NE, with speeds up to 8-10

m/s; occasional gusts from SW can reach higher velocities (> 10 m/s), due to the passage of depressionary systems over the basin, with rapid decreases of the air pressures and the setting up of intense winds. In spring, summer and fall an alternation between NE and SW winds is observed. During this period of the year, owing to the relaxation of larger scale forcings the breeze regime becomes dominant (Perusini et al., 1992), with a daily alternation of sea and land breeze wind. The most intense winds are always associated with SW wind (8-10 m/s or higher). The waters of the Gulf of Naples respond with a coincident clockwise rotation of the surface current field (Menna, 2007; Cianelli et al., 2011). Under the effect of the sea breeze, surface currents flow from W to E; on the contrary, in presence of land breeze, surface currents move from E to W. In between these two extremes, the current field turns clockwise by approximately 90^o in 6 hours so as to adapt to the changing wind conditions. The CODAR temporal resolution allows detecting such surface circulation variability (Fig. 1.17). In another recent work, Uttieri et al. (2011) have carried out a multiplatform analysis by combining HF radar current fields, satellite images and modelling tools. For the fall 2009 they concluded that the surface water renewal mechanisms were much more efficient than in the previous summer, thus explaining why the episodes of drastic decrease of the water quality, which took place in the area in August 2009, ceased after the end of the summer.

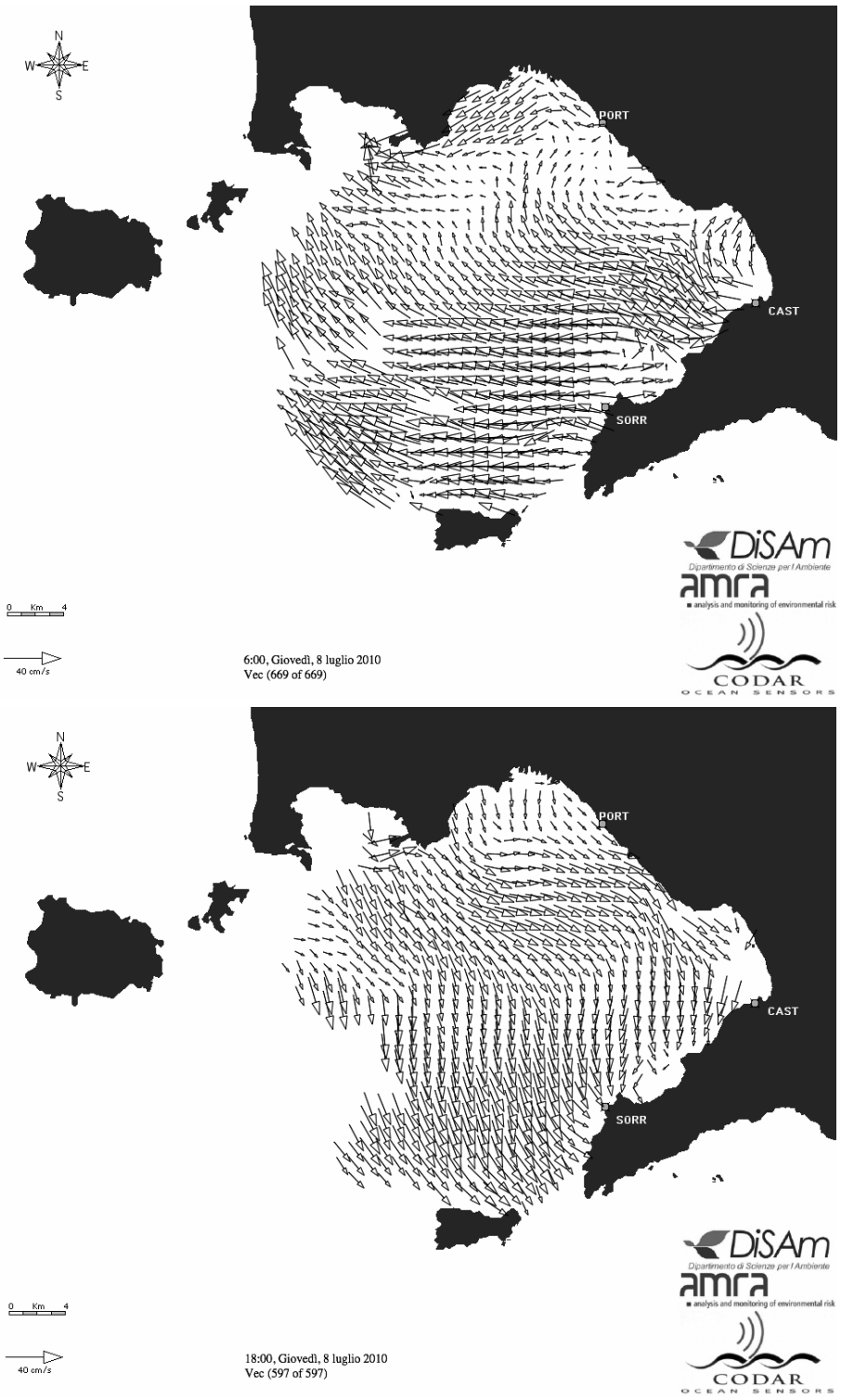

Figure 1.17: Surface circulation in the Gulf of Naples induced by the daily alternation of breeze winds, detected by HF radar measurements. The two panels show the evolution of the circulation field: at 06:00 GMT (upper panel)the flow is mainly directed offshore; at 18:00 GMT (lower panel) the flow is reversed (Cianelli et al., 2011).

1.5 Modeling the circulation in the Gulf of Naples

Along with the observational studies on the marine circulation in the Gulf of Naples discussed in the preceding section, modeling studies have also been developed for the same area (Gravili et al., 2001; Pierini et al., 2004, 2005; Grieco et al., 2005). Some results of those papers are now briefly reviewed.

Process-oriented model studies were have been carried out by Gravili et al. (2001) in order to analyze barotropic dynamical features in the Gulf of Naples, such as the gravitational normal mode oscillations (seiches) of the gulf and the depth-averaged circulation induced directly by the wind and remotely by the large-scale Tyrrhenian circulation. The shallow water equations are solved numerically in a domain which includes the Gulf of Naples and an external buffer zone whose role is two-fold: it is required to remove the effect of a fictitious boundary in the determination of the seiches, and it allows for the imposition of boundary conditions related to the large-scale circulation in the Tyrrhenian Sea, which contributes to determine the internal circulation via topographic coupling. The seiches are studied by means of a spectroscopic analysis in which eigenoscillations are generated by the relaxation of a wind setup. The eigenperiods corresponding to the main seiches are determined and the corresponding horizontal spatial structures are presented. Good agreement is found when comparing these numerical modeling results with tide gauge records.

The wind and boundary-driven depth-averaged circulation in the gulf has then been studied by imposing idealized local winds and external currents chosen on the basis of realistic modeling of the wind-driven circulation of the Tyrrhenian Sea. Both quasi-steady and typical transient-time

dependence are taken into account, so that a series of circulation schemes is obtained representing typical dynamic scenarios in the Gulf of Naples in good agreement with observations. Fig. 1.18 shows an example of scenarios produced by a spatially uniform surface wind stress and by external currents with a temporal variation shown in the upper panel. In Fig. 1.19 the shielding effect of the Vesuvius is shown (see section 1.3 and Fig. 1.12 for an experimental validation of this scenario).

Pierini et al. (2004) applied a three-layer shallow water model (developed for large-scale ocean circulation studies, e.g., Pierini, 2003) to the Gulf of Naples and adjacent areas (Fig. 1.20). The initialization was prescribed by hydrological structures based on observations, while the forcing was provided by both ECMWF surface wind stress fields with a resolution of $1/2^o$, and high-resolution (9 km) limited area model winds. Fig. 1.21 shows how the use of these two different wind products can significantly affect the oceanic response (see Signell et al., 2005, for a general discussion on the impact of wind quality in coastal ocean modeling). The study of Pierini et al. (2005) carried out with the same model will be discussed in section 6.

Grieco et al. (2005) developed a hybrid numerical approach to study the dispersion of passive/reactive tracers in the Gulf of Naples. To this end, Eulerian and Lagrangian schemes were implemented in the barotropic form of the Princeton Ocean Model, which were then and applied to the dispersion of zoo- and phytoplankton in the gulf. The hybrid technique was first validated by comparing the tracer concentration patterns from the Eulerian model and maps of particle positions from the Lagrangian model. Excellent agreement in both spatial distribution and temporal evolution of these quantities was found between the two models. Second, the circulation in the gulf was simulated using the Princeton Ocean Model model imple-

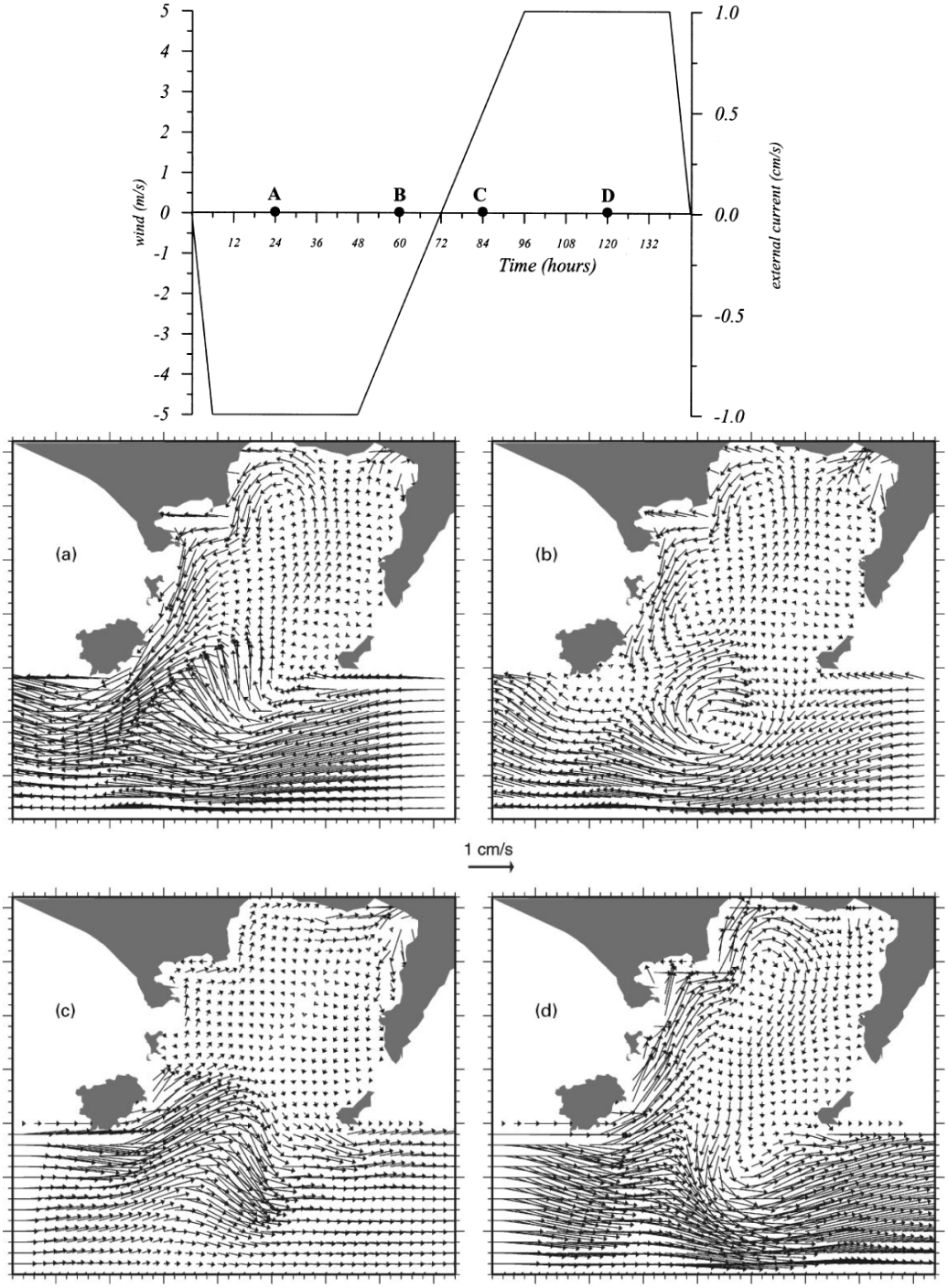

Figure 1.18: Upper panel: time dependence of the imposed external currents and wind forcing. Lower panels: depth-averaged currents corresponding to times indicated by A, B, C, D in the upper panel (adapted from Gravili et al., 2001).

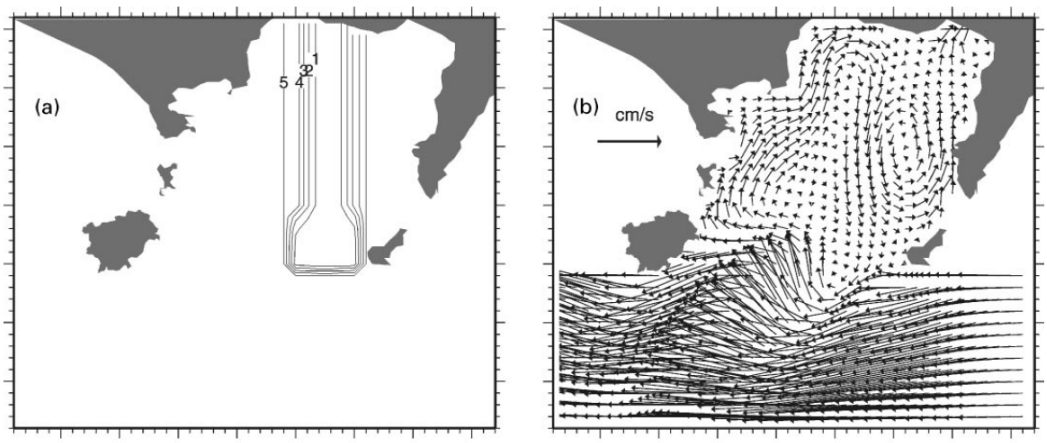

Figure 1.19: (a): Isolines of the amplitude of the wind forcing directed along the negative y-direction (nearly north-easterly); (b): depth-averaged currents generated by forcing (a) and corresponding to time A of the upper panel of Fig. 1.18 (compare with map (a) of Fig. 1.18 referring to the same forcing except for a spatially uniform wind; adapted from Gravili et al., 2001).

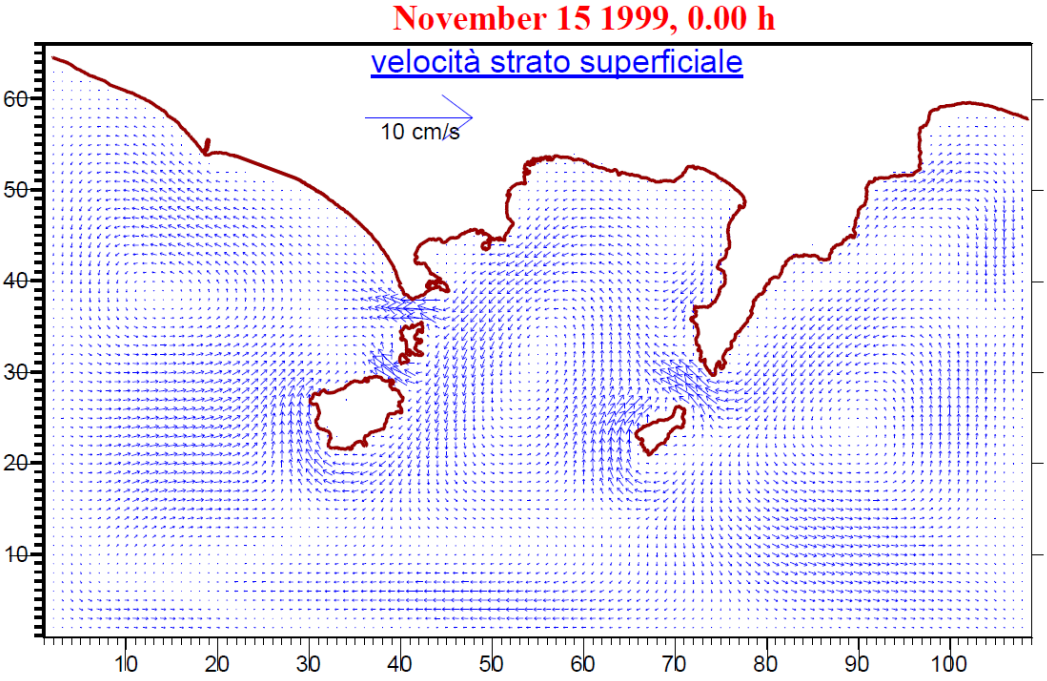

Figure 1.20: (Example of instantaneous velocity field in the upper layer of the three-layer SW model implemented in the Gulf of Naples (adapted from Pierini et al., 2004).

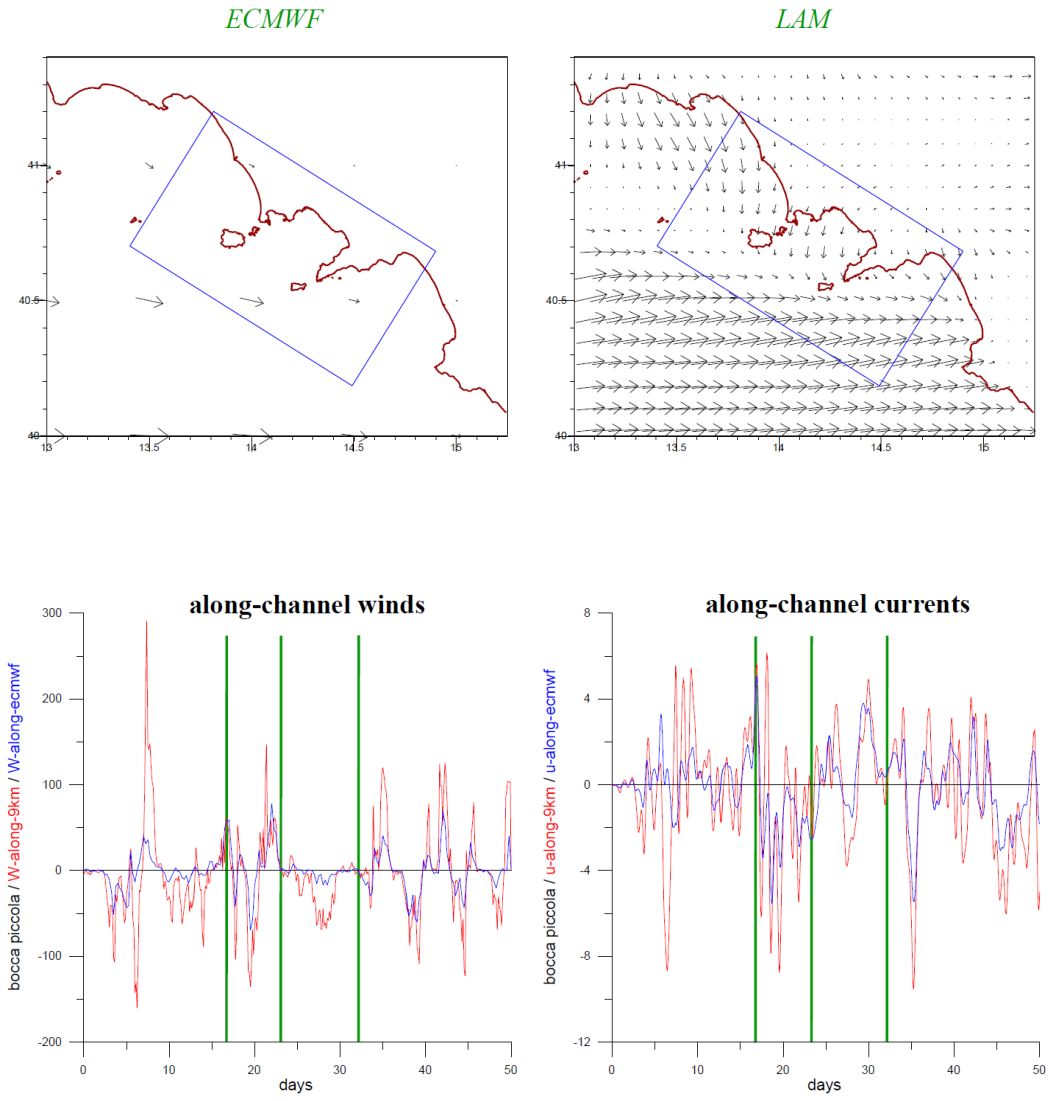

Figure 1.21: (Upper panels: example of instantaneous ECMWF and LAM winds (November 20, 2003, 0.0 h). Lower panels: winds and modeled currents in the surface layer in the Bocca Piccola projected onto the along-channel direction (adapted from Pierini et al., 2004).

mented with the same configuration adopted by Gravili et al. (2001) (Fig. 1.22). While using simplified forcing fields, the simulated circulation pat-

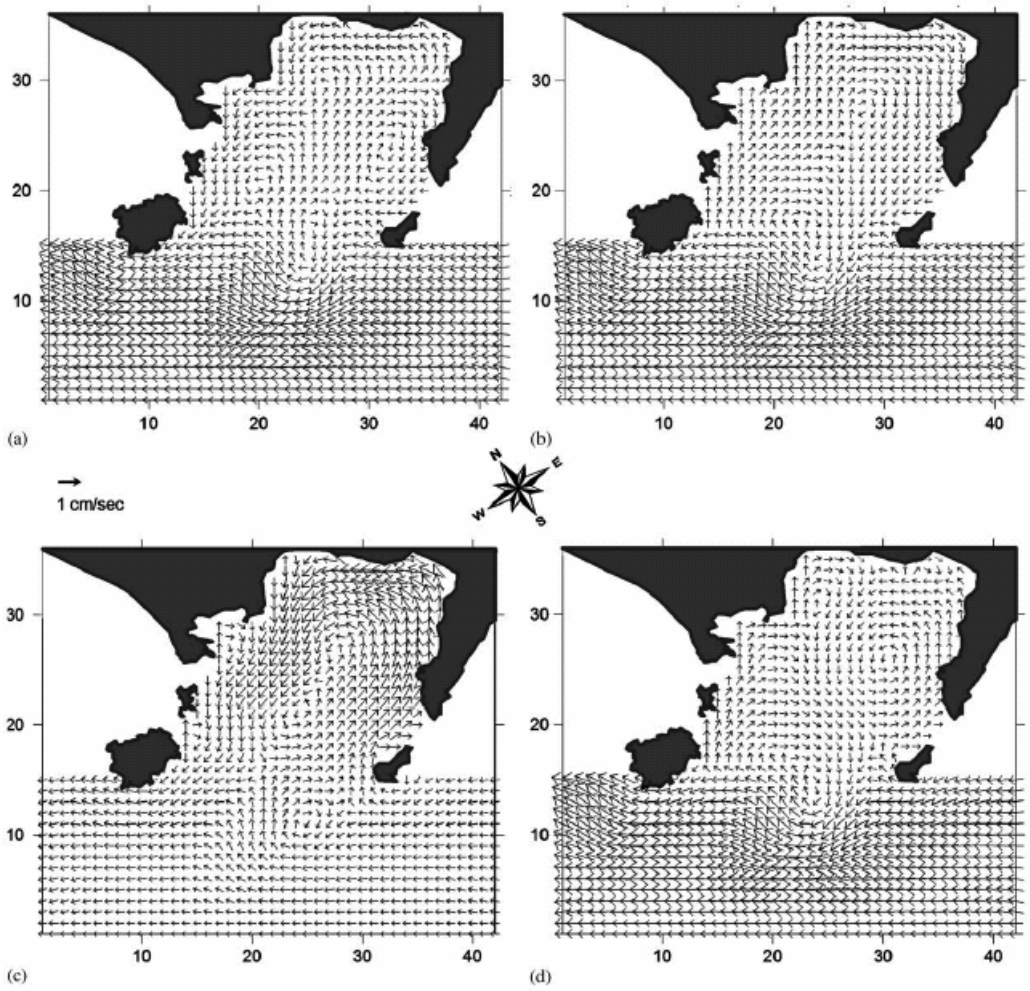

Figure 1.22: The seasonal mean circulation patterns in the Gulf of Naples: January (a), April (b), July (c) and October (d), from Princeton Ocean Model in 1998 using monthly varying surface wind stress and a constant northwestward Tyrrhenian current of 1 cm/s entering the domain from the right (South-East; from Grieco et al., 2005).

terns reproduced many observed features. These include the flushing of the gulf waters typically occurring in spring and the formation of a close cyclonic gyre (trapping and homogenizing tracers in the gulf) in autumn. The circulation patterns were found to be strongly influenced by both the surface wind stresses and bathymetry and only "remotely" by the Tyrrhenian

circulation.

These modeling efforts focused on the Gulf of Naples and adjacent areas have in common a process-oriented approach with different degree of realism; all the implementations have indeed been proved valuable for investigating specific and fundamental aspects of the local circulation. If, on the other hand, a more realistic approach is to be achieved, then, apart from other technical aspects, a fundamental component of the modeling system must be introduced that is lacking in the studies mentioned above, namely the coupling with a coarser and larger scale Tyrrhenian Sea model. In the remainder of the thesis the implementation of the Princeton Ocean Model nested with such a larger scale model will be presented.

Chapter 2

The Princeton Ocean Model

2.1 The mathematical model

In this chapter we will provide a detailed description of the Princeton Ocean Model (POM), that is the modeling tool used for our simulations. The POM was developed by Blumberg and Mellor in the late 70's and subsequently improved by the scientific community; papers that either describe the numerical model (Blumberg and Mellor, 1987) or made use of the model are contained in the Reference Section, and a more complete list is available on the POM home page at (Mellor, 2004): `http://www.aos.princeton.edu/WWWPUBLIC/htdocs.pom`; the latest version (officially dated 2006) is the one used here.

POM is a sigma-coordinate, free surface, primitive equation model that contains a sub-model (Mellor and Yamada, 1982) for the turbulent vertical mixing often cited in the literature as the Mellor-Yamada turbulence closure model (it should be noted that the model is based on turbulence hypotheses by Rotta and Kolmogorov which was then extended to stratified flow cases). Here, the Level 2.5 model is used together with a prognostic equation for the

turbulence macroscale.

The vertical sigma coordinate system (Fig. 2.1) is a valuable attribute when dealing with significant topographical variations such as those encountered in estuaries or over continental shelf breaks and slopes; in this coordinate system, the number of vertical levels in the water column is the same everywhere in the domain irrespective of the depth of the water column. Thus, the choice of such a sigma coordinate ocean model appears ideal in our case, in which a very variable and complex topography is present (e.g., see Fig. 1.10).

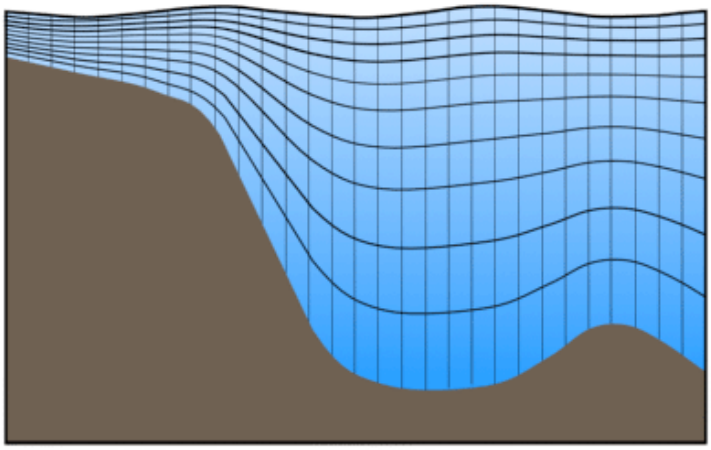

Figure 2.1: Example of sigma coordinate system that follows the bathymetry.

With the sigma coordinate system, and together with the turbulence submodel, the model produces realistic bottom boundary layers, which are important in coastal waters. The horizontal grid uses curvilinear orthogonal coordinates and an "Arakawa C" differencing scheme. The free surface (η) formulation, that is essential to simulate a coastal basin circulation, is possible thanks to adopted time-splitting technique (Simons, 1974; Madala and Piacsek, 1977); this involves separating out the external and internal mode equations and solving each of them separately at the appropriate time steps

dictated by the respective gravity wave speeds, making sure that the two calculations are consistent and synchronous with each other (see section 2.2). The principal advantage of this method is significant savings in computing time, because the vertically integrated, barotropic equations governing external mode are fewer and much simpler to solve. The baroclinic (or vertical structure) equations, on the other hand, are more expensive to solve and are solved at much larger time steps dictated by the slow speed of internal gravity waves, under this scheme. The barotropic equations still need to be solved al smaller time steps determined by the fast external gravity waves, but these calculations are only a small fraction of the total. As for the three-dimensional mode, its vertical differencing is implicit (without time constraints), permitting the use of fine vertical resolution in the surface and bottom boundary layers, and the complete thermodynamics are implemented.

2.2 The governing equations

The model uses orthogonal curvilinear coordinates in the horizontal and the sigma coordinate system in the vertical. Let x, y and z be the conventional Cartesian coordinates; the basic equations are derived in the sigma coordinate system by this transformation:

$$\sigma = \frac{x - \eta}{H + \eta} \tag{2.1}$$

where $D = H + \eta$, $H(x, y)$ is the bottom topography and $\eta(x, y, t)$ is the surface elevation; thus, σ ranges from $\sigma = 0$ at $z = \eta$ to $\sigma = -1$ at $z = H$ (Fig. 2.2).

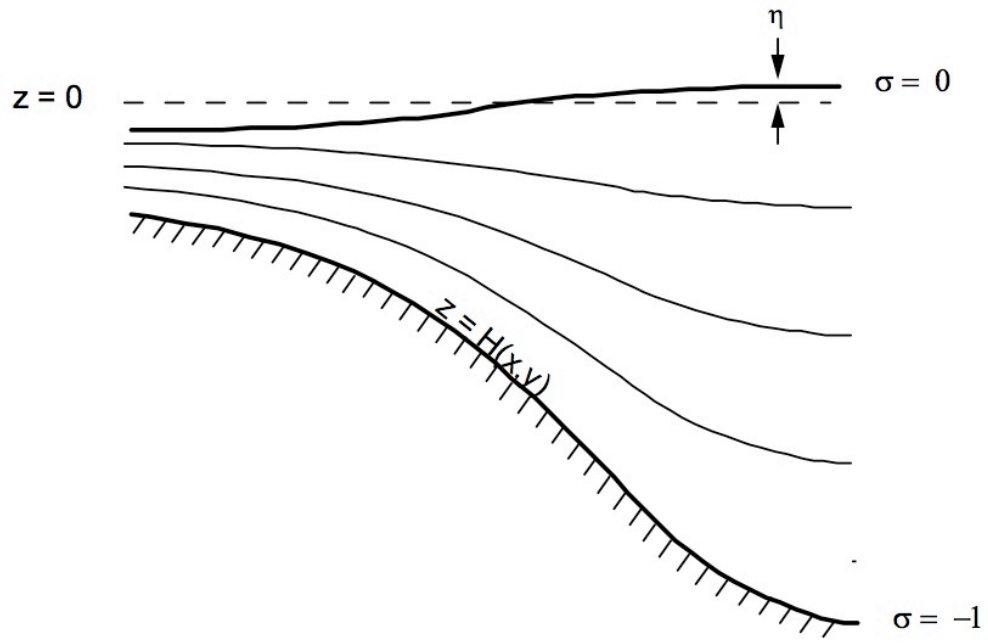

Figure 2.2: The sigma coordinate system (from Mellor, 2004).

After conversion to sigma coordinates the basic equations may be written in horizontal Cartesian coordinates:

$$\frac{\partial \eta}{\partial t} + \frac{\partial UD}{\partial x} + \frac{\partial VD}{\partial y} + \frac{\partial \omega}{\partial \sigma} = 0 \tag{2.2}$$

$$\begin{aligned} &\frac{\partial UD}{\partial t} + \frac{\partial U^2 D}{\partial x} + \frac{\partial UVD}{\partial y} + \frac{\partial U\omega}{\partial \sigma} - fVD + gD\frac{\partial \eta}{\partial x} + \\ &\frac{gD^2}{\rho_0}\int_\sigma^0 \left[\frac{\partial \rho'}{\partial x} - \frac{\sigma'}{D}\frac{\partial D}{\partial x}\frac{\partial \rho'}{\partial \sigma'}\right] d\sigma' = \frac{\partial}{\partial \sigma}\left[\frac{K_M}{D}\frac{\partial U}{\partial \sigma}\right] + F_x \end{aligned} \tag{2.3}$$

$$\begin{aligned} &\frac{\partial VD}{\partial t} + \frac{\partial V^2 D}{\partial y} + \frac{\partial UVD}{\partial x} + \frac{\partial V\omega}{\partial \sigma} + fUD + gD\frac{\partial \eta}{\partial y} + \\ &\frac{gD^2}{\rho_0}\int_\sigma^0 \left[\frac{\partial \rho'}{\partial y} - \frac{\sigma'}{D}\frac{\partial D}{\partial y}\frac{\partial \rho'}{\partial \sigma'}\right] d\sigma' = \frac{\partial}{\partial \sigma}\left[\frac{K_M}{D}\frac{\partial V}{\partial \sigma}\right] + F_y \end{aligned} \tag{2.4}$$

$$\frac{\partial TD}{\partial t} + \frac{\partial TUD}{\partial x} + \frac{\partial TVD}{\partial y} + \frac{\partial T\omega}{\partial \sigma} = \frac{\partial}{\partial \sigma}\left[\frac{K_H}{D}\frac{\partial T}{\partial \sigma}\right] + F_T - \frac{\partial R}{\partial z} \tag{2.5}$$

$$\frac{\partial SD}{\partial t} + \frac{\partial SUD}{\partial x} + \frac{\partial SVD}{\partial y} + \frac{\partial S\omega}{\partial \sigma} = \frac{\partial}{\partial \sigma}\left[\frac{K_H}{D}\frac{\partial S}{\partial \sigma}\right] + F_S \tag{2.6}$$

$$\begin{aligned}\frac{\partial q^2 D}{\partial t}+\frac{\partial U q^2 D}{\partial x}+\frac{\partial V q^2 D}{\partial y}+\frac{\partial \omega q^2}{\partial \sigma}&=\frac{\partial}{\partial \sigma}\left[\frac{K_q}{D}\frac{\partial q^2}{\partial \sigma}\right]\\&+\frac{K_M}{D}\left[\left(\frac{\partial U}{\partial \sigma}\right)^2+\left(\frac{\partial V}{\partial \sigma}\right)^2\right]+\frac{2g}{\rho_0}K_H\frac{\partial \rho}{\partial \sigma}-\frac{2Dq^3}{B_1 l}+F_q\end{aligned} \tag{2.7}$$

$$\begin{aligned}\frac{\partial q^2 lD}{\partial t}+\frac{\partial U q^2 lD}{\partial x}+\frac{\partial V q^2 lD}{\partial y}+\frac{\partial \omega q^2 l}{\partial \sigma}&=\frac{\partial}{\partial \sigma}\left[\frac{K_q}{D}\frac{\partial q^2 l}{\partial \sigma}\right]\\&+E_1 l\left(\frac{K_M}{D}\left[\left(\frac{\partial U}{\partial \sigma}\right)^2+\left(\frac{\partial V}{\partial \sigma}\right)^2\right]+E_3\frac{g}{\rho_0}K_H\frac{\partial \rho}{\partial \sigma}\right)-\frac{Dq^3}{B_1}W+F_{ql}\end{aligned} \tag{2.8}$$

Equation (2.2) is the mass conservation equation, and equations (2.3) and (2.4) are the momentum equations in the horizontal direction; note that ω is the transformed vertical velocity (it is the velocity component normal to the sigma surfaces); the transformation to the Cartesian vertical velocity is

$$W=\omega+U\left(\sigma\frac{\partial D}{\partial x}+\frac{\partial \eta}{\partial x}\right)+V\left(\sigma\frac{\partial D}{\partial y}+\frac{\partial \eta}{\partial y}\right)+\sigma\frac{\partial D}{\partial t}+\frac{\partial \eta}{\partial t} \tag{2.9}$$

In the momentum equations (2.3) and (2.4), the fluid acceleration is balanced by the Coriolis force, the pressure gradient force and the horizontal viscosity and diffusion terms. The governing equations are simplified by assuming that the fluid is incompressible and of weakly variable density. Thus variations in density are ignored except when the density is multiplied by the gravitational acceleration, thus retaining the important stratification (i.e. buoyancy) effects; this is the so-called Boussinesq approximation. All terms, except the gravitational and pressure gradient, are ignored in the momentum equation in the vertical, equivalent to a hydrostatic balance, even though the fluid is in motion. The equations (2.5) and (2.6), temperature (T) and salinity (S) equations, respectively, together resolve the thermodynamic processes; while the equation (2.7) and (2.8) estimate (in deterministic way) the kinetic energy (q).

As far as the turbulent mixing parameterization is concerned, while the

values of horizontal diffusivities are also influenced by numerical considerations arising from the need to damp subgrid scale computational noise, the vertical diffusivities are principally determined from small scale turbulent mixing in the water column; nevertheless, proper parameterization is the most important unresolved issue in ocean modelling since the model results are sensitive in varying degrees to the values of these coefficients and the theoretical underpinnings needed to confidently prescribe them are for the most part quite shaky.

It is not unusual to use 0^{th} order closure models for these diffusivities and regard them as constants throughout. This is rather counter-intuitive, since these values are functions of the prevailing turbulence field in the fluid and strictly speaking should be derived from properties of turbulent mixing occurring in the fluid. However, away from the fully turbulent mixed layers near the surface and the bottom of the ocean, very little is known about intermittent mixing processes that occur in the interior of the ocean.

Traditionally, the diffusivities terms are prescribed a priori as constant values and these values are "tuned" to obtain the desired results. However, because of the sensitivity of the model output to these values, this ad-hoc procedure has become increasingly untenable and better prescriptions often using higher order closures have become the norm. For example, this model uses 0^{th} order closure for the horizontal mixing, thus relating them to mean deformation rates in the fluid, while the vertical mixing is obtained from 2^{nd} order closure (also called second moment closure) for small-scale turbulent mixing that principally determines the vertical diffusivities in the upper and bottom mixed layers.

With regard to the horizontal mixing, the diffusivities terms F_x and F_y,

in equations (2.3) and (2.4), are defined according to

$$F_x = \frac{\partial}{\partial x}\left[H2A_M\frac{\partial U}{\partial x}\right] + \frac{\partial}{\partial y}\left[HA_M\left(\frac{\partial U}{\partial y} + \frac{\partial V}{\partial x}\right)\right] \tag{2.10}$$

$$F_y = \frac{\partial}{\partial y}\left[H2A_M\frac{\partial V}{\partial y}\right] + \frac{\partial}{\partial y}\left[HA_M\left(\frac{\partial U}{\partial y} + \frac{\partial V}{\partial x}\right)\right] \tag{2.11}$$

where A_M is the horizontal eddy diffusivities, that can be considered as constant value or flow-dependent; in the flow-dependent case, generally, the model use the Smagorinsky formula to estimate A_M:

$$A_M = C\Delta x\Delta y\frac{1}{2}\left|\nabla V + (\nabla V)^T\right| \tag{2.12}$$

where $\left|\nabla V + (\nabla V)^T\right|$ is the characteristic flow term and C is the Horcon parameter; the Horcon values in the range, 0.10 to 0.20 seem to work well, but, if the grid spacing is small enough (Oey et al., 985a,b), C can be nil. An advantage of the Smagorinsky relation is that C is non-dimensional; related advantages are that A_M decreases as resolution improves and that A_M is small if velocity gradients are small.

The vertical eddy diffusivities K_H and K_M (see equations (2.3-2.8)) are instead defined as

$$K_M = qlS_M \tag{2.13}$$

$$K_H = qlS_H \tag{2.14}$$

where q is the eddy-kinetic energy calculated in subroutine PROFQ (see section 2.2), l is the turbulence length scale, and the coefficients, S_M and S_H, are given by

$$S_H[1 - (3A_2B_2 + 18A_1A_2)G_H] = A_2[1 - 6A_1/B_1] \tag{2.15}$$

$$S_M[1 - 9A_1A_2G_H] - S_H[(18A_1B_2 + 8A_1A_2)G_H] = A_1[1 - 3C_1 - 6A_1/B_1] \tag{2.16}$$

where

$$G_H = \frac{l^2}{q^2}\frac{g}{\rho_0}\left[\frac{\partial \rho}{\partial z} - \frac{1}{c_s^2}\frac{\partial p}{\partial z}\right] \tag{2.17}$$

is a Richardson number. The five constants in (2.15) and (2.16) are evaluated from neutral homogeneous and near surface turbulence data (law-of-the-wall region) and are found (Mellor and Yamada, 1982) to be $(A_1B_1A_2B_2C_1) = (0.92, 16.6, 0.74, 10.1, 0.08)$.

This set of equations (see equations 2.3-2.8) needs to be supplemented by initial and boundary conditions on the prognostic variables. These depend on the nature of the solution sought. The free surface is a material surface and hence there cannot be any flow across it; this is given by the condition $\omega = 0$ at $\sigma = 0$. The ocean bottom is also impermeable and the condition $\omega = 0$ at $\sigma = -1$ satisfies this requirement. In addition, the oceans are driven by momentum, heat and salt fluxes at the air-sea interface and at the bottom these values are normally zero due to bottom stress, which in turn depends on the surface roughness and flow velocity near the bottom. The boundary conditions at the free surface and the bottom have to be prescribed.

In this model, the momentum, heat and salt fluxes at the free surface are given by

$$\frac{K_M}{D}\left(\frac{\partial U}{\partial \sigma}, \frac{\partial V}{\partial \sigma}\right) = -(\langle wu(0)\rangle, \langle wv(0)\rangle), \sigma \longrightarrow 0 \tag{2.18}$$

$$\frac{K_H}{D}\left(\frac{\partial T}{\partial \sigma}, \frac{\partial S}{\partial \sigma}\right) = -(\langle w\theta(0)\rangle), \sigma \longrightarrow 0 \tag{2.19}$$

$$(q^2(0), q^2l(0)) = (B_1^{2/3}u_\tau^2(0), 0) \tag{2.20}$$

where the r.h.s. in (2.18) is the input value of the surface wind stress; the r.h.s. in the (2.19) is the net heat flux, dependent on the turbulent sensible and latent heat fluxes, and salt fluxes, dependent on the difference between the evaporation rate and the precipitation rate at the air-sea interface. The equations, (2.18) and the (2.19), are, respectively, the surface boundary conditions for the (2.3) and (2.4), and for the equations (2.5) and (2.6). The equation (2.20) is the surface boundary conditions for the equations (2.7) and (2.8), where the turbulence closure constant has an important role.

Conversely the bottom boundary conditions are

$$\frac{K_M}{D}\left(\frac{\partial U}{\partial \sigma}, \frac{\partial V}{\partial \sigma}\right) = C_z\left[U^2 + V^2\right]^{1/2}(U, V), \sigma \longrightarrow -1 \tag{2.21}$$

$$\frac{K_H}{D}\left(\frac{\partial T}{\partial \sigma}, \frac{\partial S}{\partial \sigma}\right) = 0, \sigma \longrightarrow -1 \tag{2.22}$$

$$(q^2(-1), q^2 l(-1)) = (B_1^{2/3} u_t^2(-1), 0) \tag{2.23}$$

The equation (2.21) is the bottom condition for equations (2.3) and (2.4), where the drag coefficient (C_z) is determined either by matching to the logarithmic law of the wall if resolution is adequate or prescribed at the canonical value of 0.0025:

$$C_z = MAX\left[\frac{K^2}{\left[\ln\left\{1 + \sigma_{Kb-1} H/z_0\right\}\right]^2}, 0.0025\right] \tag{2.24}$$

where k = 0.4 is the von Karman constant and z_0 is the roughness parameter. The equations (2.22) and (2.23) are the bottom boundary conditions, respectively, for the equations (2.5) and (2.6) and for the equations (2.7) and (2.8).

2.3 The numerical scheme

The governing equations discussed in the previous section are a coupled set of nonlinear partial differential equations (PDEs) governing the time-dependent behaviour of properties of a fluid flowing in three-dimensional space and acted upon by various forces. Because of the vertical mixing and Laplacian horizontal diffusion terms, the governing equations are second-order PDEs. Numerical solutions require the domain to be discretized and the governing equations reduced to their finite difference equivalents.

The solution technique can be explicit or implicit, while regard to order of differences scheme, the most common practice is to use the lowest order possible and rely on a smaller grid size for better accuracies.

The treatment of the vertical mixing terms requires flexibility in the choice of the vertical grid, with the use of appropriate thinning in the regions of the boundary layers and, more generally, in regions characterized by strong vertical shear. For this reason, it is more convenient to use implicit schemes in the vertical, so to avoid severe limitations on the time step due to the inhomogeneous grid spacing.

POM adopts for the spatial discretization a second-order finite difference scheme implicit in the vertical and explicit in the horizontal, relying on the Thomas algorithm (Fletcher, 1987) for efficient solution of the resulting tridiagonal matrix equations.

The explicit scheme in the horizontal direction for both internal and external modes introduces time step constraints from the Courant-Friedrichs-Lewy (CFL) condition:

$$\Delta t \leq \frac{1}{2c} \left| \frac{1}{\partial x^2} + \frac{1}{\partial y^2} \right|^{-1/2} \tag{2.25}$$

where c is the external gravity wave speed $(c = (gh)^{1/2})$ for the external mode, or the internal gravity wave speed $(c = (g'\bar{h})^{1/2})$for the internal mode. The internal mode has additional limits imposed by horizontal diffusion (momentum o scalars) and rotation (Mellor, 2004).

Figure 2.3 shows the time stepping process (the temporal scheme is a leapfrog). The former uses a short time step, d_{te}, whereas the latter uses a long time step, d_{ti}. The external mode primarily provides the surface elevation to the internal mode whereas, as symbolized by "Feedback", the internal mode provides integrals of momentum advection, density integrals and bottom stress to external mode at the time $t^{(n)}$.

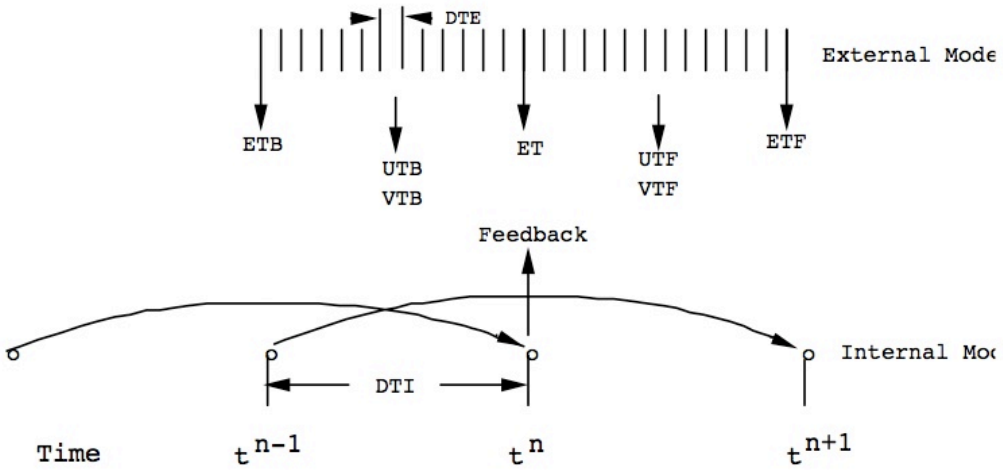

Figure 2.3: A simplified illustration of the interaction of the external mode and the internal mode (from Mellor, 2004).

With regard to the spatial discretization, the model uses the staggered Arakawa C grid for discretization in the horizontal direction (Fig. 2.4); in this grid, quantities such us H and η are defined at the center of the grid, while the east-west velocity component is displaced half a grid point to the west of the grid center and the north-south component is displaced half a grid to the south of the grid center. C grid has favourable wave propagation

properties if the grid size is smaller than the Rossby deformation radius. Since implementation to coastal oceans implies invariably fine resolution grids, the C grid appears to be a much better choice for discretization. Besides, for application to shallow coastal waters around ocean basins, high spatial resolution is rather imperative so that the shorter spatial scales typical of the processes in such regions can be resolved. Once again a staggered C grid is better suited to this application.

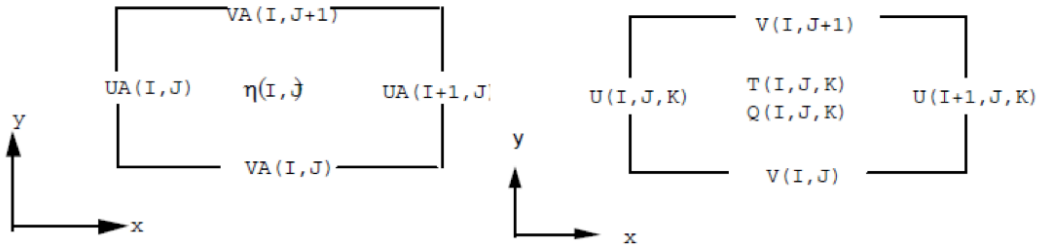

Figure 2.4: The horizontal discretization for two-dimensional external mode (left) and for three-dimensional internal mode (right; from Mellor, 2004).

The three-dimensional variables are staggered not only in the horizontal but also in the vertical direction. While q, l, ω, K_M and K_H are located at σ levels, variables u, v, T, S and ρ are staggered in the vertical and therefore located between two corresponding σ levels (Fig. 2.5).

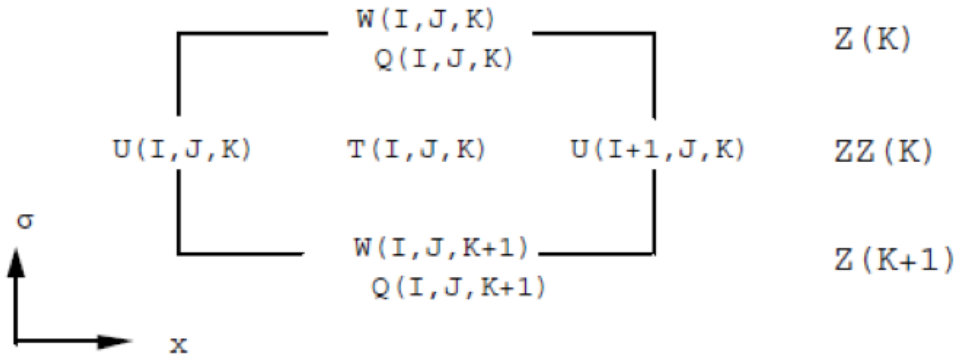

Figure 2.5: The vertical discretization for three-dimensional internal mode, where Q represents K_M , K_H, q^2, or q^{2l}. T represents t, s or ρ (from Mellor, 2004).

The code structure is shown in Fig. 2.6 The calculation consists of two nested loops, loop 8000 nested in loop 9000, the former corresponding to the external mode computations and the other to the internal mode. The routine BAROPG calculates the pressure gradients arising from horizontal density gradients; note the fact that, in the code, the average density has been subtracted from the density before the integrals are calculated. An average density is the basin area average values of density, which is mapped onto the sigma-grid just as the initial conditions were similarly mapped. This procedure reduces the errors in sigma-coordinate model computations of pressure gradients and prevents along-slope currents from destroying the solutions and removes most of the truncation error in the transformed baroclinic terms.

The internal mode solution is obtained in the subroutines PROFT, PROFS, PROFU, PROFV and PROFQ, which solve temperature, salinity, velocity and kinetic energy, respectively. The advection and horizontal diffusion terms needed by these routines are supplied by routines ADVT, ADVU, ADVV and ADVQ.

External mode calculations yield the sea surface elevation and the vertically averaged barotropic velocity components. They therefore provide the elevation gradients needed for the internal mode calculations. The bottom friction and the vertical integrals of the density gradients (integrated baroclinic forcing) needed to make the external mode calculations come from the internal mode calculations, which yield internal variables. This is how the two calculations interact with each other. However, the interaction is tricky because of the time step disparities and care has been taken in constructing the computing engine (Mellor, 2004) to conserve properties and prevent the two calculations from drifting apart in long-term integrations

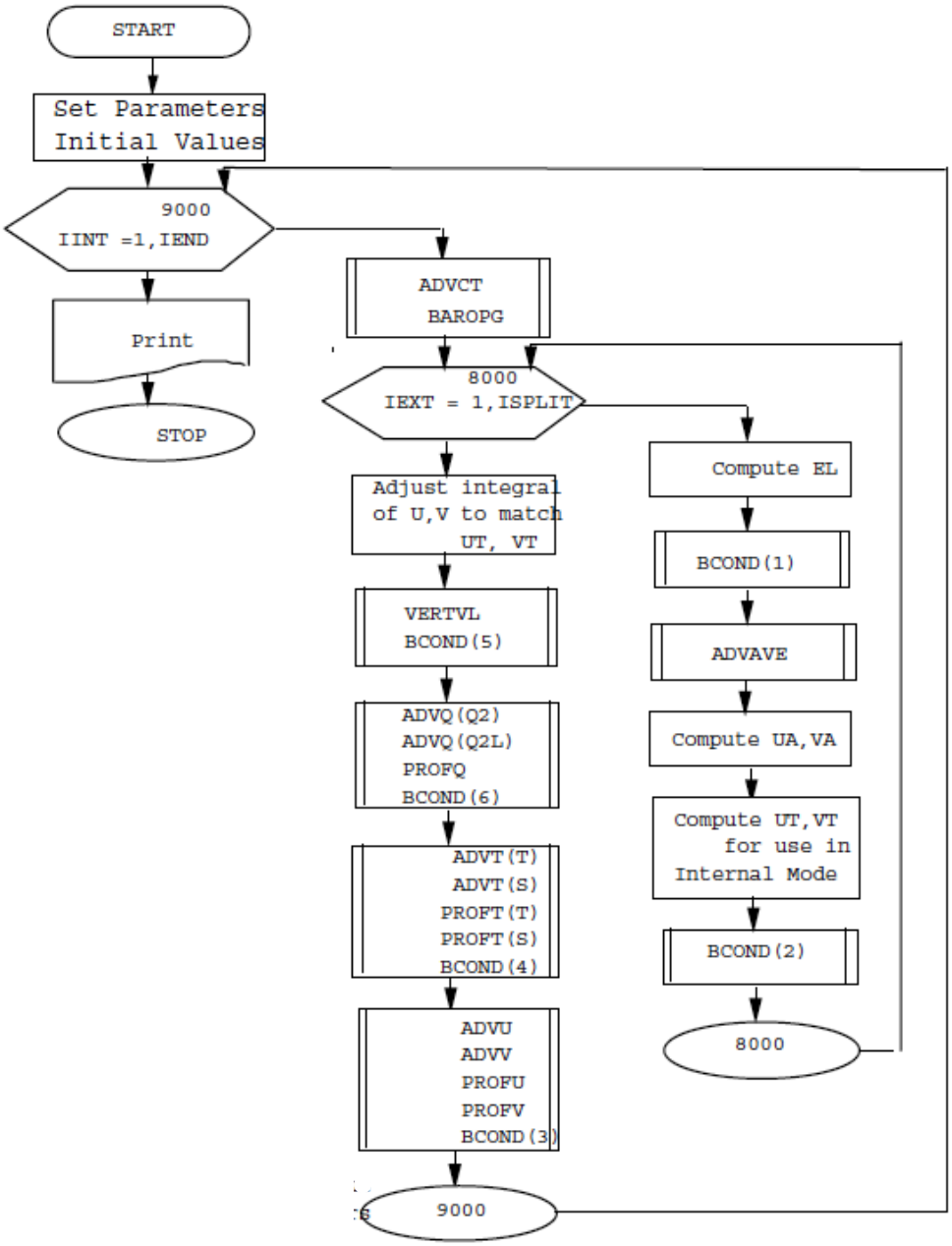

Figure 2.6: Flow diagram of the code (from Mellor, 2004).

due to inevitable numerical truncation and round off errors, which are not necessarily of the same magnitude in the two sets of calculations.

2.4 The pressure gradient error

Transformation to sigma-coordinates causes two vexing problems: the artificial purely numerical diffusion along isopycnals, brought about by the form for the horizontal diffusion terms, and spurious currents in the water column along topography, produced by truncation errors in calculating the baroclinic pressure gradients across sharp topography changes such as the continental slope. The former can produce a spurious vertical transfer of properties by diffusion along sigma surfaces, even when homogeneity prevails in the horizontal direction. To alleviate this problem, only anomalies from a horizontally homogeneous mean background state are retained in the horizontal diffusion terms of temperature and salinity (Mellor et al., 1994); thus before these terms are computed, an area-averaged mean value is subtracted, so that horizontal homogeneity would lead to zero diffusion (see previous section). Nevertheless, spurious diapycnal diffusion due to the inclination of isopycnal surfaces to coordinate surfaces that is present in z-level models also plagues sigma-coordinates models in applications to the deep basins. The best remedy is to employ isopycnal diffusion schemes in the interior of the ocean, but this is yet to be implemented in a sigma-coordinates model.

The second problem can be illustrated more simply hereafter. The use of sigma coordinates, wherein the water column is divided into the same number of grid cells independent of depth, is attractive when dealing with bottom topography (Mellor et al. 1996). It has been seen that estuaries are

modelled rather well (Oey et al., 985a,b; Galperin and Mellor, 990a,b); one needs to model the bottom boundary layer to correctly represent tidal mixing. Evidence is accumulating that sigma coordinates can accommodate rather sharp topographical changes that include a continental shelf with an adjacent shelf breack and deep ocean (Haidvogel et al., 1991; Ezer and Mellor, 1992) and seamounts (Ezer, 1994).

The source of the problem is that in the sigma-coordinate ocean models, the x-component of the internal density gradient may, after neglecting the free surface elevation, be written as

$$\left.\frac{\partial \rho}{\partial \mathrm{x}}\right|_{\mathrm{z}} = \frac{\partial \rho}{\partial \mathrm{x}} - \frac{\sigma}{\mathrm{H}} \frac{\partial \mathrm{H}}{\partial \mathrm{x}} \frac{\partial \rho}{\partial \sigma} \tag{2.26}$$

where x is the horizontal coordinate, z the vertical coordinate, ρ the density, H the depth, and $\sigma = \mathrm{z}/\mathrm{H}$. Near steep topography, the two terms on the right-hand side of equation (2.26) may be large and comparable in magnitude. The difference of two large terms may cause large errors in the estimates of the internal pressure gradient (Berntsen and Oey, 2010), a problem well known to atmospheric modelers (Gary, 1973, for example), but highlighted by Haney (1991) for oceanic applications. He notes, for example, that Rousseau and Pham (1971), Janjic (1997), and Mesinger (1982) have identified the related problem of "hydrostatic consistency" corresponding to:

$$\left| \frac{\sigma}{\mathrm{H}} \frac{\partial_{\mathrm{x}} \mathrm{H}}{\partial \sigma} \right| < 1 \tag{2.27}$$

where H is the depth; $\partial_{\mathrm{x}}\mathrm{H}$ is the horizontal change in depth of adjacent grid cells; and $\partial\sigma$ is the vertical cell size associated with a sigma grid cell, $\partial\sigma\partial$x. For non-zero σ, a σ-model becomes hydrostatically inconsistent when $\partial\sigma$ tends to zero. If (2.27) is not satisfied, the finite-difference scheme is pur-

portedly non-convergent. Haney concludes: "It is obviously essential to choose the horizontal and vertical resolution carefully, not only to accommodate the particular ocean problem at hand, but also to satisfy the hydrostatic consistency condition" (Mellor, 2004). Mellor (2004) derived the following discretization error for the second-order internal pressure method used in the POM:

$$E\left(\frac{\partial_x b}{\partial x}\right) = \frac{H}{4}\frac{\partial_x H}{\partial x}\left(\frac{\partial^2 b}{\partial z^2}\right)\left\{(\partial\sigma)^2 - \sigma^2\left(\frac{\partial_x H}{H}\right)^2\right\} \tag{2.28}$$

where $b = \rho g/\rho_0$, g is the gravity constant, and ρ_0 is a constant reference density. Equation (2.28) shows that the error decreases as $\partial\sigma$ and $\partial_x H$ both tend to zero, contrary to that implied by equation (2.27). It also shows that, for a given σ and $\partial_x H/H$, the error does not become large as $\partial\sigma$ tends to zero. Therefore, hydrostatic consistency is not a useful concept. The error term (2.28) suggests that the truncation errors may be reduced if higher-order schemes are used. Furthermore, the error behaviors may strongly depend on the particular discretization scheme used (Berntsen and Oey, 2010).

Mellor et al. (1994) showed that, in diagnostic experiments, the pressure errors are maintained in time as an input of potential energy; the mean kinetic energy does not tend to zero even if the system is not externally forced. However, in two-dimensional (x,z) prognostic experiments, the density field is advectively adjusted, the numerical potential energy tends to zero, and the mean kinetic energy accordingly dies out. Haidvogel et al. (1991) studied flow over a three-dimensional seamount. For their internal pressure gradient scheme, the vorticity resulting from the schemes grew indefinitely in time. For the same seamount problem, Mellor and Wang (1996)

reported that the errors asymptote to constants in time. Mellor and Wang (1996) categorized the errors reported in Mellor et al. (1994) as sigma errors of the first kind. These errors are associated with two-dimensional (x, z) flow. They categorized the vorticity errors reported by Beckmann and Haidvogel as sigma errors of the second kind; for this, the internal pressure errors create first errors in the velocities, which die out as a compensating error in the density field develops. For the sigma errors of the second kind case, the velocities driven by the perturbed density field asymptote to constant values in time.

The POM uses staggered grids in both the horizontal and the vertical directions leading to an effectively second-order spatial differencing scheme. The resulting pressure gradient errors cause spurious along-topographic currents even in ocean basins with horizontally homogeneous density distribution that is expected to be quiescent. In fact, a favourite ploy of modelers is to initialize their sigma-coordinate ocean model with a basin-averaged density profile, so that horizontal density gradients are automatically eliminated, and then perform a long-term integration without any external forcing to watch for any horizontal currents induced by topographic changes in the basin. If the currents induced are "small enough" in magnitude, subsequent calculations with surface forcing and the actual density field are regarded as acceptable (this is in fact what we have concluded in our model implementation, see section 4.2). The pressure gradient problem is reduced somewhat but not eliminated, by subtracting a reference horizontal average value from density before computing the pressure gradient.

Several methods have been suggested to reduce further the truncation errors to acceptable levels for sigma-coordinate model: smoothing topography (Chu and Fan, 2001), subtracting a mean vertical density profile before

calculating the gradient (Gary, 1973; Mellor et al., 1994), bringing certain symmetries of the continuous forms into the discrete level to ensure cancellations of these terms such as the density Jacobian scheme (e.g., Mellor and Wang, 1996; Song, 1998; Song and Wright, 1998), increasing numerical accuracy (e.g., McCalpin, 1994; Chu and Fan, 1997, 1998, 1999, 2000, 2001), changing the grid from a sigma grid to a z level grid before calculating the horizontal pressure gradient (e.g., Stelling and Van Kester, 1994). Kliem and Pietrzak (1999) claimed that the z-level based pressure gradient calculation is the most simple and effective means to reduce the pressure gradient errors. After comparing to other schemes, Ezer et al. (2002) show the favorable performance of the latest polynomial schemes. Shchepetkin and McWilliams (2003) design a pressure gradient algorithm with splines that achieves more accurate hydrostatic balance between the two components and that does not lose as much accuracy with non-uniform vertical grids at relatively coarse resolution (Chu and Fan, 2003). In conclusion, this section has been provided to explain the internal pressure gradient errors concept and the several methods suggested in the literature to reduce it.

Chapter 3

The surface wind forcing

3.1 Introduction

The ocean circulation is due to a combination of very complex phenomena depending on a series of physical mechanisms, and originates from fluxes occurring at the air-sea interface: they are the momentum fluxes (associated with the surface wind stress), the sensible and latent heat fluxes, evaporation and precipitation, and radiative forcing.

In a limited coastal area such as the one considered in this PhD thesis, the momentum fluxes provided by the action of the surface wind stress constitute the main atmospheric forcing, while the remaining forcing agents, that do affect the structure of the water column, can partly be taken into account in the initialization and nesting procedures (a complete analysis of these effects is beyond the scope of this work, and will be studied in the future in dedicated simulations). The forcing acting through the lateral boundaries of the domain of integration is also a very relevant effect, and is taken into account when boundary conditions provided by the Tyrrhenian Sea model are imposed in the one-way nesting procedure (see section 4.4). In conclu-

sion, in our model the surface wind forcing is the basic atmospheric forcing agent.

In sections 1.1 and 1.4 examples of ocean models forced by surface wind stress fields provided by meteorological models have been discussed. Such kind of wind product is ideal, in that it provides wind data regularly sampled in space and time over the sea surface. For example, the NMC (now "National Centers for Environmental Prediction" - NCEP) data were used in Pierini and Simioli (1998), while the "European Centre for Medium Range Weather Forecast" (ECMWF) data were used in Pierini et al. (2004) and Napolitano et al. (2013). On the other hand, in Pierini et al. (2004) the use of an alternative, higher resolution wind product derived from an ad hoc "limited area model" (LAM) implementation of an atmospheric model showed that the simulation of the marine circulation can improve, especially as far as intense meteorological phenomena are concerned (e.g., see Fig. 1.21).

In this PhD research use has been made of ECMWF analysis model data that will be described in the next section. We did not use LAM winds because the main aim of the study was to achieve a complete and validated implementation of a sigma coordinate model in the area of interest, regardless of the wind forcing used; needless to say, the forcing of our model by LAM winds, when available, will be straightforward. Another reason to rely on ECMWF winds is that this is the wind product used by Napolitano et al. (2013) for their Tyrrhenian Sea model, with which nesting of our coastal model is performed.

In addition, wind data derived from X-band COSMO-SkyMed©Synthetic Aperture Radar (SAR) data have also been used. In section 3.1 and 3.2 the retrieval of these new data, and their comparison with more classical satellite scatterometer winds, and ECMWF winds will be presented. In

section 5.3 the construction of a blended wind product including COSMO-SkyMed©SAR data based on ECMWF winds will be presented, and the results obtained by forcing our model with those winds will be discussed.

These results have been obtained within the framework of a COSMO-SkyMed©Italian Space Agency (ASI) project, and the resulting publication of Montuori et al. (2013) is integral part of this PhD research activity.

3.2 Satellite wind data

Accurate and appropriate measurements of the wind vector field over the sea surface are of great relevance in the oceanographic, meteorological and climatic research, and for the improvement of short-term forecast and warning. In fact, as already pointed out in section 3., the wind is a key parameter in the momentum exchange between the atmospheric boundary layer and the sea surface, which in turn drives the circulation and mixing of seawater (e.g., Vallis, 2006). The capability and the increasing need to retrieve the wind field at sea with both high spatial-temporal resolution and continuity can improve the modeling of the ocean circulation, especially in coastal areas, where the changes of the local winds may depend on the local coastal orography and land/sea thermal conditions.

The wind field over the sea surface is classically inferred by means of either meteorological models or in situ measurements, which unfortunately suffer from both technical and physical constraints that severely affect spatial-temporal coverage and resolution of the resulting wind field product. In addition to these widely used wind field data, microwave remote sensing has shown the capability of providing sea surface wind fields with mesoscale resolution and with short revisiting time. Within such a framework, the

key sensor is the active satellite-based microwave Scatterometer, which provides wind field measurements at sea by means of a non-linear inversion scheme, which requires both an accurate tailored Geophysical Model Function (GMF) and an appropriate set of sea surface normalized radar cross-section (NRCS) measurements at different azimuth angles (Bentamy et al., 1999; Migliaccio and Reppucci, 2006). The GMF, which is not a "universal model", relates the NRCS measurements of the sea surface roughness to the local wind field at sea, taking into account both the specific sensor parameters (e.g. polarization, frequency, incidence angle, etc.) and sea state conditions. Actually, scatterometer-based missions, such as the QuikSCAT (unavailable after November 2009) and the Advanced Scatterometer (ASCAT) ones, have been providing operational wind products with a spatial gridding resolution ranging from 25 km $\times$ 25 km to 12.5 km $\times$ 12.5 km, respectively (Yang et al., 2011). These products are not properly suitable for some marine applications, especially in coastal and near shore areas, where they suffer from uncertainty and large wind field estimation errors due to their large footprint (Bentamy et al., 1999; Migliaccio and Reppucci, 2006; Yang et al., 2011).

In this context, the possibility to retrieve the sea surface wind field from SAR images, with high resolution and in areas where the scatterometer measurements fail, is very interesting from an operational viewpoint. SAR is an active, microwave, band-limited sensor able to provide day-and night-time high-resolution NRCS measurements of the observed marine scenes with a synoptic view, and almost independently of atmospheric conditions (Jackson and Apel, 2004; Migliaccio and Reppucci, 2006). It has long been known that the wind field generates an anisotropic sea roughness, which can in principle be explained by means of a two-scale scattering model (Nunzi-

ata et al., 2007), where both centimeter resonant waves and long waves can be directly and indirectly observed, respectively. The physical interaction between the electromagnetic waves and the sea surface at the SAR resolution scale is generally nonlinear, and accounts for complex interactions between the sea surface and atmosphere (Jackson and Apel, 2004). This makes the physical problem much more complicated than the scatterometer one. However, the use of SAR measurements allows one to resolve the wind co-location problem, which generally introduces further errors, as in the case of SAR oil spill monitoring. Moreover, the high-spatial and temporal resolution provided by each SAR sensor, together with both the ground coverage and the short revisit-time provided by the recently-launched SAR constellations, make this sensor a key alternative source of sea surface wind field information able to integrate classical wind field estimation techniques, such as meteorological models, in situ observations and scatterometers.

In connection with the SAR-based wind field retrieval at sea, the use of X-band COSMO-SkyMed©(CSM) SAR data is highly innovative. The Italian Space Agency CSM is a constellation of four satellites equipped with X-band SARs, which ensures both wide area coverage and a small revisit time (Italian Space Agency, 2007). Among the different CSM SAR acquisition modes, i.e. Spotlight, StripMap and ScanSAR modes, the ScanSAR Huge Region mode is very interesting from an operational viewpoint, especially for both coastal circulation and oceanographic applications. In fact, it allows achieving a large ground coverage of about 200 km $\times$ 200 km with a spatial resolution of 100 m $\times$ 100 m in both range and azimuth directions (Italian Space Agency, 2007). However, the sea surface wind field estimation through X-band SAR measurements is a non-trivial task since, at higher frequencies, severe weather conditions and atmospheric phenomena dras-

tically compromise SAR image interpretations for sea surface wind field estimation purposes (Lee et al., 1995).

The innovative techniques developed to retrieve the wind vector from X-band CSM SAR data are presented in detail in Montuori et al. (2013). In summary, the SAR-based wind vector field estimation is accomplished by resolving both the SAR-based wind speed and wind direction retrieval problems independently. The sea surface wind speed is retrieved by means of a SAR wind speed algorithm based on the Azimuth cut-off procedure, while the sea surface wind direction is provided by means of a SAR wind direction algorithm based on the Discrete Wavelet Transform Multi-Resolution Analysis. The interested reader can refer to the original article.

3.3 ECMWF, scatterometer and COSMO-SkyMed SAR wind data intercomparison

In this section, some significant experimental results are presented, which are relevant to the sea surface wind vector field estimation over X-band VV-polarized Level 1B DGM ScanSAR Huge Region CSM SAR measurements and their subsequent comparison with both ASCAT scatterometer and ECMWF model wind fields (Montuori et al., 2013).

The X-band SAR data set consists of 60 X-band Level 1B DGM ScanSAR Huge Region mode VV-polarized CSM SAR data, gathered in a Southern Tyrrhenian coastal area during the summer and winter seasons of 2010 (Italian Space Agency, 2007). Each SAR acquisition provides ground coverage of about 200 km $\times$ 200 km with a spatial resolution of 100 m $\times$ 100 m and a pixel spacing of 50 m $\times$ 50 m, in both range and azimuth direction respectively.

The ECMWF analysis model data (used throughout this PhD research activity) have a horizontal resolution of $1/4^{\circ}$, which corresponds to ~ 27 km along a meridian and, in the area under consideration, to ~ 20 km along a parallel, and six hour of temporal resosolution. The ground truth, which is used as reference wind field for comparison purposes, is provided by timely and spatially co-located ASCAT scatterometer wind fields (with a spatial gridding resolution of 12.5 km $\times$ 12.5 km) and ECMWF analysis model data, respectively. Since both the ASCAT scatterometer wind field and the ECMWF model data are often not timely co-located with respect to the SAR image acquisition, a linear interpolation in time is accomplished between both the ground truth reference wind field data acquired before and after the SAR acquisition time, thus providing the timely co-located reference wind field.

A single experiment is fully detailed, with the aim of demonstrating the effectiveness of the X-band VV-polarized Level 1B DGM ScanSAR Huge Region mode CSM SAR data for sea surface wind field estimation purposes. The analysis is properly accomplished by comparing the X-band CSM SAR-derived wind speed and wind direction retrievals with respect to the reference ground truth. A SAR-based wind field retrieval gridding scale of 12.5 km $\times$ 12.5 km is considered. Therefore, the timely co-located reference ground truth provided by ECMWF model wind fields is bi-linearly interpolated in space over both the ASCAT scatterometer and the SAR-based wind field gridding scale, for comparison and validation purposes.

The experiment refers to the X-band CSM SAR acquisition of 20 November 2010 at 5:00 UTC. The VV-polarized NRCS image is shown in gray tones in Fig. 3.1(a). The output of the pre-processing step is shown in Fig. 3.1(b), where the scalloping, the atmospheric phenomena and other

non-homogeneous areas in the SAR image are successfully detected and removed from the homogeneous marine background.

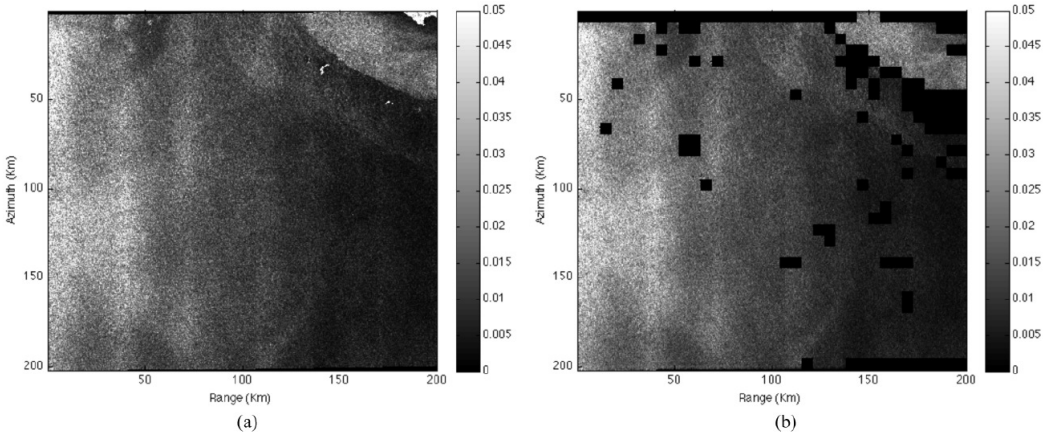

Figure 3.1: X-band Level 1B DGM ScanSAR Huge Region COSMO-SkyMed©SAR data acquired on 20 November 2010 at 05:00 UTC. (a) VV-polarized NRCS. (b) Output of the pre-processing step of the SAR wind field retrieval approach (from Montuori et al., 2013).

The timely and spatially co-located ASCAT scatterometer and ECMWF model wind speed data are shown in Fig. 3.2(a)-(b) respectively, where notable differences appear, especially along the coastal area. This result can be explained by considering the different spatial gridding resolution of the two different wind speed products, demonstrating that the ECMWF model data suffer from more uncertainty over the maritime coastal areas with respect to the ASCAT scatterometer wind speed. The output of the X-band CSM SAR wind speed retrieval approach based on the X-band Azimuth cut-off procedure is shown in Fig. 3.2(c). The comparison between the X-band SAR-based Azimuth cut-off wind speed estimation and the reference ground truth shows a fair agreement (especially with respect to the ASCAT scatterometer reference wind speed) with root mean square error (RMSE) values equal to 2.1 m/s and 4 m/s with respect to the ASCAT scatterometer and the ECMWF model wind speed, respectively. A further comparison is

provided between the ASCAT scatterometer and the ECMWF model wind speeds, which provides a RMSE value of 2.8 m/s. It can be noted that non-negligible differences in terms of sea surface wind speed are present along the coastal area of SAR image domain, for both the ASCAT scatterometer and the ECMWF model ground truth wind speed. This result takes into account that the reference wind speed data (especially the ECMWF model one) both suffers from uncertainty over the maritime coastal areas and it is not able to capture small-scale features, which can in turn be revealed by means of SAR data. Experimental results further demonstrate both the high-resolution accuracy of the ASCAT scatterometer wind speed with respect to the ECMWF model data (especially along the coastal areas) and the consistency of X-band CSM SAR-derived wind speed product especially with respect to the ASCAT scatterometer ground truth.

The output of the X-band CSM SAR wind direction retrieval approach based on the WT-MRA is shown in Fig. 3.2(d)-(e) together with the timely and spatially co-located ASCAT scatterometer and ECMWF model ground truth, respectively. The comparison between the X-band SAR-based WT-MRA wind direction estimation and the reference ground truth shows a fair agreement (especially with respect to the ASCAT scatterometer reference wind direction) with RMSE values equal to 16° and 24° with respect to the ASCAT scatterometer and the ECMWF model wind directions, respectively. A further comparison is provided between the ASCAT scatterometer and the ECMWF model wind directions (see Fig. 3.2f), which provides a RMSE value of 21°.

Moreover, in Fig.3.3 the three comparisons of Fig.3.2 are shown in geo-referenced maps in terms of the complete wind vector field. In conclusion, these results demonstrate both the high-resolution accuracy of the

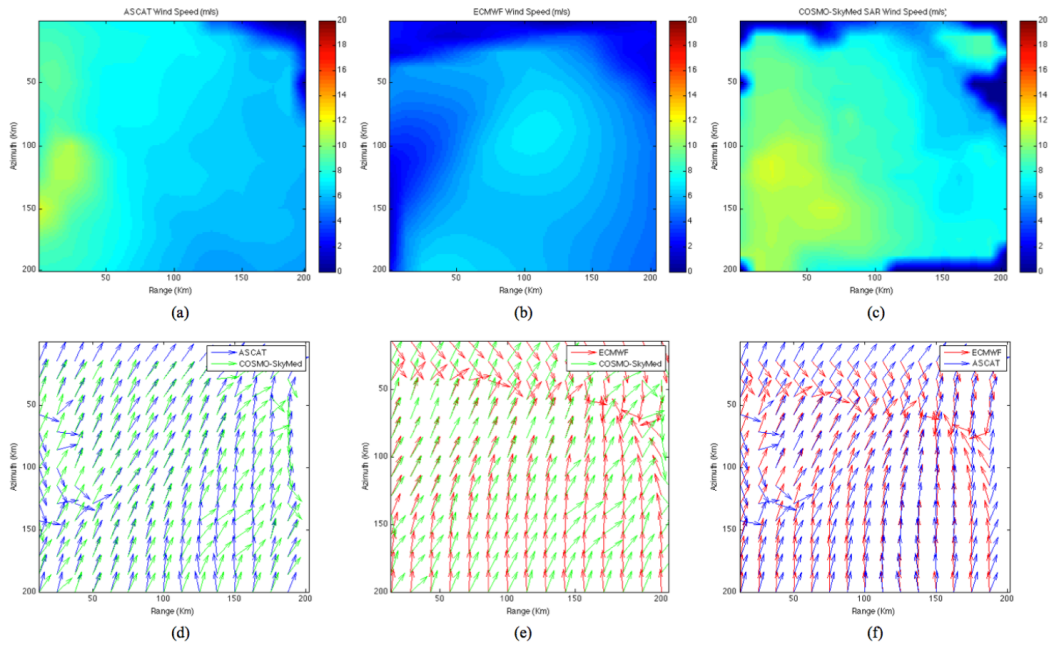

Figure 3.2: Wind field retrieval of the X-band VV-polarized Level 1B DGM ScanSAR Huge Region COSMO-SkyMed©SAR data acquired on 20 November 2010 at 05:00 UTC. (a) Reference ASCAT scatterometer wind speed. (b) Reference ECMWF model wind speed. (c) SAR-based wind speed estimation over a sub-image scale of 12.5 km $\times$ 12.5 km. (d) SAR-based wind direction estimation together with the reference ASCAT scatterometer wind direction. (e) SAR-based wind direction estimation together with the reference ECMWF model wind direction. (f) ASCAT scatterometer wind direction together with the ECMWF model data (from Montuori et al., 2013).

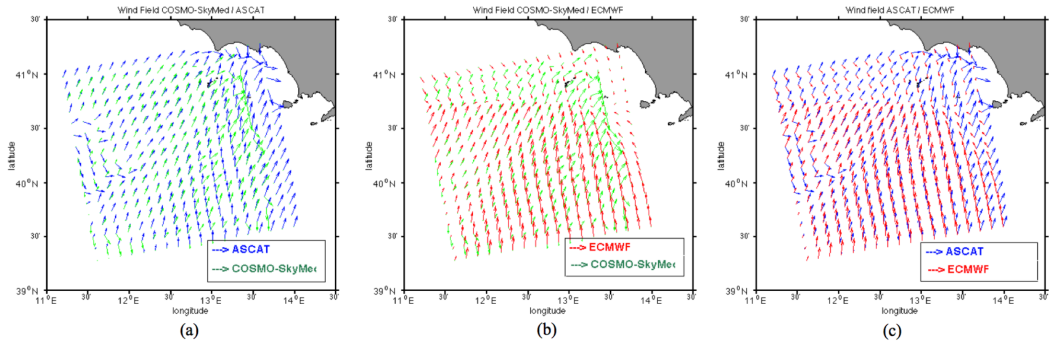

Figure 3.3: Georeferenced maps of the comparisons of Fig. 3.2d, e, and f in terms of the complete surface wind vector fields (from Montuori et al., 2013).

ASCAT scatterometer wind direction (especially along the coastal areas) with respect to the ECMWF model data and the consistency of CSM SAR wind direction retrievals, especially with respect to the ASCAT scatterometer winds.

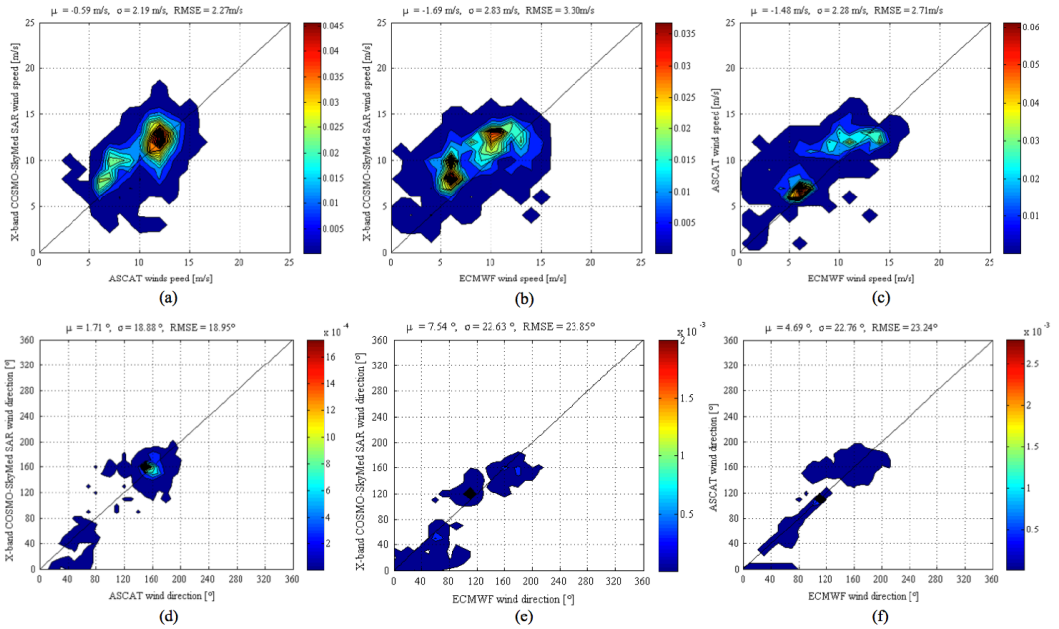

Figure 3.4: Probability density scatter plots of the comparison of the X-band COSMO-SkyMed©SAR derived wind field with ASCAT scatterometer and ECMWF model reference ground truth, by considering a sub-image gridding scale of 12.5 km ×12.5 km. (a) Scatter plot of COSMO-SkyMed©-ASCAT wind speed inter-comparison. (b) Scatter plot of COSMO-SkyMed©-ECMWF wind speed inter-comparison. (c) Scatter plot of ASCAT-ECMWF wind speed inter-comparison. (d) Scatter plot of COSMO-SkyMed©-ASCAT wind direction intercomparison. (e) Scatter plot of COSMO-SkyMed©-ECMWF wind direction inter-comparison. (f) Scatter plot of ASCAT-ECMWF wind direction inter-comparison (from Montuori et al., 2013).

Other meaningful results are summarized in Fig. 3.4 and Table 3.1 , where the three different wind field products (i.e., from SAR, scatterometer and model data) are properly compared for the whole processed CSM SAR data set. These results agree with the previous ones, thus demonstrating the effectiveness of both the X-band Azimuth cut-off model function and

	Variable					
	Wind Speed ($m\,s^{-1}$)			Wind direction (°)		
Product comparison	RMSE	μ	σ	RMSE	μ	σ
COSMO-SkyMed© SAR vs. ASCAT	2.27	−0.59	2.19	18.95	1.71	18.88
COSMO-SkyMed© SAR vs. ECMWF	3.30	−1.69	2.83	23.85	7.54	22.63
ASCAT vs. ECMWF	2.71	−1.48	2.28	23.24	4.69	22.76

Table 3.1: COSMO-SkyMed©SAR-ASCAT-ECMWF wind field products inter-comparison in terms of RMSE, μ and σ values (from Montuori et al., 2013).

the WT-MRA technique to obtain consistent wind speed and wind direction estimation, respectively, even through X-band SAR data. Furthermore, experimental results show the full benefits of X-band Level 1B DGM ScanSAR Huge Region mode CSM SAR data as an alternative source of wind field estimation.

Chapter 4

Model implementation

4.1 Integration domain, topography and surface wind forcing

In this chapter the implementation of our coastal model (COSM heretofore) is described. Several error tests and the one-way nesting with a large-scale Tyrrhenian Sea circulation model are also described in detail.

The domain of integration (Fig. 4.1) spans the range $\lambda = 13^\circ/15.36^\circ$ and $\phi = 40^\circ/41.43^\circ$. As already anticipated, it covers a southern Tyrrhenian Sea coastal area which includes the Gulfs of Gaeta, Napoli and Salerno, plus a wide outer buffer zone, which is required both to reduce boundary effects in the closed-boundary simulations, and to allow for a smooth nesting with the large-scale model. The model horizontal resolution is $1/144^\circ$ (with $\Delta y \approx$ 772 m, $\Delta x \approx$ 579-591 m, on a 342 $\times$ 192 grid) and the vertical discretization makes use of 40 sigma-levels (in section 4.4 this choice will be justified in connection with the one-way nesting with the Tyrrhenian Sea model). The temporal steps are Δ_{text} = 1 s and Δ_{tint} = 60 s. As for the bottom topography, the 30" GEBCO (General Bathymetric Chart of the Oceans) data are

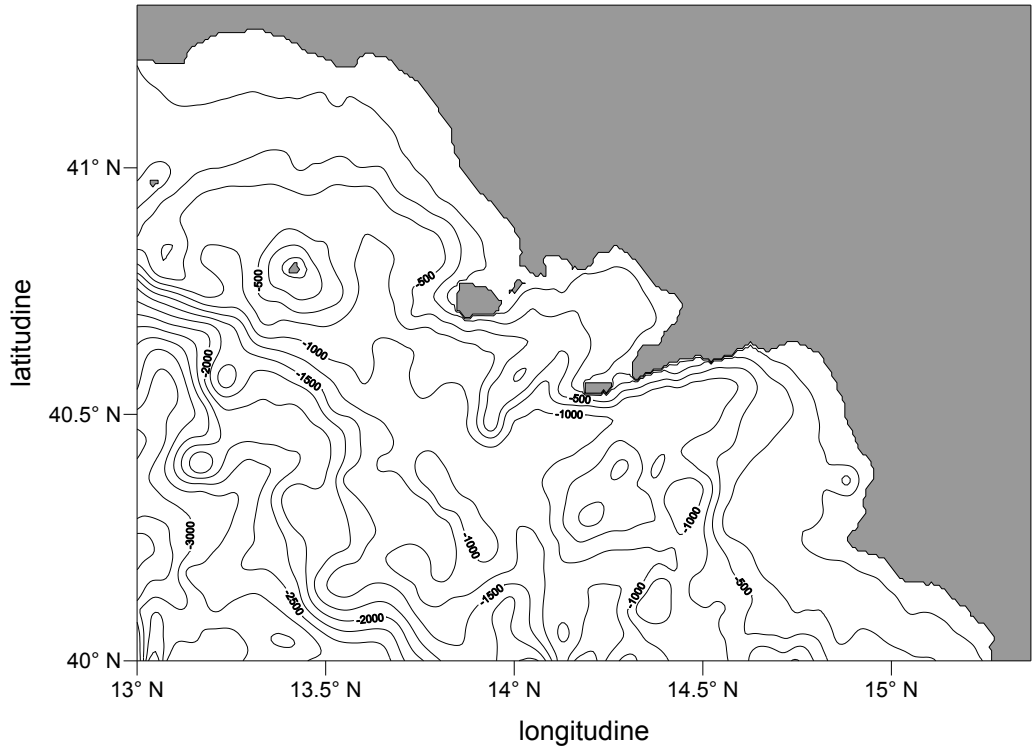

Figure 4.1: Domain of integration.

used (Fig. 4.2) [GEBCO operates under the auspices of the International Hydrographic Organization and the Intergovernmental Oceanographic Commission of UNESCO]. A Laplacian filter has been applied to the original bathymetry to provide a weak smoothing.

As for the wind forcing, a detailed discussion is presented in Chapter 3. In all the simulations the ECMWF analysis (ECMWF for short) surface wind data are used, but in the simulation of the month November 2010 also an alternative blended wind forcing is used in order to test CSM SAR wind forcing capabilities (see sections 3.3 and 5.3). The fully dynamically consistent ECMWF data (regularly sampled in space on a $1/4^\circ$ grid and in time with a 6 h temporal resolution) have been obtained in the window λ = -19°/48° and ϕ = 30°/42° for several test periods. The surface wind velocity data are transformed into surface wind stress by means of classical bulk

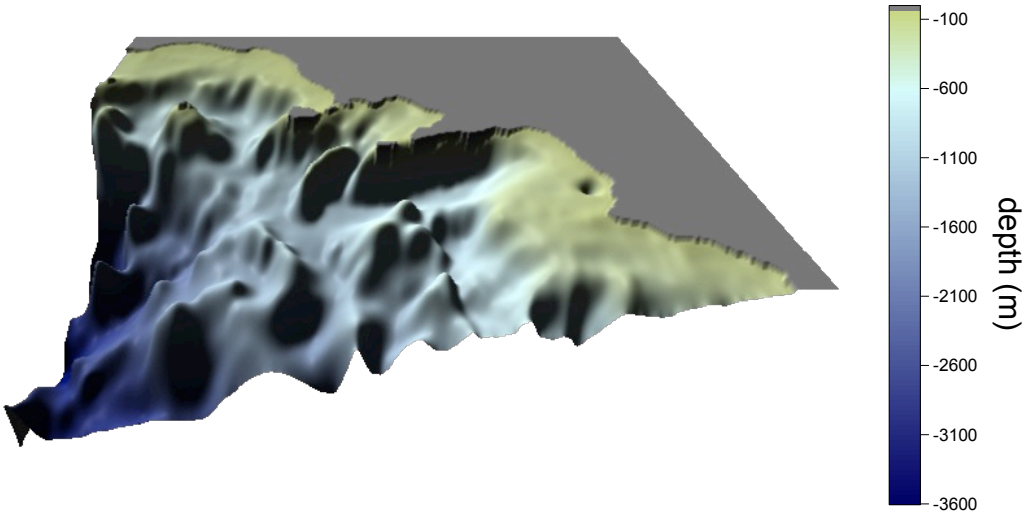

Figure 4.2: 3D view of the GEBCO topography inside the domain of integration.

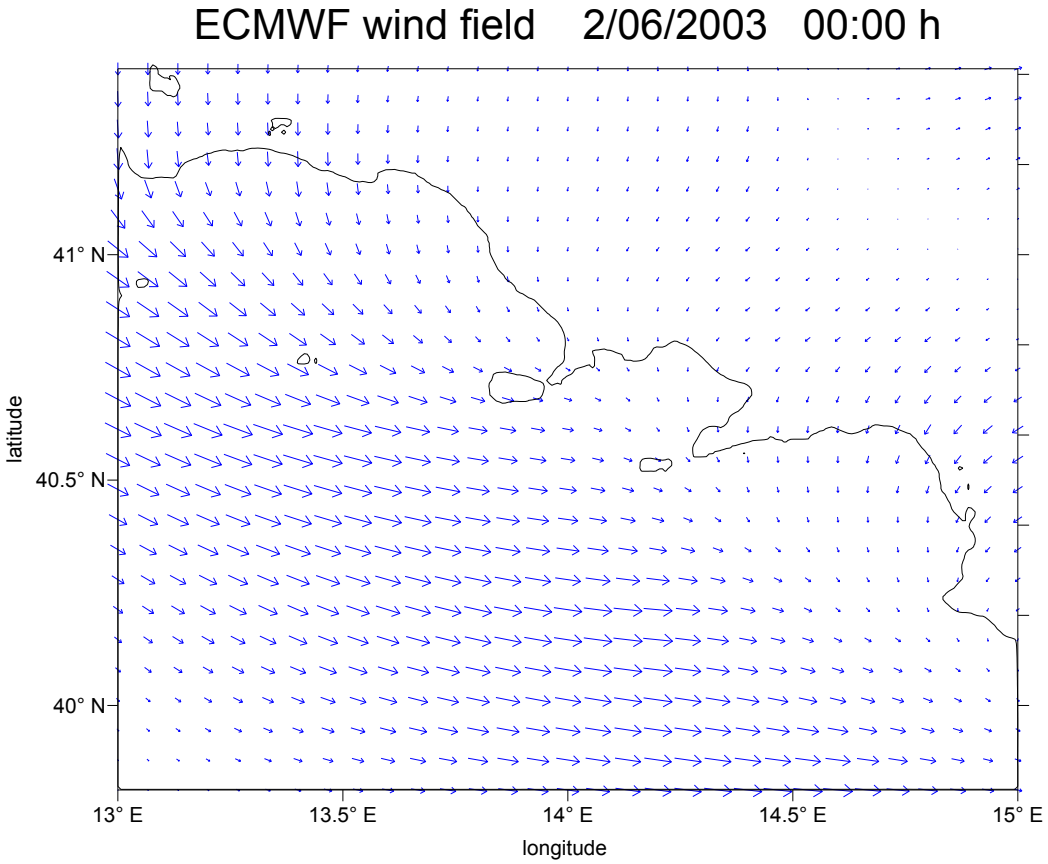

Figure 4.3: Example of ECMWF analysis surface wind velocity data interpolated onto the integration domain (June 2, 2003, 0:00 h).

formulae. The routines that interpolate this field bilinearly onto the model grid (at 10 m, see Fig. 4.3 for an example) and linearly in time in order to provide the actual model forcing have been developed, implemented and successfully tested for POM.

4.2 The sigma error test

In section 2.3 a detailed discussion of the internal pressure gradient error arising in POM (but common to all sigma coordinate models) was presented. To this respect, ad hoc tests were performed to assess whether such error is of sufficiently small amplitude. We checked that by running the model with vanishing forcing and with a homogeneous density (with T=15°C S=37.00 PSU) in the 40 sigma-levels: the result is shown in Fig. 4.4. The energy reaches immediately a very small constant value; the maximum current speed is less than 1 mm/s. The same sensitivity run was performed

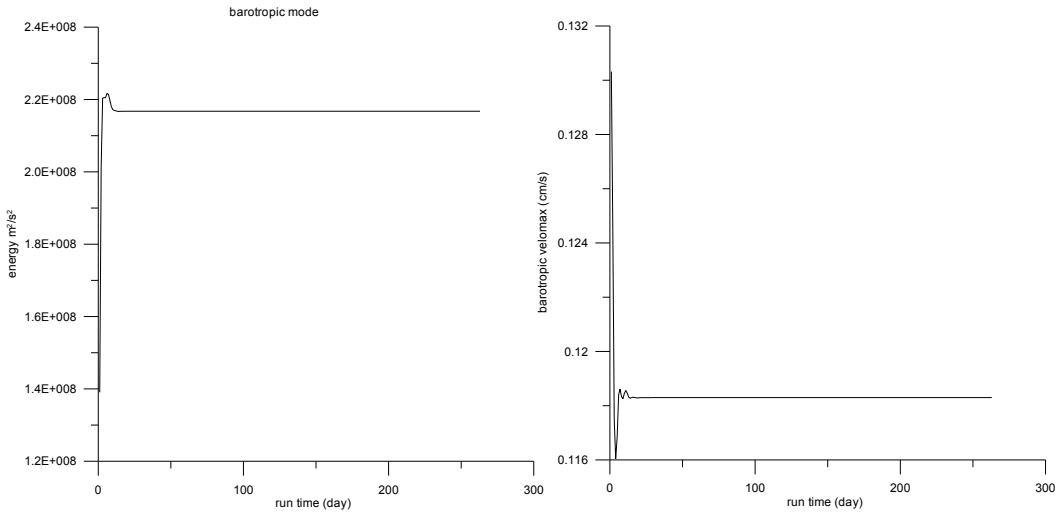

Figure 4.4: Total kinetic energy (left) and current speed (right) time series for the barotropic test.

with variable density (the stratification corresponds to the initialization of

June 2003 described in sections 5.4 and 6). The right panel of Fig. 4.5 shows that the maximum asymptotic current speed remains less than 5 mm/s. Thus, in both cases the gradient error is definitely negligible for our applications (such a good model performance is clearly due to the high resolution adopted). The conclusion is that the adopted topography does not require any further treatment.

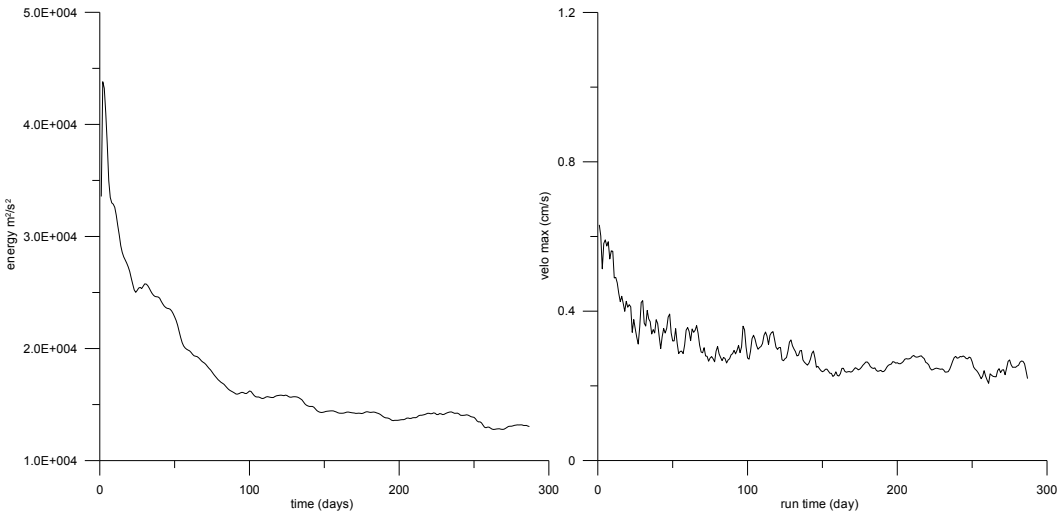

Figure 4.5: Total kinetic energy (left) and current speed (right) time series for the baroclinic test.

4.3 Barotropic simulations in the closed domain

As a necessary first step toward the construction of a realistic nested model configuration, simulations performed with closed boundary conditions (i.e., without nesting with the large scale model) must be carried out. In this section, simulations of this kind performed for summer and winter test periods in both barotropic and baroclinic conditions are described. The normal velocities along coastal boundaries and the landward tangential velocities in the horizontal friction terms are also set to zero (Mellor, 2004); at

the bottom, a quadratic bottom friction dominates over lateral friction, that is calculated by combining the velocity profile with the logarithmic law of the wall, with a prescribed drag coefficient (Sannino et al., 2004).

In meteorology and oceanography "barotropic" is a term denoting a condition in which isobaric and isopycnic surfaces coincide, which implies the independence of the geostrophic velocity on the vertical; on the contrary, "baroclinic" denotes a condition in which isobaric and isopycnic surfaces do not coincide, which implies that a relative pressure gradient exists that produces the so-called "thermal wind", "baroclinic compensation" and corresponding depth dependent geostrophic velocities. In a homogeneous (constant density) ocean only the barotropic condition is obviously allowed, while if the ocean is stratified both barotropic and baroclinic conditions are allowed (of course, the latter is the most typical case). In oceanographic modeling, the barotropic condition schematizes, sometimes quite realistically, winter conditions in shallow coastal waters, when surface cooling and strong winds produce the deepening of the surface mixed layer and the erosion of the seasonal thermocline, leading to a virtually constant-density fluid. The barotropic condition is usually the first one to be tested in a model implementation (disregarding the corresponding limited degree of realism), since it does not require any hydrological initialization, but it may nonetheless present technical problems because, since currents are strong even close to the bottom, vigorous topographic interactions must be dealt with.

Vertical turbulent mixing processes are parameterized with the 2.5-order turbulence closure sub model scheme named Mellor-Yamada 2.5 (Mellor and Yamada, 1982). In COSM a modification of this closure scheme proposed by Kantha and Clayson (1994) is included, as in Napolitano et al. (2013) .

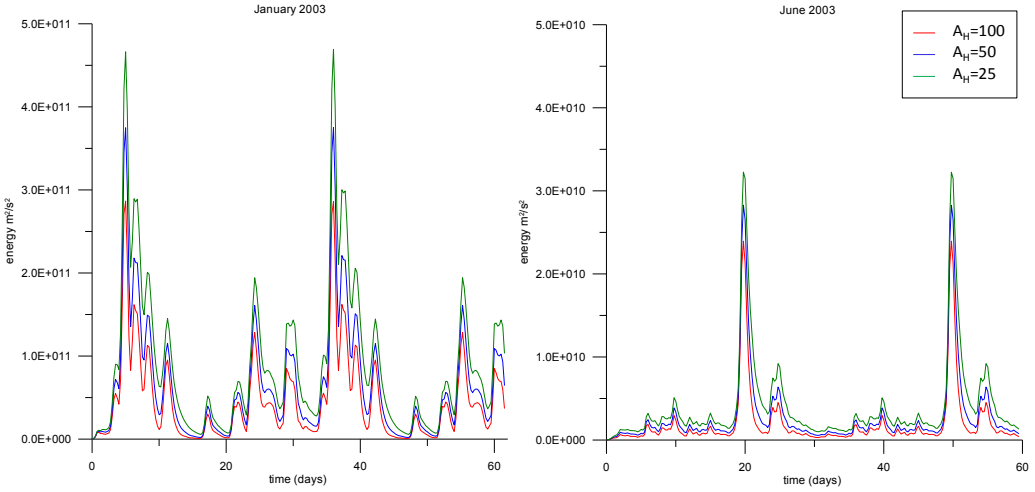

Figure 4.6: Time series of the integrated kinetic energy of the system for January 2003 (left panel) and for June 2003 (right panel) for three different values of the lateral eddy viscosity coefficient.

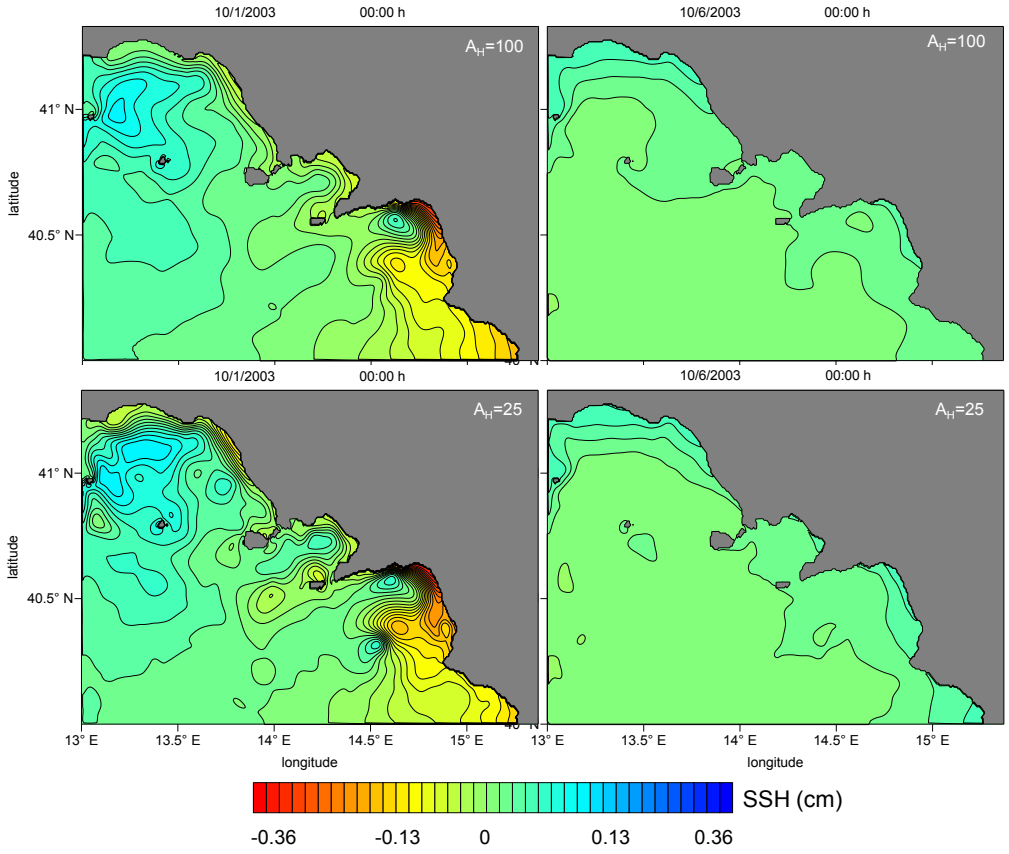

Figure 4.7: Examples of maps of the sea surface elevation for January 10, 2003, 10.00 h (left panel) and June 10, 2003, 00:00 h (right panel) for two different values of the lateral eddy viscosity coefficient.

Examples of barotropic simulations are now presented. Fig. 4.6 shows the time series of the kinetic energy integrated over the whole domain for winter (January 2003) and summer (June 2003) winds for three different values of the Laplacian lateral eddy viscosity coefficient (this provides useful information on the sensitivity of the circulation to this specific dissipative parameter). The simulations are run for a two-month period under the same monthly wind field repeated for two subsequent times (the so-called "perpetual" forcing): this evidences that the system spins up in a very short period, of the order a 1-2 days. Fig. 4.7 shows two snapshots of the sea surface elevation (which closely represents the barotropic streamfunction) for both January and June 2003.

4.4 Baroclinic simulations in the closed domain

We now move to the discussion of more realistic baroclinic simulations, for which the water properties have, in general, a three-dimensional dependence, so that baroclinic compensation, but also internal gravity, Kelvin, and (topographic) Rossby waves are all resolved by the model. In this section we present simulations in which the stratification is idealized and horizontally homogeneous, so that the model behavior can be tested in a relatively simple dynamical context.

The same simulations carried out for the barotropic case (section 4.2) have been carried out also for the baroclinic case with the temperature and density profiles shown in the lower-right panels of Figure 4.8 and 4.9 for January and June 2003, respectively (the salinity has the constant value 37.00 PSU). The snapshots corresponding to 10 January 2003, 0:00 h (Fig. 4.8) and 10 June 2003, 0:00 h (Fig. 4.9) are shown in the lower left panel for the sea

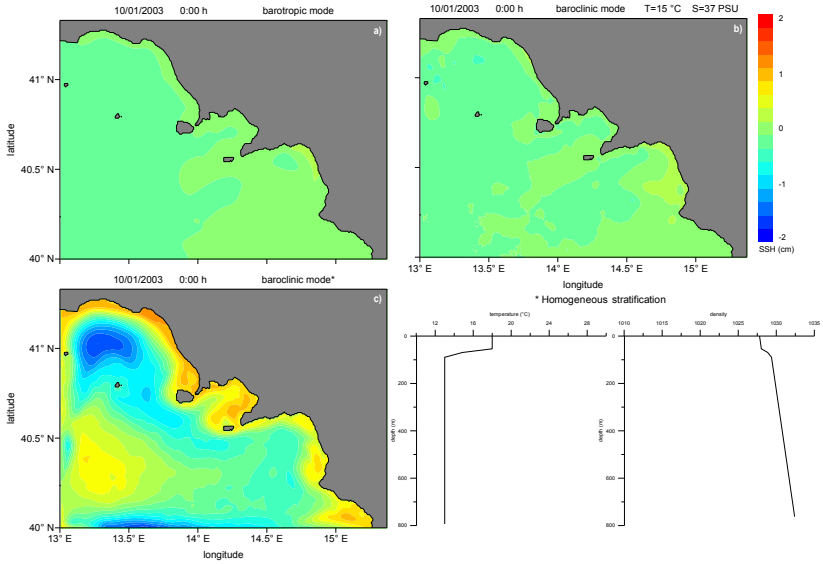

Figure 4.8: Snapshots (10 January 2003, 0:00 h) of the sea surface height of January 2003-ECMWF perpetual runs obtained in the barotropic mode (a), in the 40-sigma level baroclinic mode with constant density (b) and the 40-sigma level baroclinic mode with variable density (c); the temperature and density profiles used in this last case are shown in the lower right panel.

surface height.

In addition, in the upper panels of the two figures the result of the barotropic run (left) and that of the baroclinic run with constant density (right) are shown. It is important to note that these two maps are virtually coincident: this is because they represent two physically identical conditions and the model gradient error is, in fact, negligible.

Figure 4.10 shows the time series of the kinetic energy integrated over the whole domain for the January 2003 and June 2003 baroclinic runs with variable density (see Fig. 4.8 and Fig. 4.10). In addition, the Smagorinsky formula was used (see equation 2.12 in section 2; the horizontal momentum small-scale mixing processes are parameterized as horizontal diffusion (along sigma surfaces) depending on the horizontal velocity shear and on the grid spacing via the Smagorinsky, 1963 diffusion scheme).

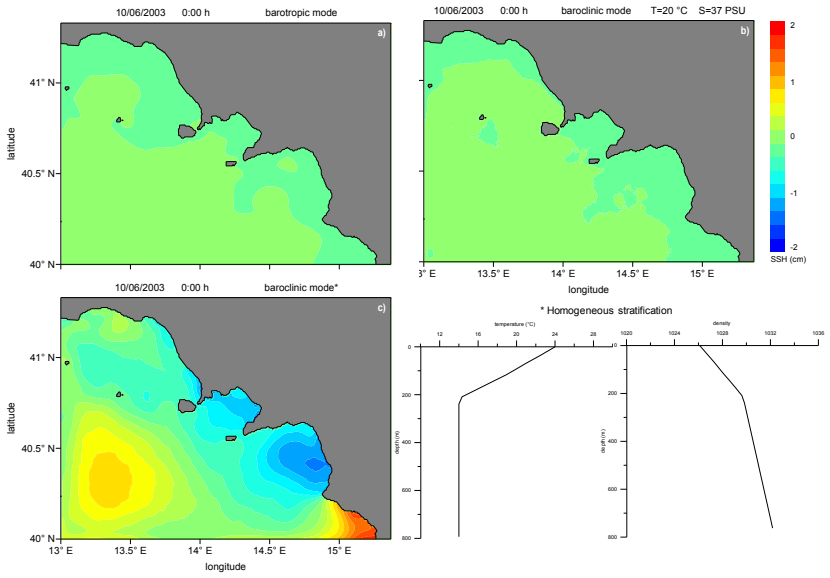

Figure 4.9: Snapshots (10 June 2003, 0:00 h) of the sea surface height of June 2003-ECMWF perpetual runs obtained in the barotropic mode (a), in the 40-sigma level baroclinic mode with constant density (b) and the 40-sigma level baroclinic mode with variable density (c); the temperature and density profiles used in this last case are shown in the lower right panel.

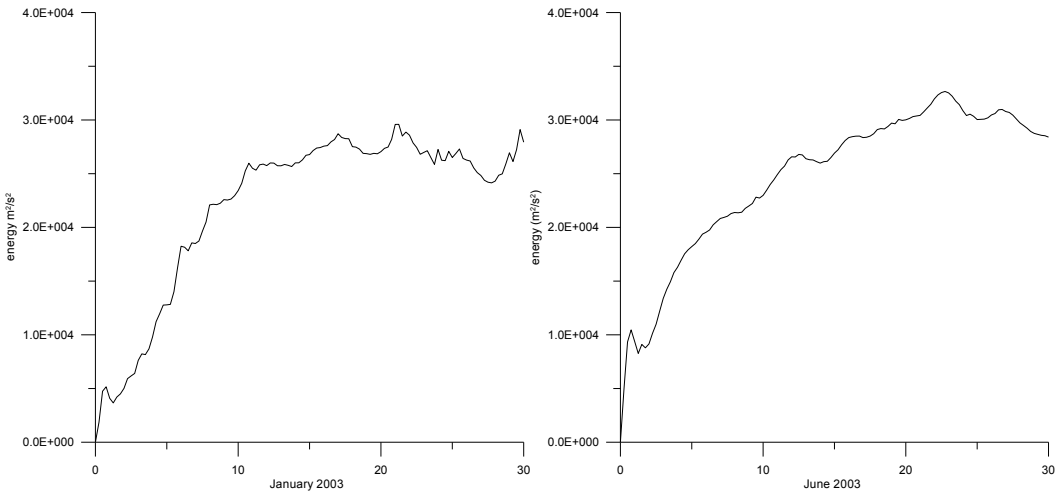

Figure 4.10: Time series of the integrated kinetic energy of the system for January 2003 (left panel) and for June 2003 (right panel) obtained in the run with 40-sigma levels in the baroclinic mode with variable density.

To describe in more detail the baroclinic structure of the simulations with horizontally homogeneous stratification, in Fig. 4.11 the current velocities at 100, 300 and 500 m depth are shown (at every 3 grid points along both x and y) for the January and June 2010 simulations. Moreover, the vertical profiles of the zonal (u) and meridional (v) current velocity components at the point indicated in Fig. 4.12 are shown in Fig. 4.13 corresponding to the snapshots of Fig. 4.11. Fig. 4.14 shows the time series of zonal (u) and meridional (v) surface velocity components and of the sea surface elevation at the same point. We conclude this section devoted to simulations in the closed domain by showing the capability of POM to provide hydrological and dynamical information that can be potentially validated with hydrological measurements performed with research vessels. As an example, in Fig. 4.15 two snapshots of a longitudinal transect of the meridional velocity for typical winter and summer conditions are shown. In the subsequent Fig. 4.16 a zoom on the upper 200 m is reported. These are good examples of how the adopted sigma coordinate model can provide valuable information on the vertical structure of the marine environment under investigation. In conclusion, the numerical results presented in this section are both qualitatively and quantitatively compatible with theoretical requirements, and insure the correct implementation of the model with realistic topography, forcing and hydrological structure. To obtain a fully realistic performance, however, the nesting with the large scale Tyrrhenian Sea model is necessary. This part of the research will be presented in the next section.

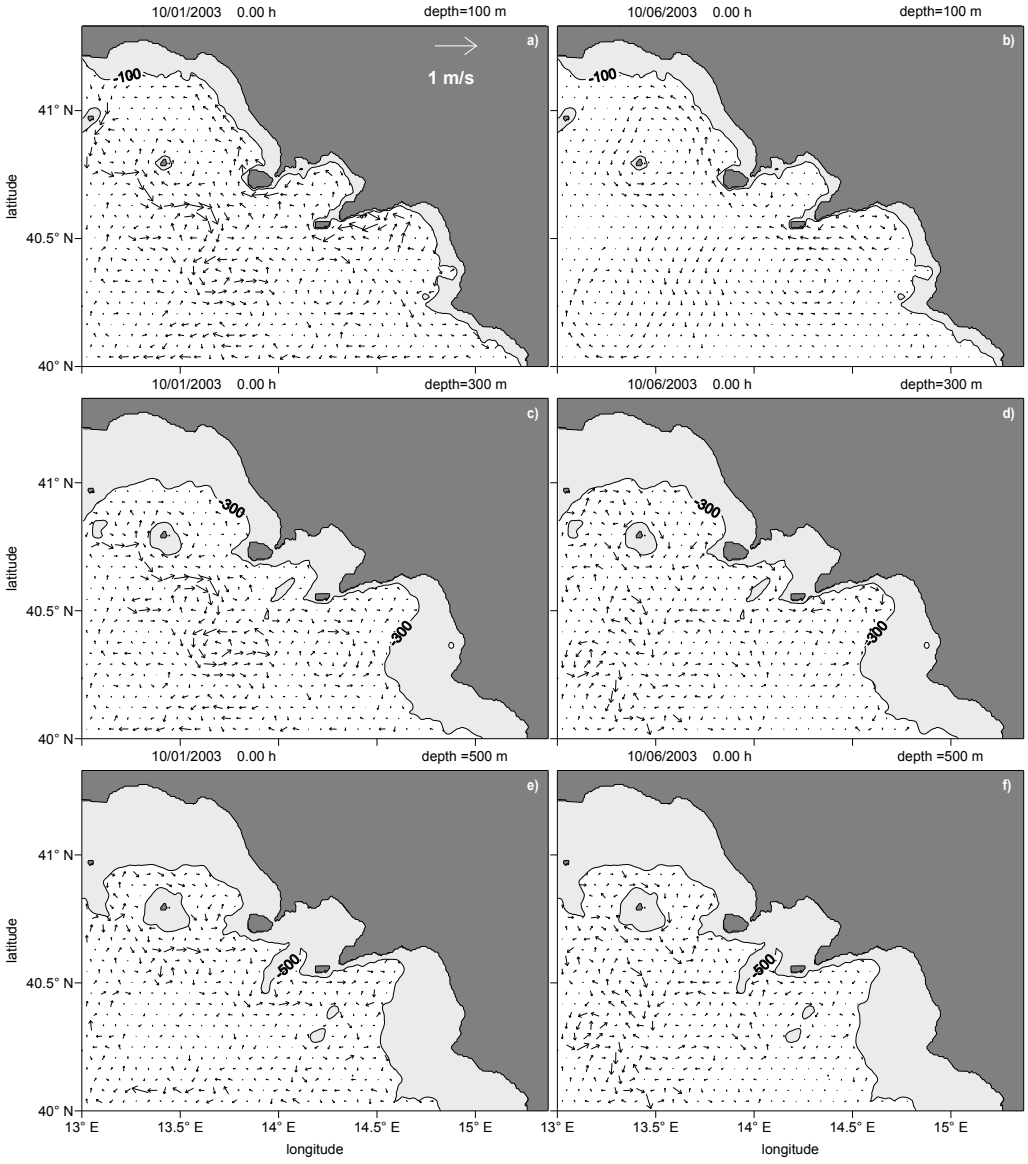

Figure 4.11: Current velocities at 100, 300 and 500 m depth on 10 January 2003 (a,c,e) and on 10 June 2003 (b,d,f) at 0:00 h. Only the arrows at each every 9 grid points along both x and y are shown.

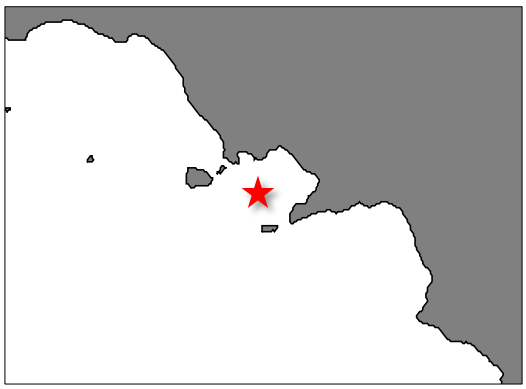

Figure 4.12: Point where currents are analyzed.

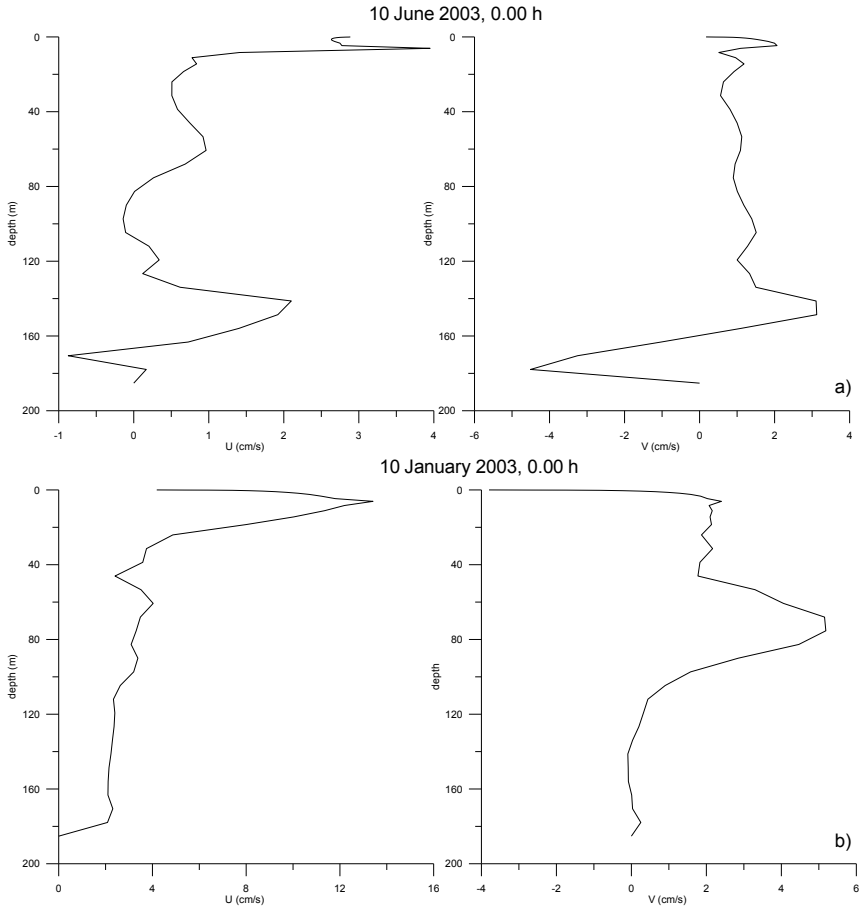

Figure 4.13: Vertical profiles of the zonal (u) and meridional (v) current velocity components in the point indicated in Fig. 4.4.5 on 10 June 2003, 0:00 h (a) and on 10 January 2003, 0:00 h.

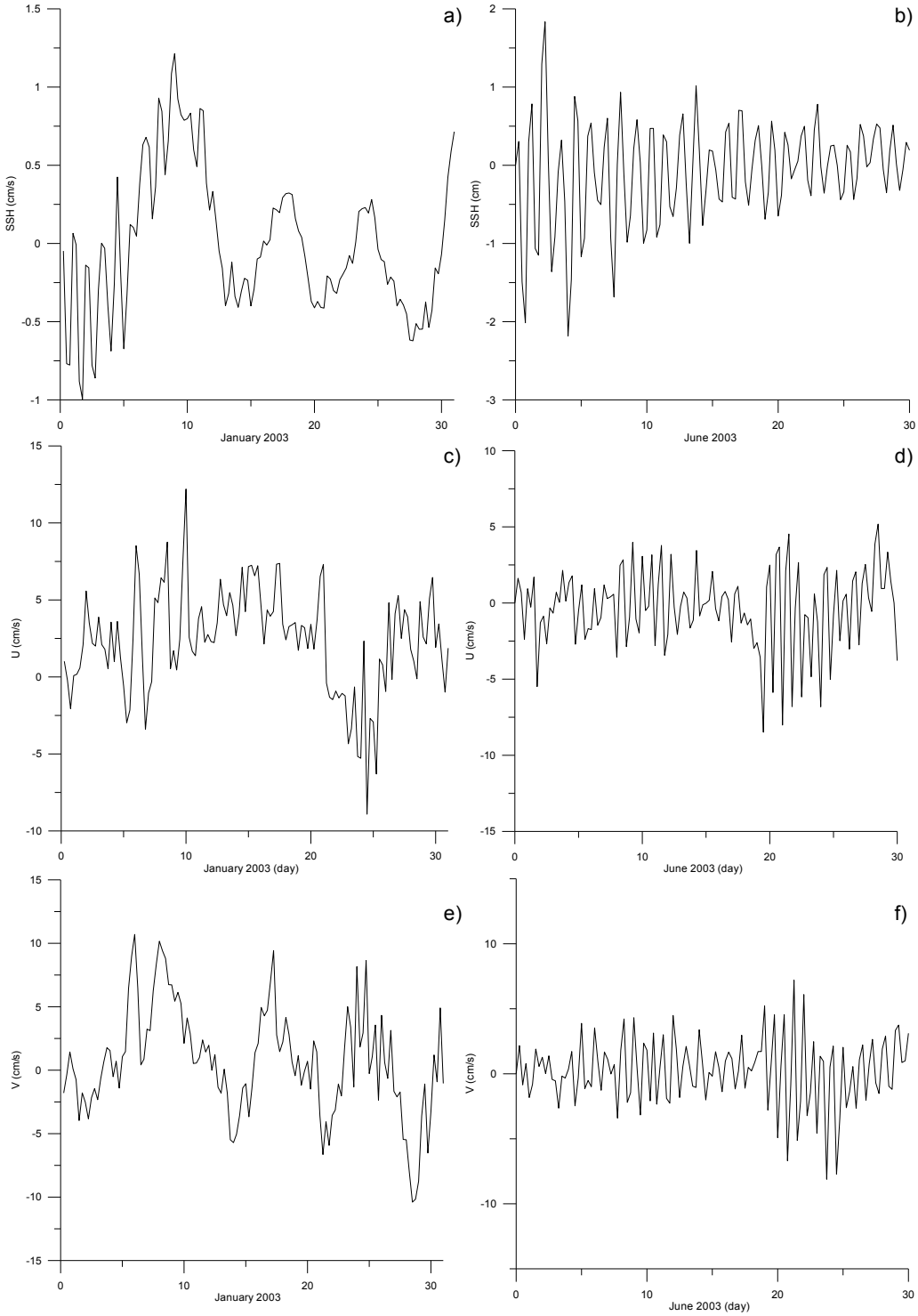

Figure 4.14: Time series of the sea surface elevation and surface velocity components (u,v) for January 2003 (a, c, e) and June 2003 (b, d, f) baroclinic runs with variable density (see Figure 4.8 and 4.9) in point of Figure 4.12.

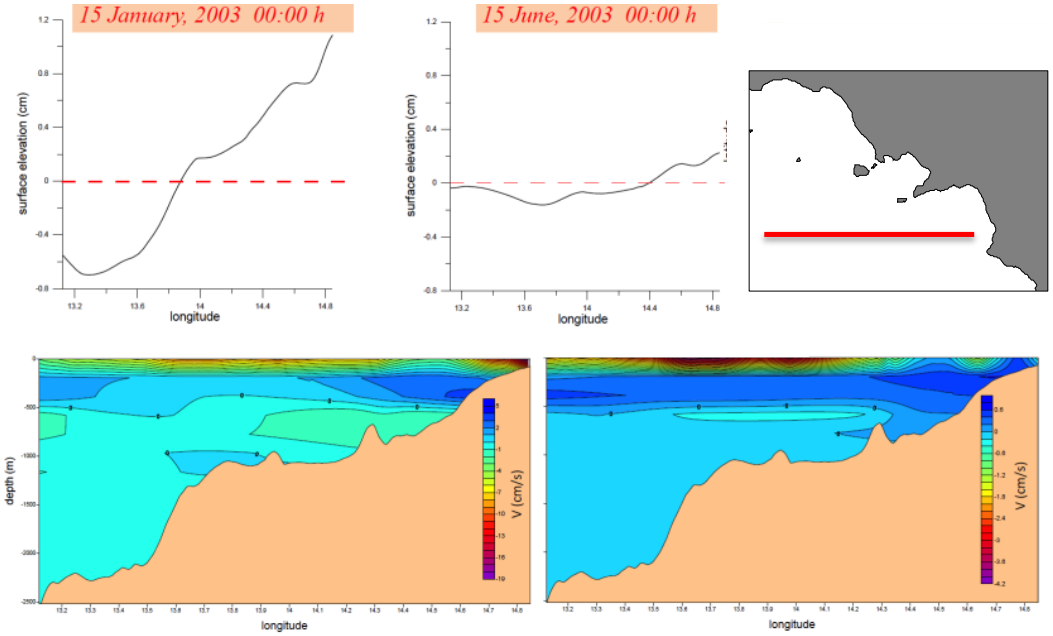

Figure 4.15: Snapshots of a longitudinal transect of the meridional velocity for typical winter and summer conditions.

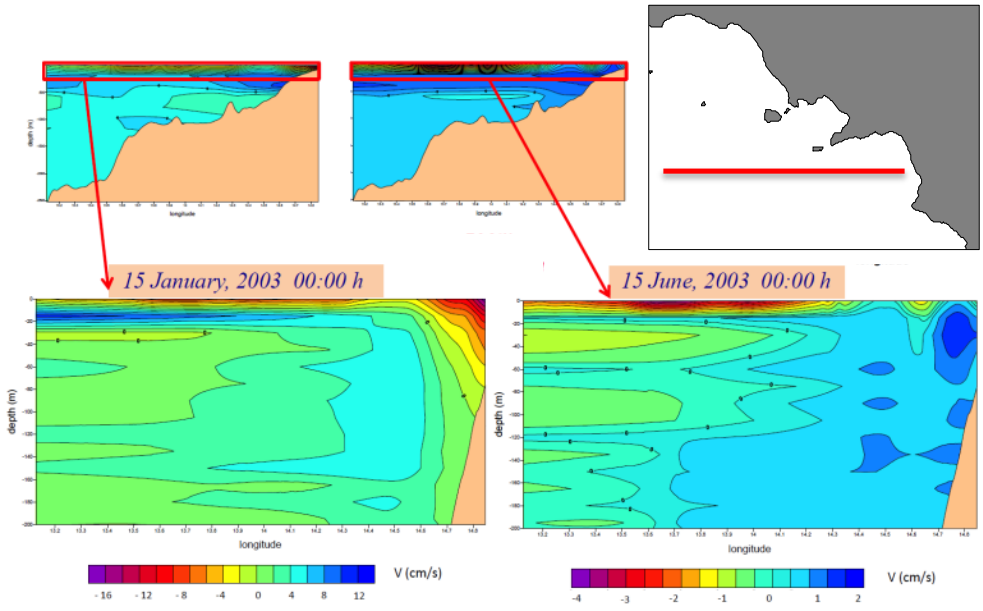

Figure 4.16: As in Figure 4.15, but with a zoom on the upper 200 m.

4.5 One-way nesting with a Tyrrhenian Sea circulation model

As already pointed out, to obtain a fully realistic performance of the coastal model, the nesting with a Tyrrhenian Sea model (TSM heretofore) must be accomplished.

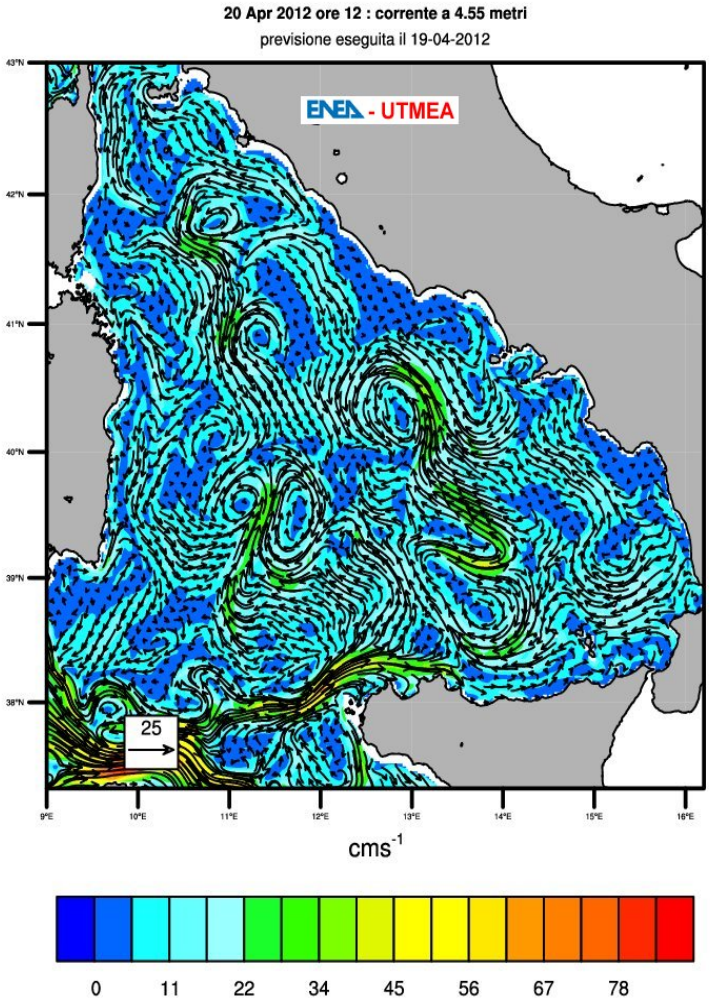

Figure 4.17: Surface current and free surface fields example obtained by the Tyrrhenian Sea POM model of Napolitano et al. (2013).

In the one-way nesting the exchange of information is from a coarser resolution "father" model to a higher resolution coastal model; on the con-

trary, the smaller scale dynamics generated by the latter does not provide a feedback to the former, as it would be the case in a two-way nesting strategy, which would obviously involve a much higher degree of complexity. In our one-way nesting the initialization of the hydrological and dynamical structure of the COSM is taken from the TSM, and the dynamical boundary conditions imposed along the open lateral boundaries are also derived from the TSM.

The latter is in our case provided by the $1/48^\circ$-resolution POM implementation of Ernesto Napolitano and Roberto Iacono, of the ENEA-Casaccia climate modeling group (Napolitano et al., 2013; see section 1.1 and Fig. 1.8 therein). The Tyrrhenian Sea model is, in turn, nested with the NEMO-OPA (Nucleus for European Modelling of the Ocean-Ocean PArallelise) implemented in the Mediterranean Sea at $1/16^\circ \times 1/16^\circ$ horizontal resolution and 71 unevenly spaced vertical levels (Oddo et al., 2009). The nesting follows the approach of Zavatarelli and Pinardi (2003). The TSM model is operational providing forecasts every hour on the web (`http://utmea.enea.it/`), Fig. 4.17 shows an example of forecast.

As already stressed, the choice of scaling the two resolutions by a factor 1/3 has the advantage of allowing for a smooth nesting; also the choice of having only two "open" boundaries inside the Tyrrhenian Sea simplifies the nesting procedure. As for the bottom topography, a correct nesting requires that the two topographies are consistent. Fig. 4.18-4.19 show that this is in fact the case.

The one-way nesting procedure consists of two steps: the initialization of the COSM and the imposition of the lateral boundary conditions. The initialization requires several technical steps that are now briefly outlined. All the fields taken from the TSM are averaged over a certain month. These tem-

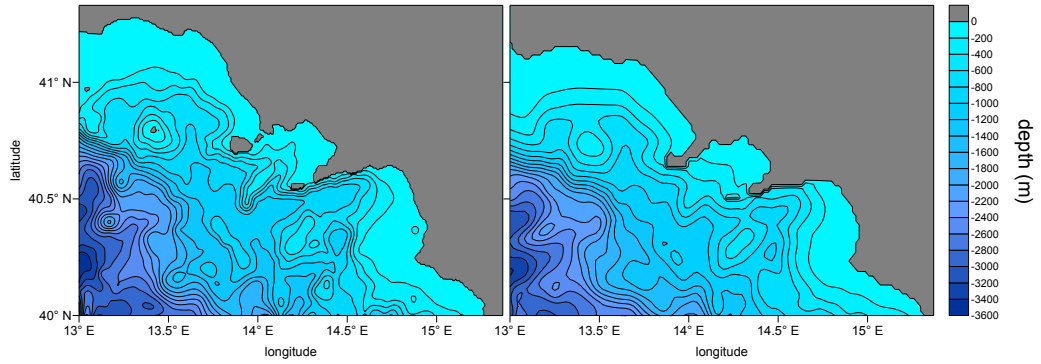

Figure 4.18: Bottom topography interpolated onto the 1/144°-resolution coastal model (left) and onto the 1/48°-resolution Tyrrhenian Sea model (right).

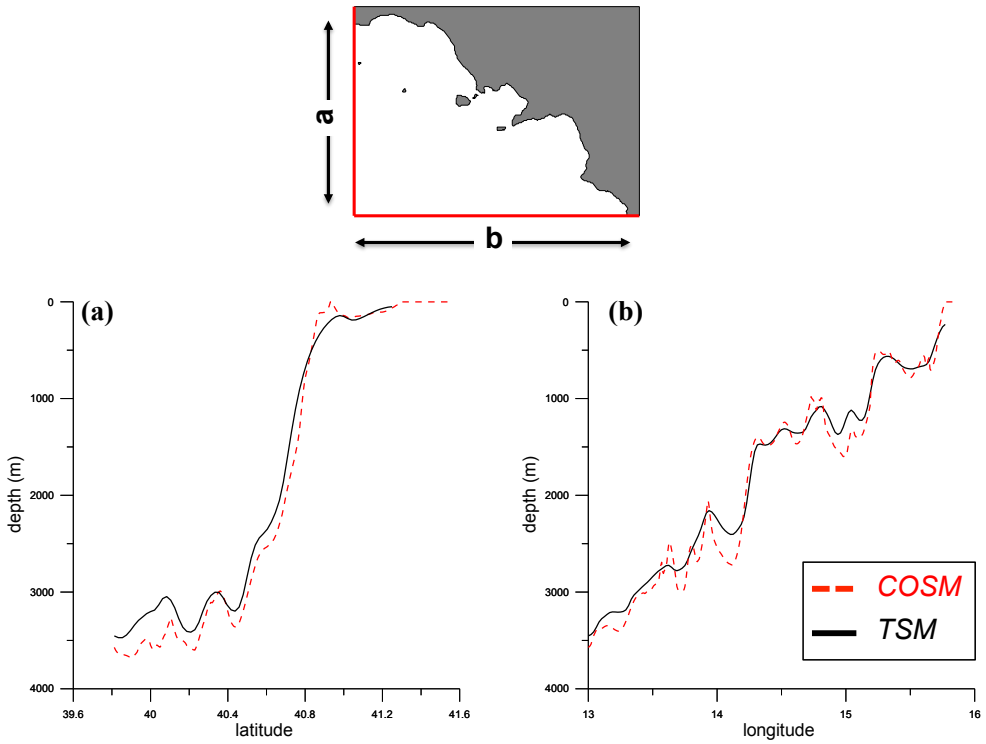

Figure 4.19: Comparison of the two bathymetries along the two open lateral western (a) and southern (b). boundaries. The black line denotes the TSM bathymetry while the red line denotes the bathymetry of the COSM.

porally averaged fields are then interpolated vertically from the 40 sigma-levels to 72 equally-spaced vertical levels. At each new level the fields are then interpolated bilinearly in the horizontal over the COSM grid. Finally, all the fields are interpolated vertically over the 40 sigma-levels of the coastal model. Although the models have the same vertical discretization, the intermediate vertical interpolation is needed because the 40 sigma-levels of the two models cannot be exactly coincident: the bottom topographies are, in fact, slightly different because of the different horizontal resolution (Fig. 4.19).

Time-dependent dynamical boundary conditions are then imposed along the lateral open boundaries of the coastal model: this is done with the velocity, salinity and temperature fields obtained from TSM integration. The open boundary condition for the barotropic velocity relies on a modified Flather (1976) formulation (see also Maraschiello et al., 2001) applied to the outflowing velocities (Zavatarelli and Pinardi, 2003). In Fig. 4.20 a schematics of the nesting procedure is reported.

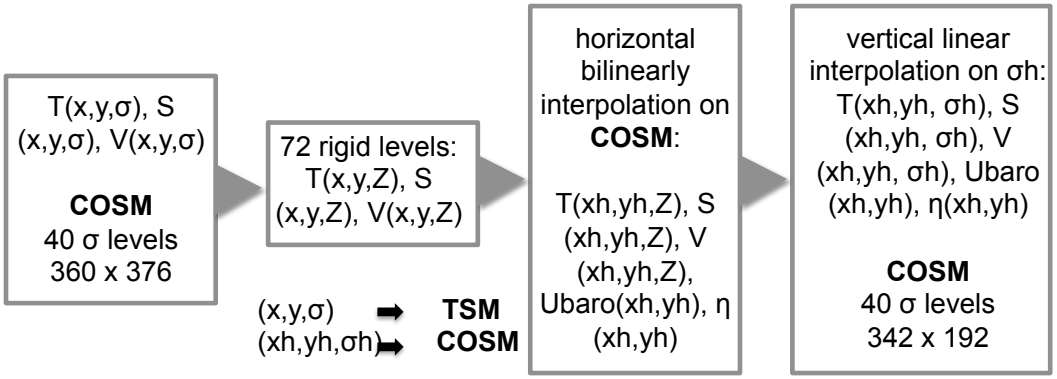

Figure 4.20: Schematics of the nesting procedure.

The relevance of the nesting is shown in Fig. 4.24. A snapshot (25 February 2009, 00:00 h) of the surface velocity map for the runs with and without

nesting are shown in the upper and lower panel, respectively. The presence of a strong large-scale north-westerly flow has clearly a profound effect on the surface circulation not only in the Tyrrhenian area, but also inside the three gulfs. This points to the fundamental role played by the nesting as far as the realistic circulation modeling in this coastal area is concerned. In conclusion, our implementation has provided a sophisticated and reliable modeling tool. In the next chapter several scenarios will be presented. Fig. 4.21 shows an example of TSM initial surface fields, while Fig. 4.22-4.23 show the lateral boundary conditions for the February 2009 run (explained in detail in section 5.1).

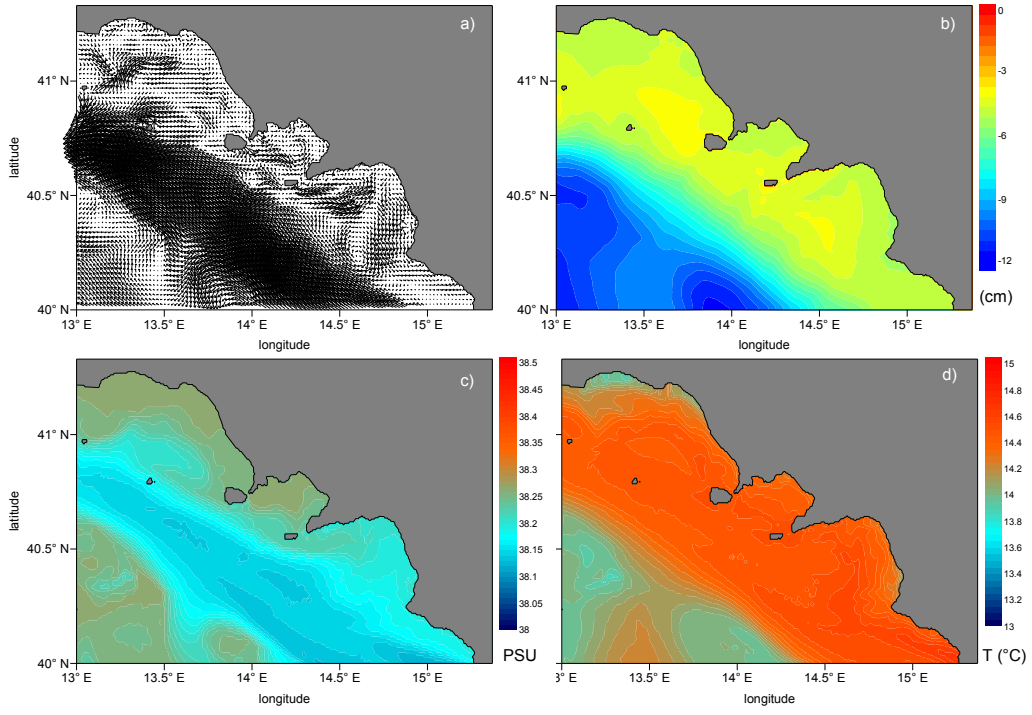

Figure 4.21: TSM initial fields of surface current (only the arrows at each every 3 grid points along both x and y are shown) (a), sea surface height (b), salinity (c) and temperature (d) on 14 February 2009 at 00:00 h.

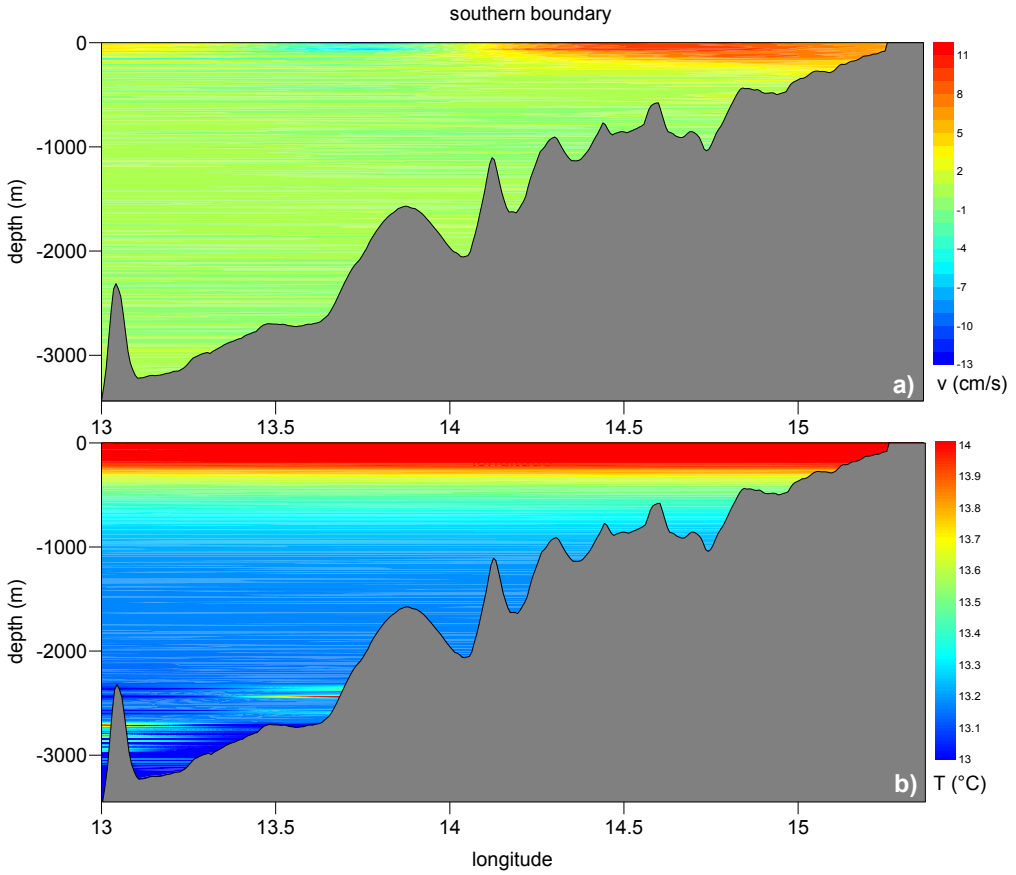

Figure 4.22: TSM lateral boundary conditions along the southern boundary for the meridional baroclinic velocity component (a) and for the temperature (b) on 14 February 2009 at 00:00 h.

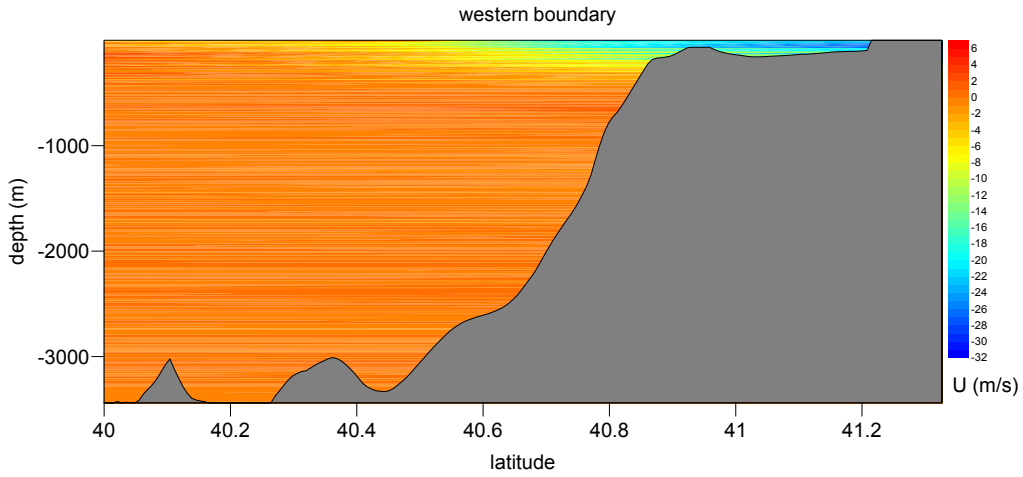

Figure 4.23: TSM lateral boundary conditions along the western boundary for zonal baroclinic velocity component on 14 February 2009 at 00:00 h.

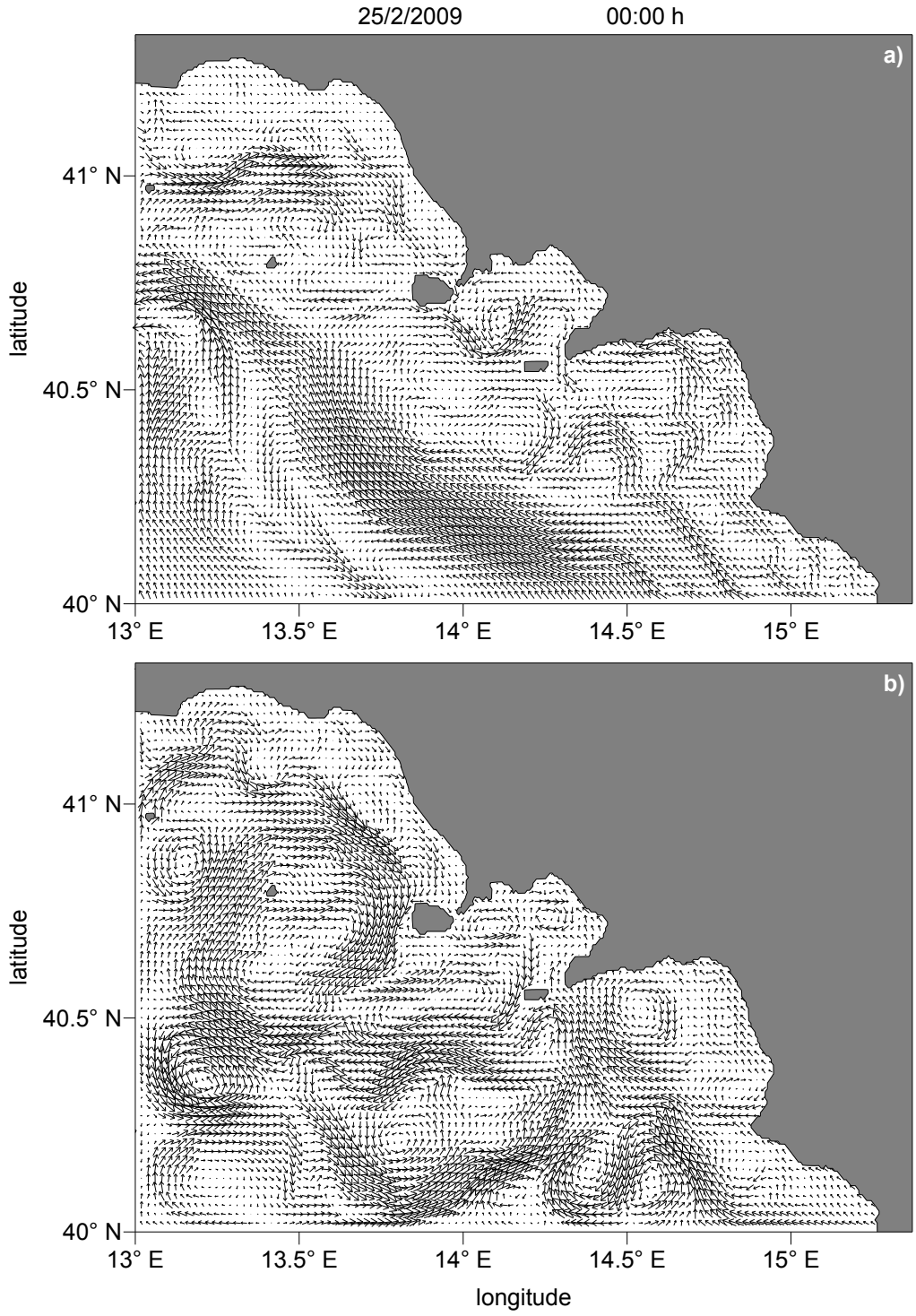

Figure 4.24: Surface current velocity maps (only the arrows at each every 3 grid points along both x and y are shown) on 25 February 2009 at 00.00h with the TSM nesting (a) and with closed boundary conditions (b).

Chapter 5

Simulation of different circulation scenarios

5.1 Introduction

In this Chapter three distinct simulations representative of winter (February 2009), autumn (November 2010) and summer (June 2003) seasons are presented. The first two simulations will be discussed in detail in sections 5.1 and 5.2, respectively. In section 5.3 the November 2010 simulation will be used to test the CSM SAR (see section 3.1) wind forcing capabilities. The June 2003 simulation will be introduced in section 5.4, but it will be discussed in detail in the next Chapter in connection with the experimental validation of the model with currentmeter measurements.

5.2 Simulation of February 2009

This is a 14-day run, spanning the period 11-25 February 2009. Fig. 5.1 shows four consecutive snapshots (6:00 h on 11, 16, 21, 24 February 2009)

of the surface current velocity maps with (left column) and without nesting (right column, obviously, in this case closed boundary conditions are imposed along the two open boundaries). Both the simulations with and without "open" boundary conditions take the same initialization from TSM, that is marked by the presence of a strong large-scale north-westerly flow (see upper panels of Fig. 5.1). The surface current evolution in the closed box simulation removes such flow (compare Fig. 5.1b-f, etc.), in so profoundly influencing the surface circulation over the whole domain. In fact also the circulation inside the Gulf of Naples and in the other gulfs presents notable differences without coastal-open sea interactions. The presence of a strong large-scale north-westerly flow in the open boundary simulation (and its absence in closed boundary simulations) is evident also in the sea surface elevation maps (Fig. 5.2): this points to the importance of the coastal-open sea coupling.

These differences are made even more evident in Fig. 5.3, where the time series of the two current velocity components and of the sea surface elevation are shown.

Now the complete nesting simulation is analyzed in detail. The time series of the total kinetic energy (Fig. 5.4) is also an interesting diagnostic tool which informs us about the short spin-up time (of few days). The vertical profiles of temperature and salinity taken in a central point of the Gulf of Naples (Fig. 5.5) show a stratification of the water column typical of the winter season.The vertical profiles of temperature and salinity taken in a central point of the Gulf of Naples (Fig. 5.5) show a stratification of the water column typical of the winter season.

It is interesting to compare the surface circulation simulated with COSM with that simulated by TSM. In Fig. 5.6 the surface current map on 24 Febru-

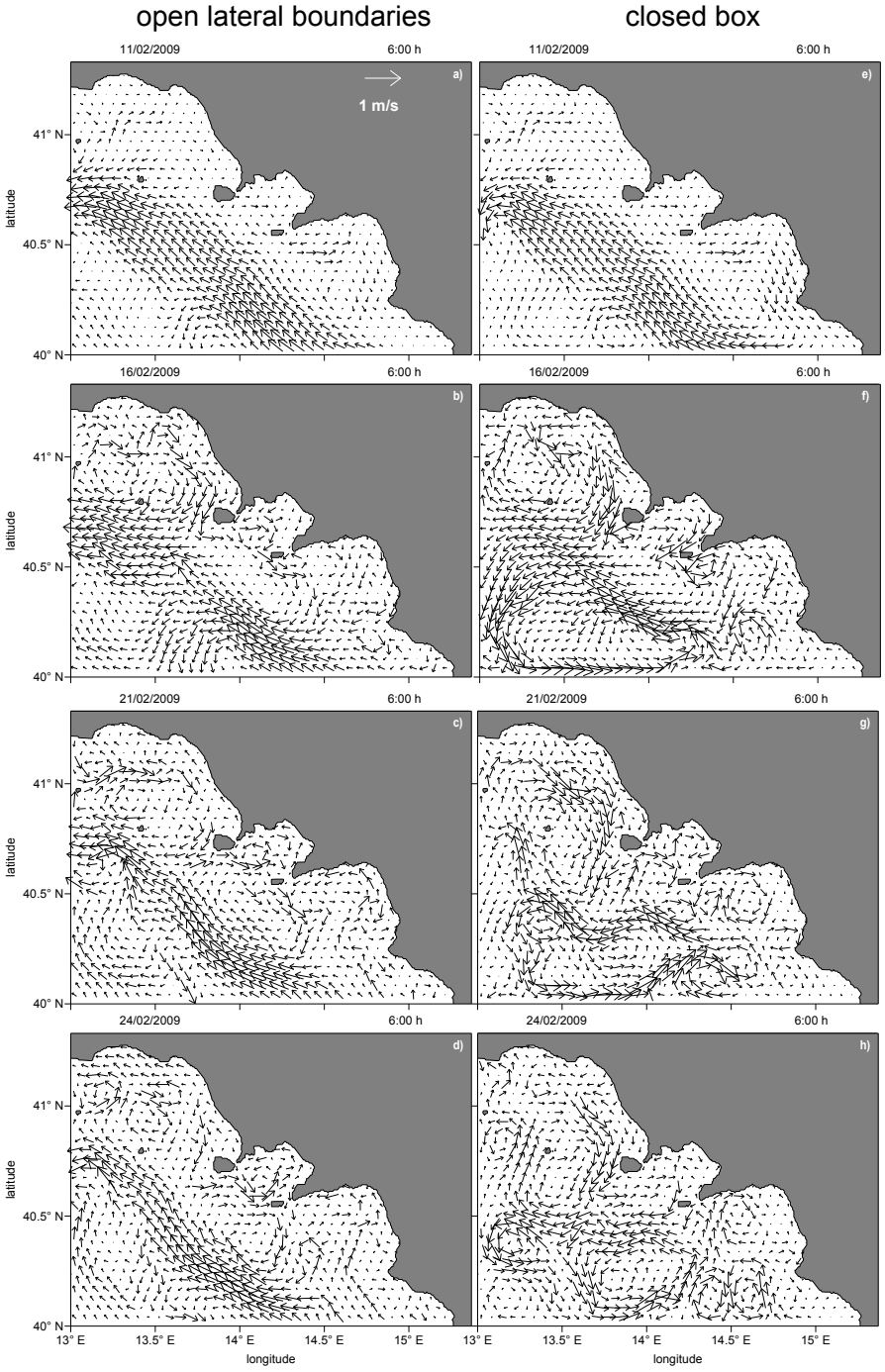

Figure 5.1: Surface current velocity maps (only the arrows at each every 9 grid points along both x and y are shown) at 6:00 h on 11, 16, 21, 24 February 2009 with (left column) and without nesting (right column).

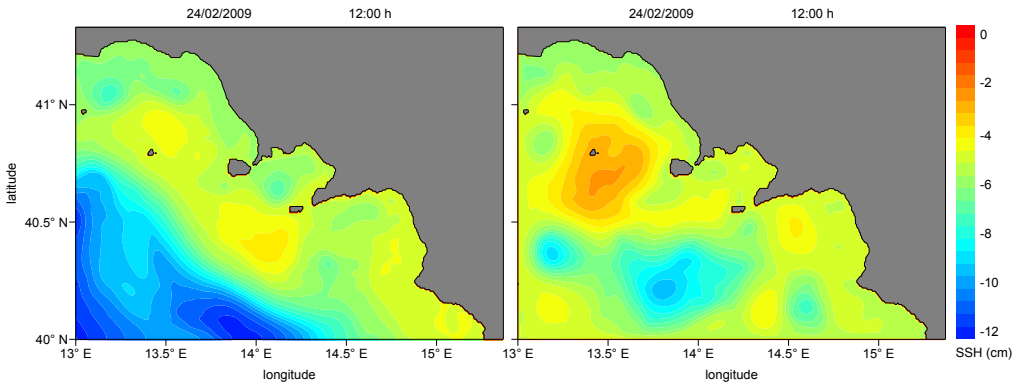

Figure 5.2: Sea surface elevation at 12:00 of 24 February 2009 with (left column) and without nesting (right column).

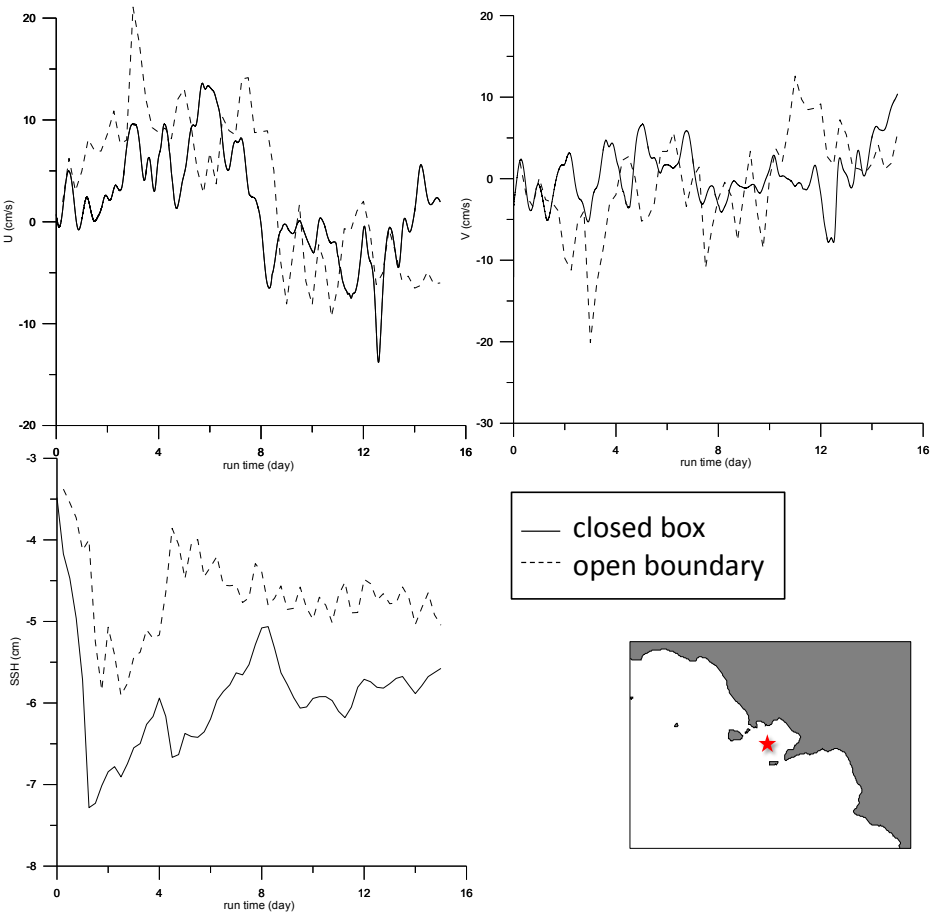

Figure 5.3: Zonal, meridional velocity components, and sea surface height time series on 11-25 February 2009 relative to the point indicated in the map (lower right panel) in the case with (dashed line) and without nesting (solid line).

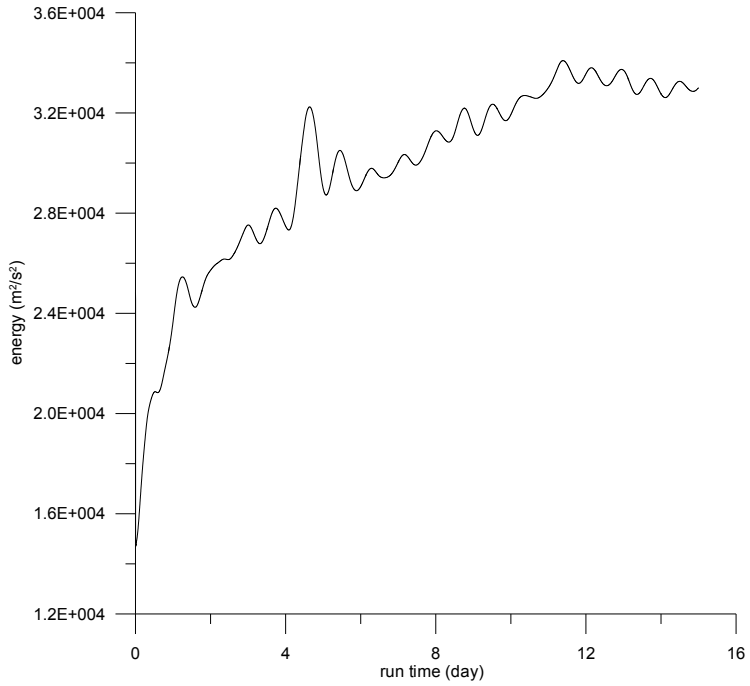

Figure 5.4: Time series of the total kinetic energy.

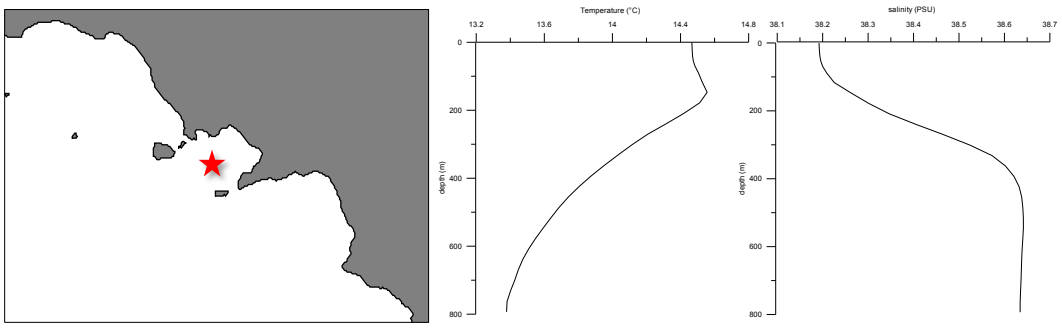

Figure 5.5: Temperature and salinity profiles at the point indicated with a star.

ary 2009 obtained with TSM is compared with altimeter data available for the same period (Napolitano et al., 2013). The altimeter data are from the

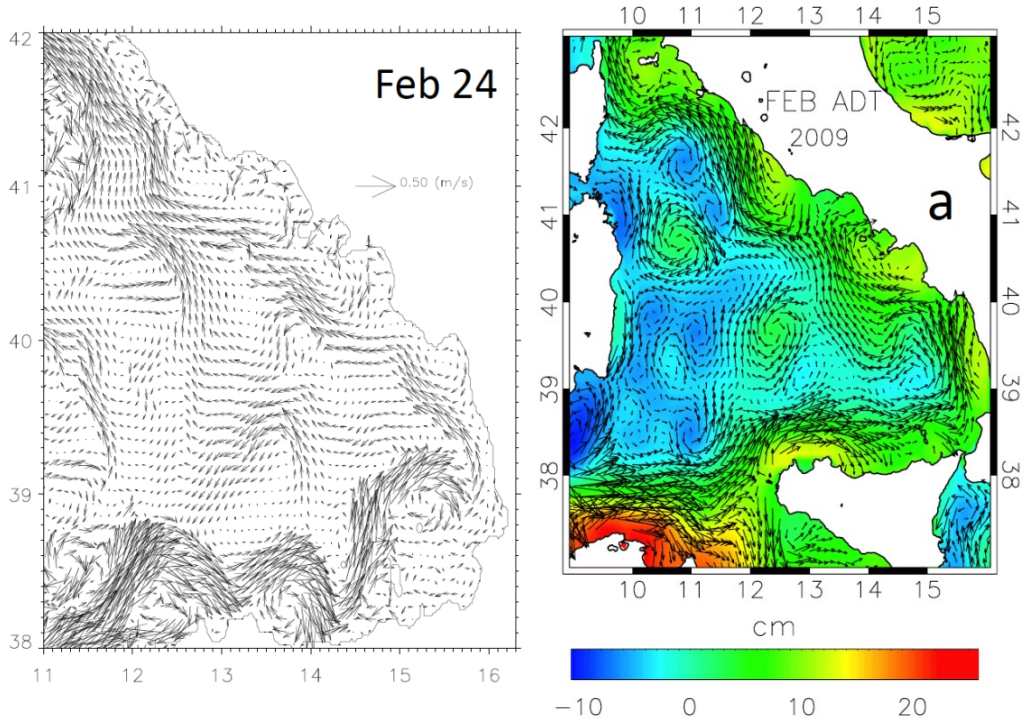

Figure 5.6: Current velocity maps by TSM on 24 February (left panel) and the weekly Updated Delayed maps of Absolute Dynamic Topography (ADT) for the same period (right panel). From Napolitano et al. (2013).

AVISO (`http://www.aviso.oceanobs.com/`) dataset that, as shown in Iacono et al. (2012), contains valuable information about the Tyrrhenian Sea surface circulation. Napolitano et al. (2013) show that the TSM surface circulation is in good agreement with the AVISO reconstruction in all seasons, as shown above for February 2009.

Comparison of the surface currents simulated on 24 February 2009 by COSM (Fig. 5.7) with those of Fig. 5.6 shows good agreement (as expected due to the adopted nesting). Moreover, the COSM dynamics yields small scale details absent in TSM. The anticyclonic gyre just off the Gulf of Naples (that seems to be a recurrent feature of the winter-spring circulation, as ob-

served by Napolitano et al., 2013) is simulated with more detail by COSM. In Fig. 5.7 it is possible to observe several small-scale dynamic structures, especially in the gulfs of Naples and Gaeta, while a strong large-scale north-westerly flow remains virtually unchanged.

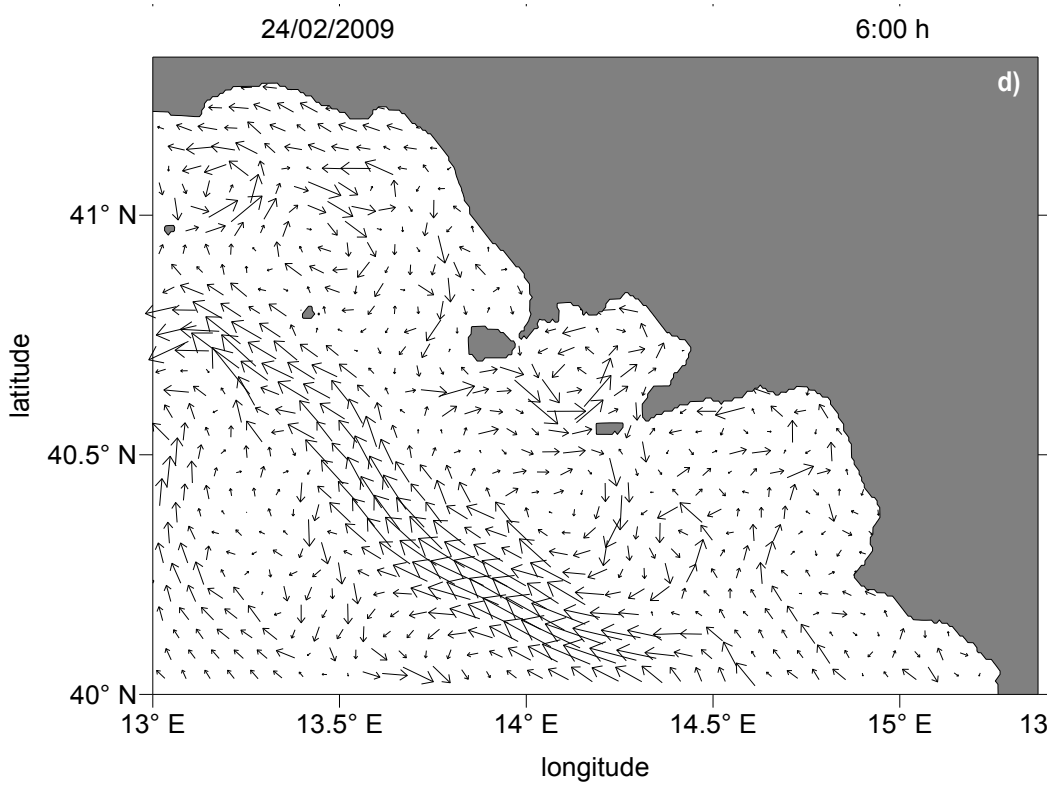

Figure 5.7: Surface current velocity maps from 24 February 2009 provided by COSM. Only the arrows at each every 9 grid points along both x and y are shown.

5.3 Simulation of November 2010

This is a 14-day run, spanning the period 10-25 November 2010. Fig. 5.8 shows the current velocity maps at the surface and at 300 m depth, and sea surface elevation at 00:00 of 25 November 2010 with (left column) and without nesting (right column). The substantial differences found between left and right maps shows once more how essential the nesting procedure is. In

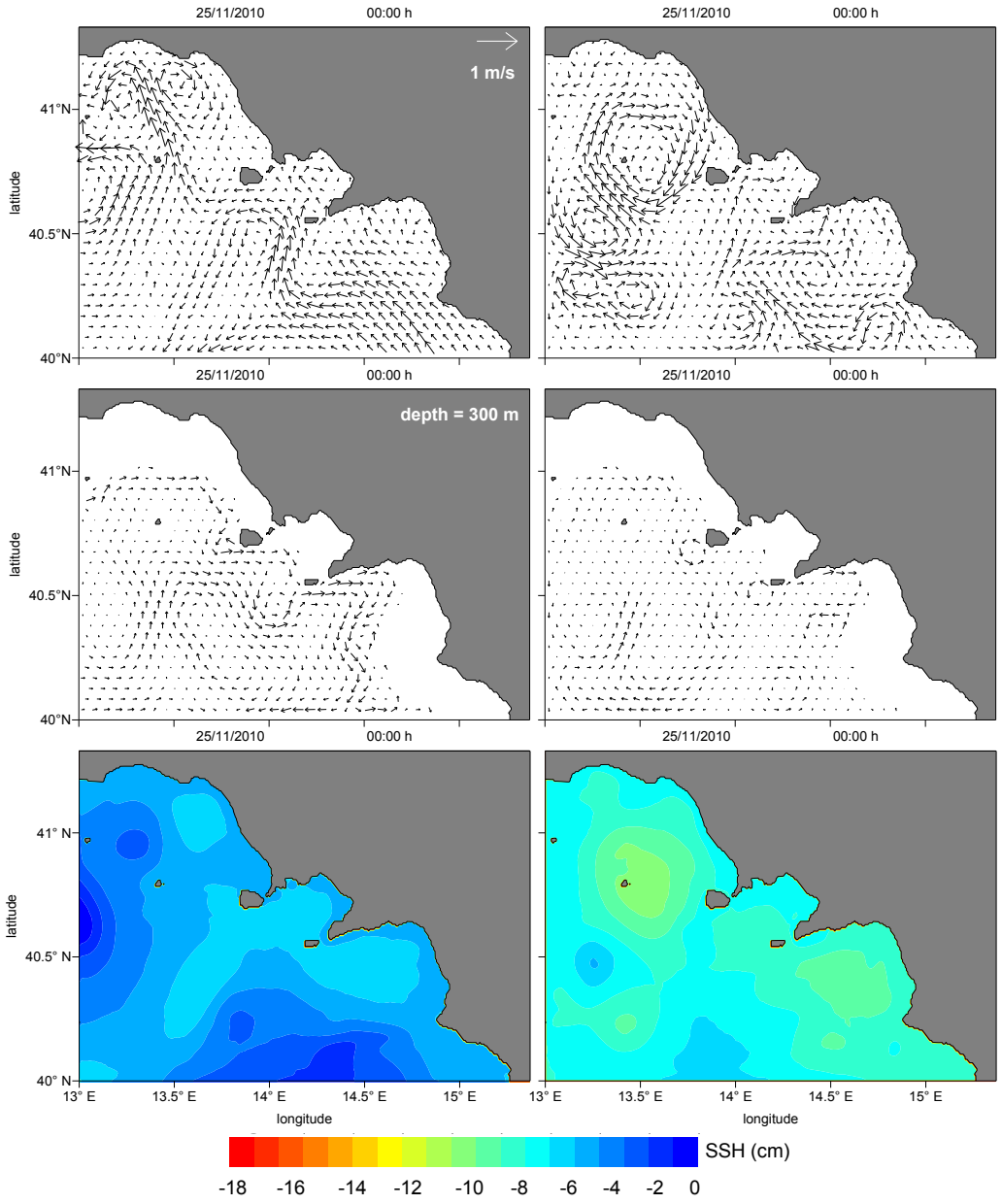

Figure 5.8: Current velocity maps (only the arrows at each every 9 grid points along both x and y are shown) at the surface and at 300 m depth, and sea surface elevation at 00:00 of 25 November 2010 with (left column) and without nesting (right column).

particular, the large surface anticyclonic gyre in the Gulf of Gaeta, present only in the simulation with closed boundary conditions, is clearly spurious, and is due to the unrealistic closed lateral barriers that force the flow to re-circulate. In Fig. 5.9 the time series of the two current velocity components and of the sea surface elevation are shown. Now the complete nesting simu-

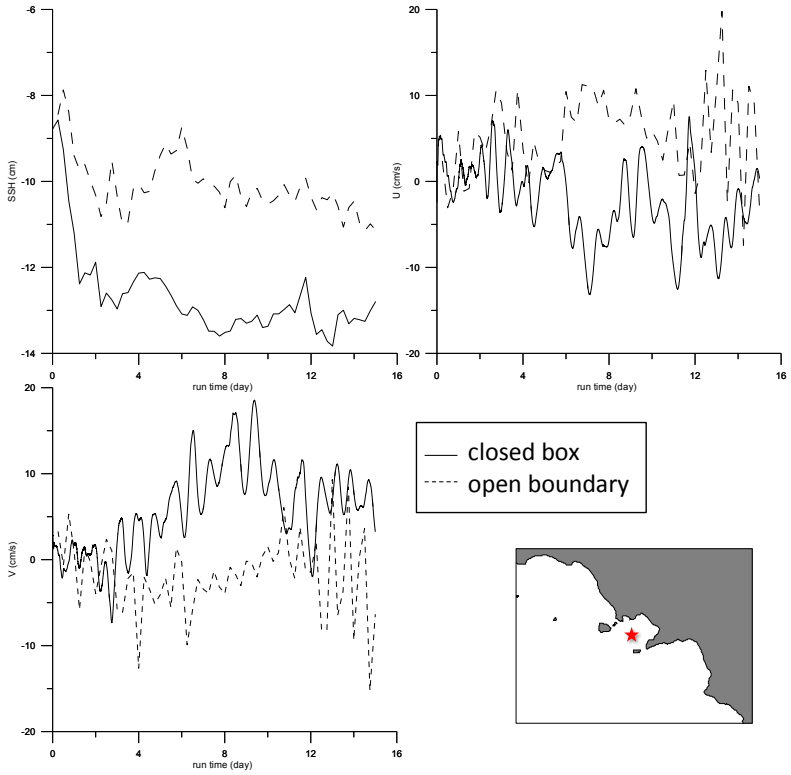

Figure 5.9: Zonal, meridional velocity components, and sea surface height time series on 10-25 November 2010 relative to the point indicated in the map (lower right panel) in the case with (dashed line) and without nesting (solid line).

lation is analyzed in detail. In Fig. 5.10 the time series of total kinetic energy is reported. The vertical profiles of temperature and salinity taken in a central point of the Gulf of Naples (Fig. 5.11) show a stratification of the water column typical of the month of November (see also Fig. 5.12), where the stratification deriving from the COSM simulation is in excellent agreement with measurements performed in the Gulf of Naples on 17 November 2003.

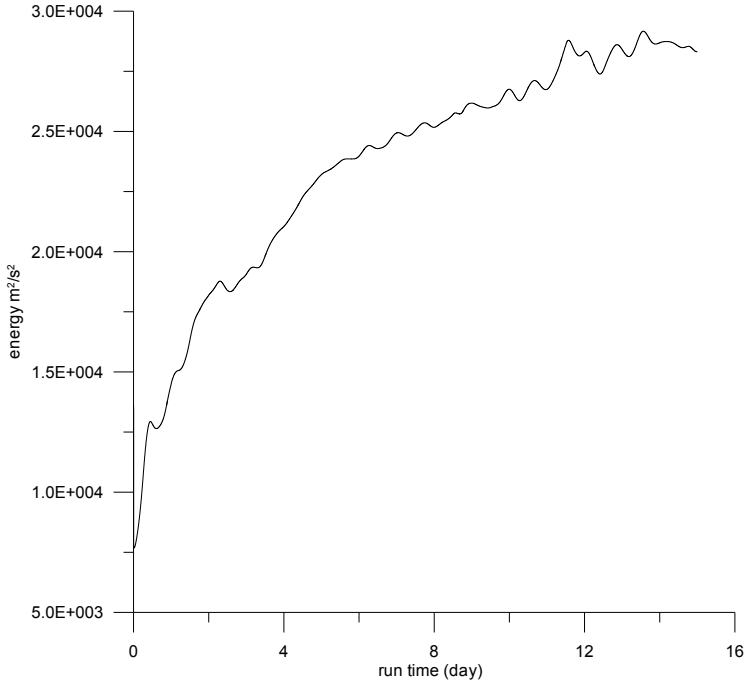

Figure 5.10: Time series of the total kinetic energy.

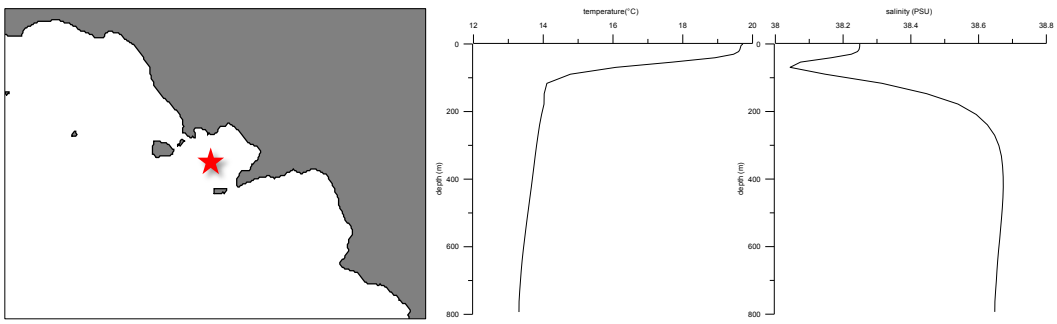

Figure 5.11: Temperature and salinity profiles at the point indicated with a star.

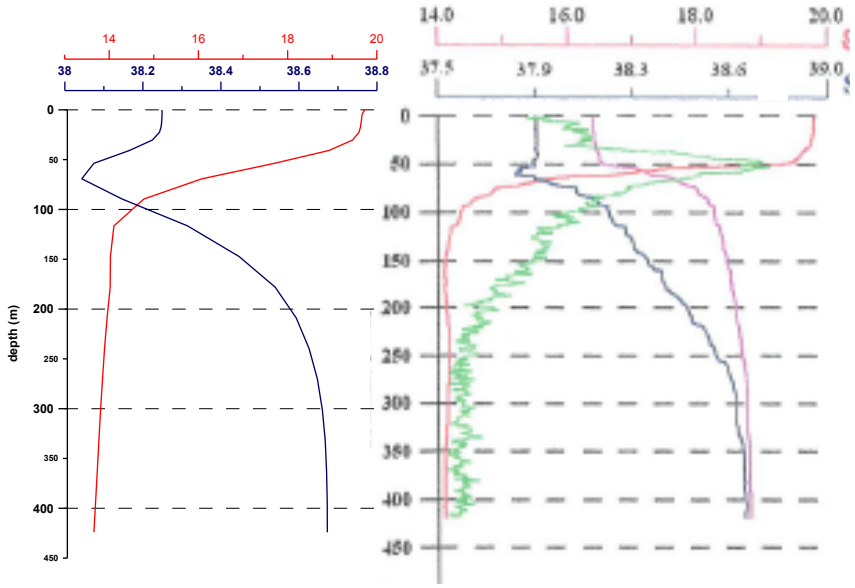

Figure 5.12: Temperature and salinity vertical profiles provided by COSM (left panel) and actually measured in the Gulf of Naples on 17 November 2003 (the right panel was taken from Roselli, 2003).

Finally Fig. 5.13 shows the surface current evolution, from 22 November to 24 November 2010, for the nested simulation; in this figure it is possible to observe several gyre structures in the gulfs of Naples, Gaeta and Salerno, and a weak large-scale north-westerly meandering flow in the northern part of the domain. In the November simulation the strong large-scale north-westerly flow, that is evident in the February simulation (see section 5.1 in Fig. 5.7), is not yet formed.

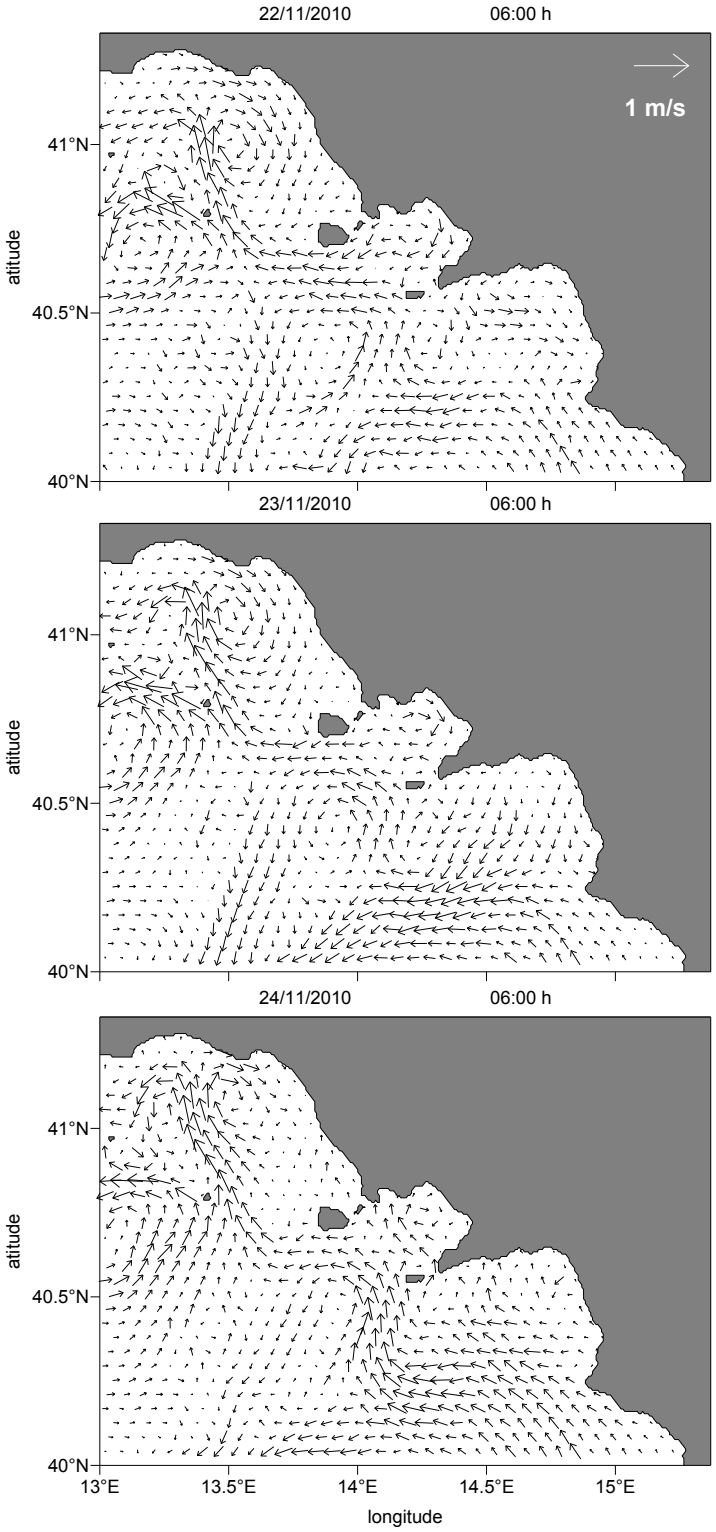

Figure 5.13: Daily snapshots of surface current velocity maps from 22 November 2010 at 06:00 h to 24 February at 06:00. Only the arrows at each every 9 grid points along both x and y are shown.

5.4 Simulation of November 2010: analysis of COSMO-SkyMed SAR wind forcing capabilities

In this section the same simulation presented in section 5.3 relative to November 2010 (for which the ECMWF forcing was imposed) will be compared to the analogous simulation forced by a blended wind forcing that includes both ECMWF and CSM SAR data (the latter were discussed in detail in section 3.3) with the aim of assessing the capability of CSM SAR wind data to improve coastal circulation modeling. These results, like the ones presented in sections 3.2 and 3.3, have been obtained within the framework of a COSMO-SkyMed©Italian Space Agency (ASI) project, and the resulting publication of Montuori et al. (2013) is integral part of this PhD research activity.

As already said in the preceding section, the simulation lasts 15 days, from 10 November 2010, 00:00 h to 25 November 2010, 00:00 h. The SAR-wind data of 20 November 2010 at 05:00 h and 21 November 2010 at 05:00 h with 12.5 km resolution have been used to construct, together with ECMWF data, the blended wind forcing. Fig. 3.3 shows the CSM SAR-derived surface wind velocity map (green arrows), along with the corresponding ECMWF (red arrows) and ASCAT (blue arrows) maps for the first of these two fields (20 November 2010, 05:00 h). The SAR-wind field of day 20 November 2010 at 05:00 h has been spatially interpolated with three ECMWF fields of day 20, at 00:00, 06:00, and 12:00 UTC (see the first set of three dots in the upper panel of Fig. 5.14). The same has been done for the second SAR-wind field (see the second set of three dots). This choice is justified

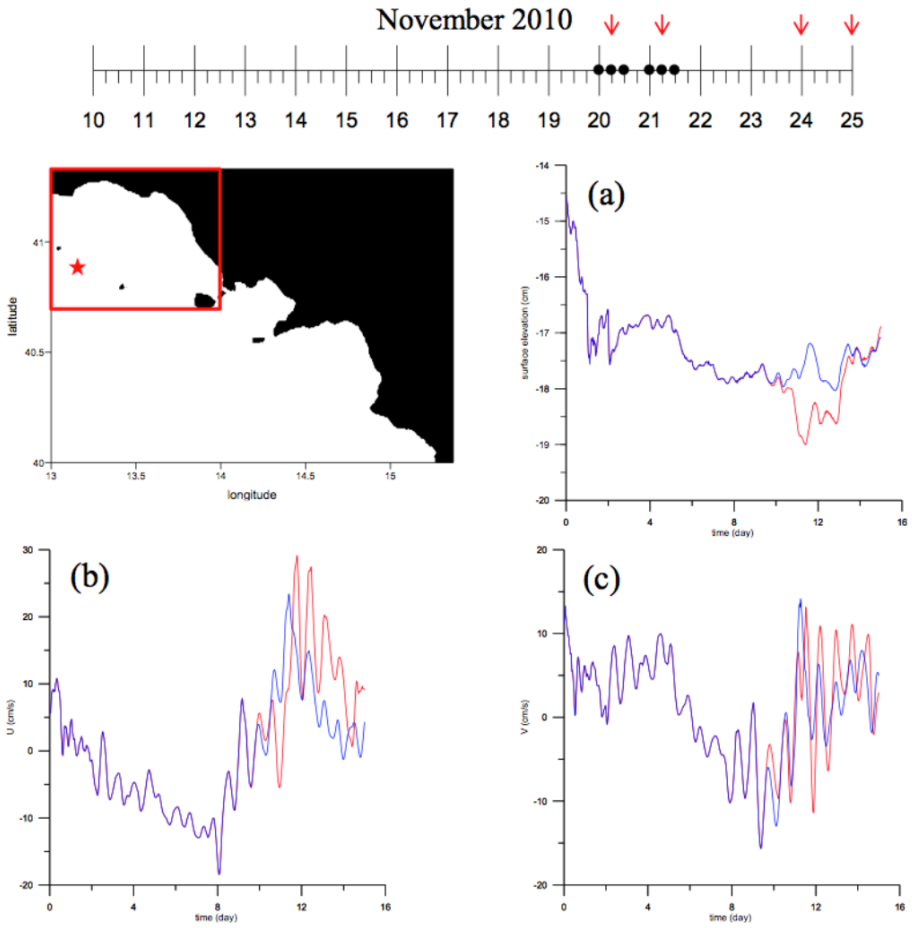

Figure 5.14: Upper panel: representation of the 15-day November 2010 blended wind product (the ticks represent ECMWF winds; the dots show the instants at which COSMO-SkyMed wind data have been blended with ECMWF data; the red arrows show the time instants corresponding to the maps shown in the subsequent figures). The red rectangle inside the map represents the window in which the comparisons shown in the subsequent figures are performed. The graphs of panels (a), (b), and (c) show the time series of the sea surface elevation, of the zonal and meridional surface velocity components, respectively, sampled in the point identified by a star in the map; the blue lines refer to the simulation with the purely ECMWF forcing, the red lines to the simulation with the blended wind forcing (t = 0 corresponds to 10 November 2010, 00:00 h; from Montuori et al., 2013).

by the paucity of SAR data: in doing so we have increased the weight of each available SAR-wind field without introducing an excessive spurious reduction of the temporal variability (the SAR-wind information has only been extended 6 h before and after the measured data). Since the SAR data are limited to a north-western part of the integration domain (Fig. 3.3), the results of the simulations are analyzed in the rectangle and in the point identified in the map of Fig. 5.14, where the improvement of the model results is expected to be more substantial. The three graphs of Fig. 5.14 show the time series of the sea surface elevation and of the two components of the surface current velocity: the signal affected by the SAR-wind forcing starts separating from that obtained with the ECMWF wind (blue line) immediately after the first SAR-wind data insertion, and the difference has remained remarkable ever since, even well after the time of the last SAR-wind data insertion. This is clearly due to the different time-dependent adjustments produced by the two forcings that have a typical time scale of few days.

In Figs. 5.15 and 5.16, the surface currents and sea surface elevation obtained with the purely ECMWF forcing (upper panels) are compared with those obtained with the blended forcing (lower panels) at the times indicated by the red arrows of the upper panel of Fig. 5.14. The differences are sometimes quite substantial and are not limited to the region of SAR-wind data coverage. For instance, on day 20 the strong southward current along the coasts of Latium produced by the ECMWF forcing is drastically reduced with SAR-wind data. On day 21 the strong cyclonic gyre east of the northward jet almost disappears with SAR-wind data. A similar phenomenon occurs on day 24. On day 25 the circulation in the western half of the window changes completely with SAR data. In conclusion, our results suggest that the surface wind fields obtained from CSM SAR data could be used,

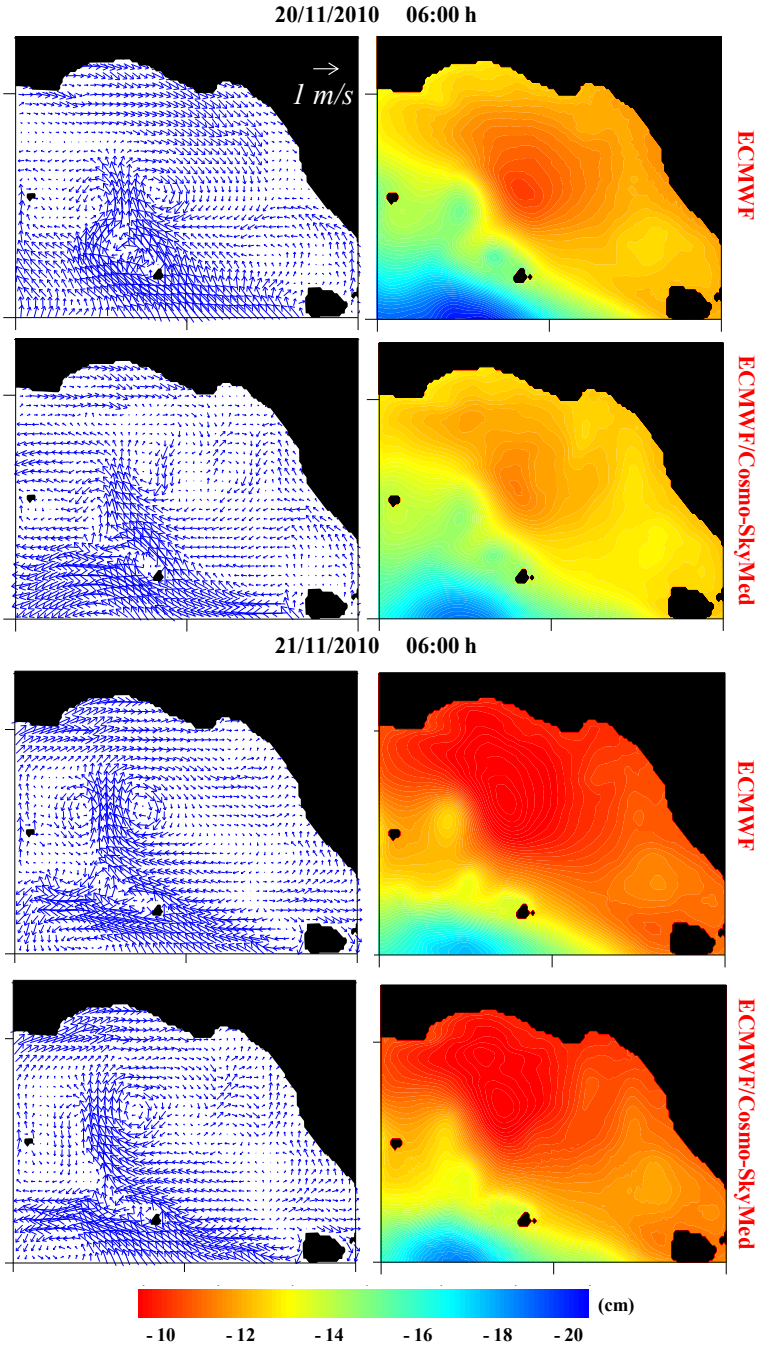

Figure 5.15: First and third row: surface currents (left) and sea surface elevation (right) in the window shown in Figure 5.14, respectively, at 06:00 h of 20 November 2010 and at 06:00 h of 21 November 2010 obtained in the simulation with ECMWF wind forcing. Second and fourth row: same, but obtained with blended ECMWF/COSMO-SkyMed wind forcing (from Montuori et al., 2013).

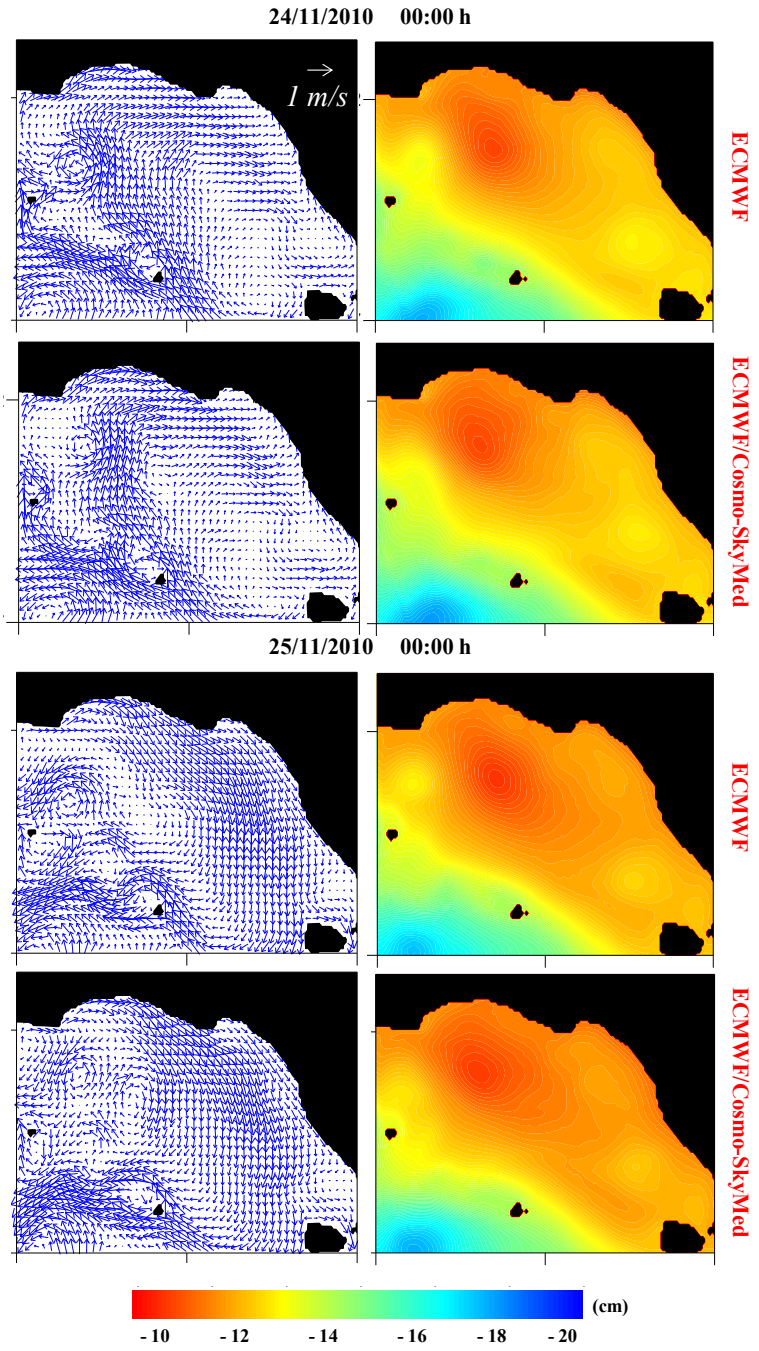

Figure 5.16: First and third row: surface currents (left) and sea surface elevation (right) in the window shown in 5.14, respectively, at 00:00 h of 24 November 2010 and at 00:00 h of 25 November 2010 obtained in the simulation with ECMWF wind forcing. Second and fourth row: same, but obtained with blended ECMWF/COSMO-SkyMed wind forcing (from Montuori et al., 2013).

together with model data (such as ECMWF), to construct a blended wind product that can serve as an alternative wind forcing for improved coastal marine circulation modeling. In fact, the SAR-based wind product is measured instead of modeled, so it bypasses all the model limitations associated with coastal environments with strong orographic features; moreover, those winds have a spatial resolution that can be considerably higher than that of modeled winds, so that more reliable simulations of mesoscale and smaller scale oceanic features can be achieved.

In conclusion, a feasibility study aimed at evaluating the capability of CSM SAR data to provide surface wind fields that can improve coastal circulation modeling was carried out. A SAR data set 60 X-band Level 1B DGM ScanSAR Huge Region mode VV-polarized CSM SAR data, gathered in a southern Tyrrhenian coastal area on 2010, is properly processed for wind vector field estimation purposes. Within such a framework: (1) the SAR wind speed estimation is accomplished by means of a SAR wind speed retrieval algorithm based on the azimuth cut-off procedure; (2) the SAR wind direction estimation is accomplished by means of SAR wind direction retrieval algorithm based on the DWT-MRA. The oceanographic model, which is used to simulate coastal circulation processes in a southern Tyrrhenian coastal test area, is forced by a blended wind product that includes ECMWF and SAR-derived winds. Our results have shown the following:

- X-band CSM SAR data effectively represent a successful resource to retrieve the wind field information at the sea surface.

- a blended wind product based on X-band CSM SAR-retrieved surface wind data, and on other wind products (such as ECMWF model winds), can improve the simulation of wind-driven coastal circulation

processes (e.g., de Ruggiero, 2013);

- despite both the limitations of available consecutive CSM SAR acquisitions (and therefore SAR-derived wind field data) and the relatively poor spatial coverage of the adopted coastal test site, our results show that CSM SAR data do represent a potentially valuable tool for improving coastal circulation modeling, which is very important for oceanographic, ecological, social and economic applications.

- In section 6.1 a validation of the present simulation with CODAR data will be presented.

5.5 Simulation of June 2003

The simulation of June 2003 is typical of a late spring-summer condition, in which a shallow seasonal thermocline is present (see Fig. 6.10). The detailed discussion of this interesting case is postponed to the next Chapter devoted to the experimental validation of COSM implementation. This is because during that month a very energetic current oscillation was measured in the Bocca Piccola, and is captured by the model response; so we will use this case study as a valuable means of validating experimentally our model implementation.

Chapter 6

Experimental validation

6.1 Experimental validation with currentmeter measurements: a Kelvin wave episode

The process-oriented model study of Pierini et al. (2005) (performed with the same three-layer model of Pierini et al., 2004, mentioned in section 1.4) evidenced the excitation of an energetic internal Kelvin wave propagating along the Campania coasts. Such coastal wave derived by the relaxation of an upwelling generated by a strong wind event during June 2003. That modeling result was then successfully validated with current data obtained by a currentmeter moored in the Bocca Piccola of Capri (Fig. 6.1) in the framework of a research project on the Marine Protected Area of "Punta Campanella".

We have therefore reproduced the same simulation with COSM, and the obtained results provide a first valuable experimental validation of this modeling tool.

The mooring instrumentation (Fig. 6.2) consisted of two *Aanderaa* currentmeters *S/N 4747* and *S/N 5798*, four *Sea-Bird Electronics 39 3930492* tem-

Figure 6.1: Left panel: mooring position in the coastal domain (point b). Right panel: a picture of "Punta Campanella" (the red mooring float is visible on the left).

perature sensors, one sediment trap, three *Resinex* floats, one Mors releaser and one ballast positioned as shown in Fig. 6.2; the mooring location was 40° 34' N and 14° 18' E. The two currentmeters, located at 25 m and 65 m depth, provided measurements of direction and speed of the current velocity during the period 9 June - 10 November 2003 with a sampling interval of 30 minutes.

	ANCHORAGE	RECOVERY
DATE	9/06/2003	10/11/2003
TIME (h)	12.05	12.35
LATITUDE	40° 34' N	40° 34' N
LONGITUDE	14° 18' E	14° 18' E
ECHO DEPTH (m)	79.84	80.03

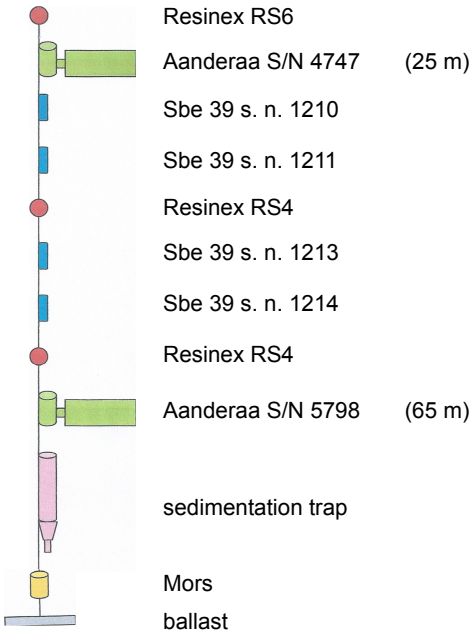

Figure 6.2: Table: mooring location and temporal deployment. Right: schematics of the mooring instrumentation (from Roselli, 2003).

Fig. 6.3 shows the time series of the current velocity measured at 25 m depth projected onto the along-channel direction (given by the red arrow in the Bocca Piccola). The time series shows a strong southward current during days 20 - 22 June followed by a rapid reversal that lasted two more days. This was explained by Pierini et al. (2005) as the result of the passage of a Kelvin wave through the strait.

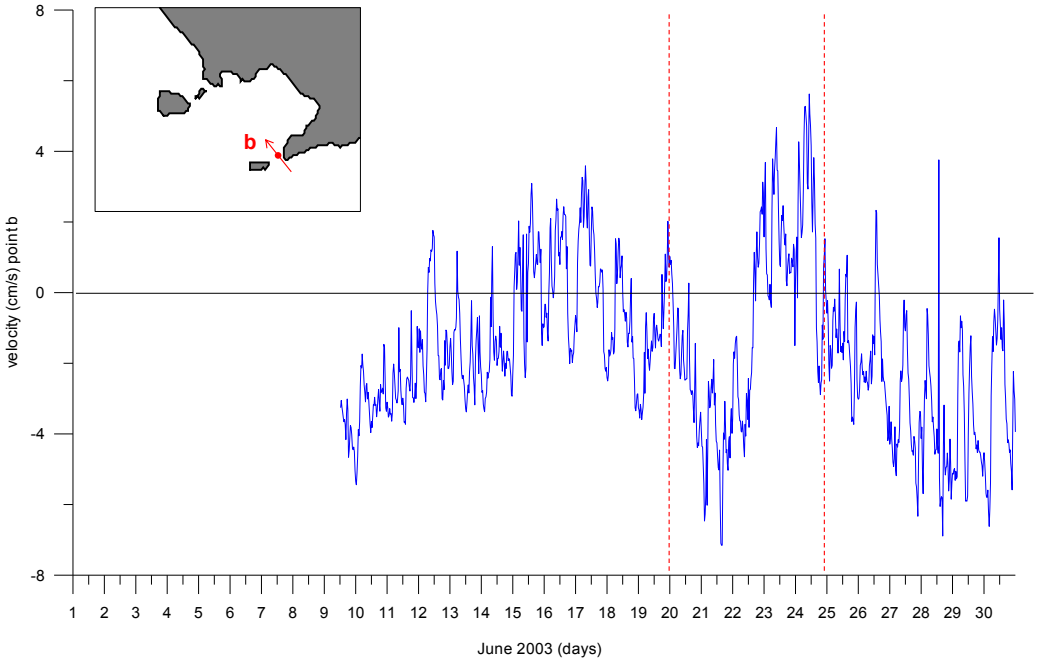

Figure 6.3: Time series of the current velocity measured at 25 m depth projected onto the along-channel direction (shown by the red arrow in the map).

The ECMWF wind stress amplitude interpolated in the mooring position yields (Fig. 6.4) strong north-easterly winds flowing from t $\sim$ 19 June to t $\sim$ 21 June, while weak winds are present both before and after that strong wind event. Fig. 6.5 shows the evolution of the surface wind velocity from 18 to 21 June 2003. Pierini et al. (2005) showed that the northerly winds blowing during 19-20 June produced a notable upwelling along the coasts of Campania, which then relaxed when the winds weakened, so that

the Kelvin wave thus generated could be clearly detected from the weak residual currents by monitoring its propagation along the coasts (this also explains the phase shift between the wind burst and the beginning of the large amplitude oscillation shown in Fig. 6.3 within the red vertical lines).

This phenomenon was modeled with the COSM through distinct simulations of increasing degree of realism summarized in Table 6.1. In all numerical experiments the model was run with closed boundary conditions.

exp.	**mode**	**initialization**	$\mathbf{A_H}$	**wind forcing**
1	barotropic	constant density T=20°C S = 36.00 PSU	100 m^2/s	June 2003
2	baroclinic	constant density T=20°C S = 36.00 PSU	100 m^2/s	June 2003
3	baroclinic	constant density T=20°C S = 36.00 PSU	Smagorinsky formula	June 2003
4	baroclinic	TSM June stratification	Smagorinsky formula	June 2003
5	baroclinic	TSM February stratification	Smagorinsky formula	June 2003
6	baroclinic	TSM June stratification	Smagorinsky formula	May- June 2003

Table 6.1: Table of June 2003 simulation.

We start from the idealized condition given by a barotropic flow. Exp. 1 is a barotropic simulation (with a homogeneous density corresponding to T=20° C and S=37.00 PSU) with a Laplacian horizontal eddy viscosity with A_H=100 m^2/s. Fig. 6.6 shows the time series (taken in the mooring location of the barotropic velocity. The first thing to note is that the amplitude (that

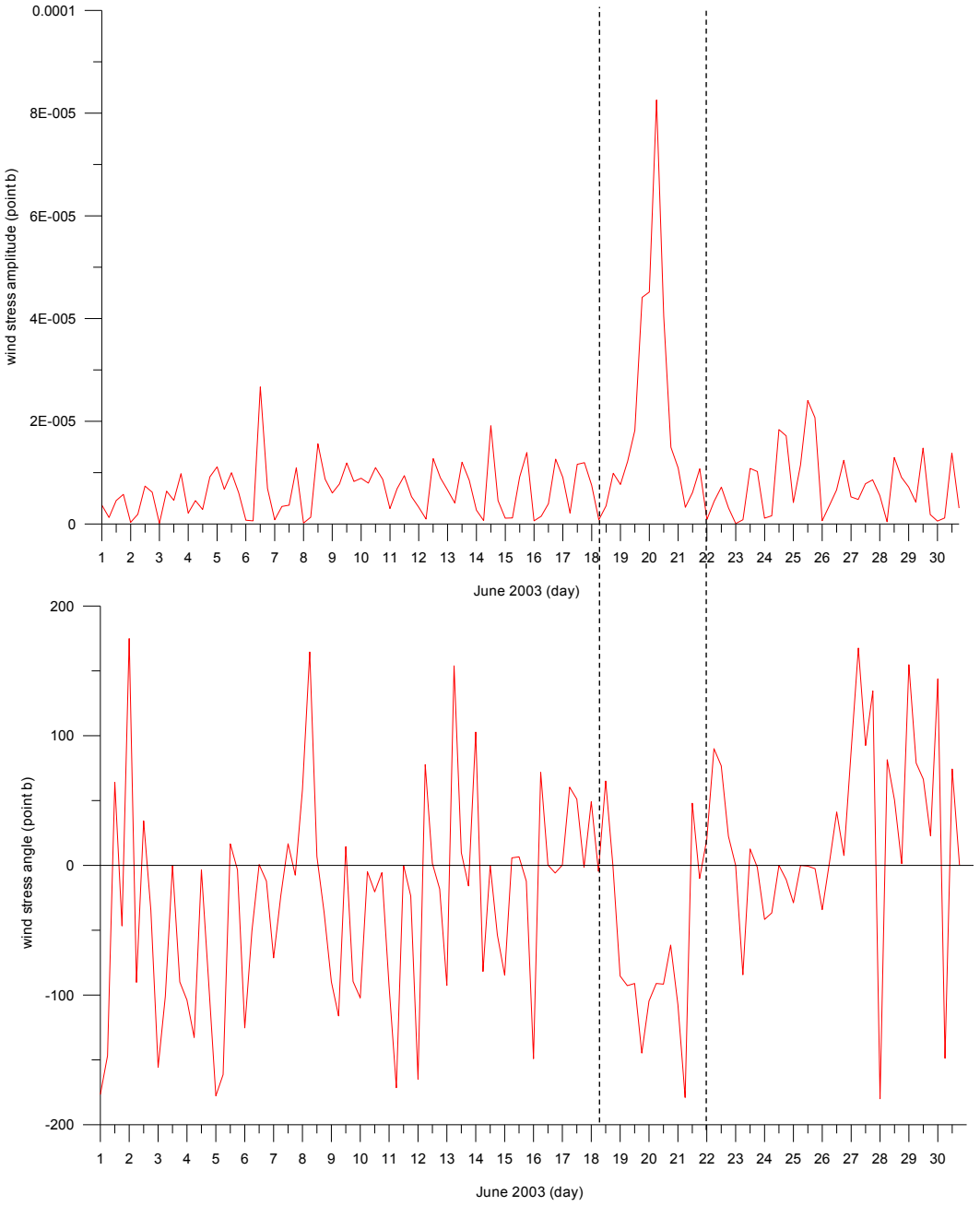

Figure 6.4: Time series of ECMWF wind stress amplitude (upper panel) and angle (lower panel) as interpolated in the mooring position for June 2003.

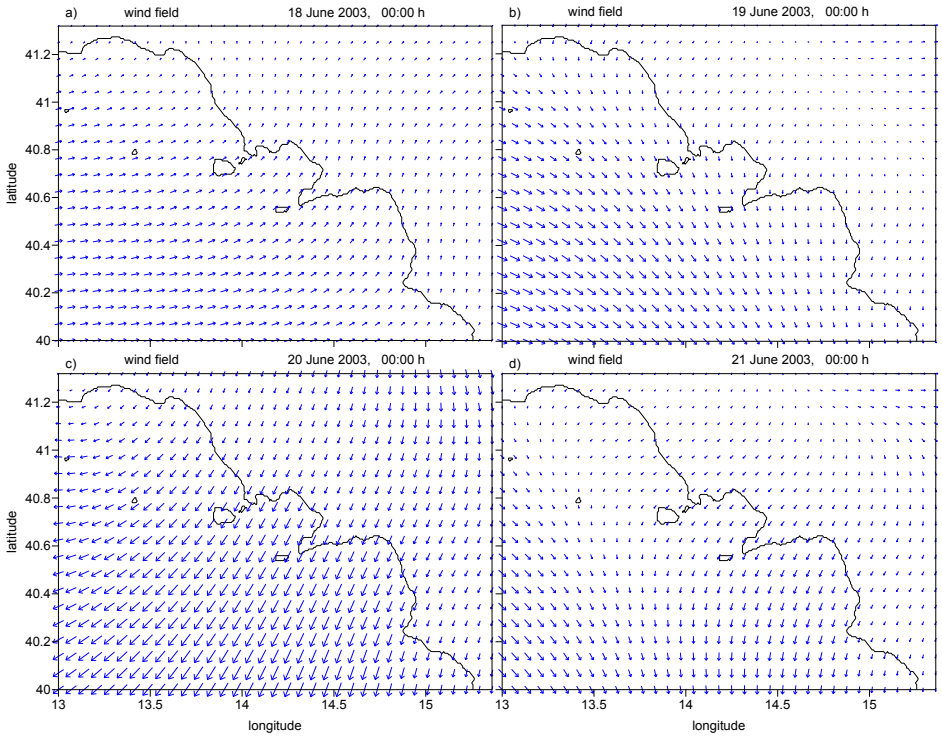

Figure 6.5: ECMWF wind velocity on 18 June (a), 19 June (b), 20 June (c), and 21 June (d) 2003 at 00:00h.

varied within a range of ~ 10 cm/s, see Fig. 6.3) is now less than one order of magnitude smaller than the measured one. This is clearly due to the excitation of an external Kelvin wave, whose surface signature is obviously much smaller than that associated with an internal Kelvin wave. Also the smaller time scale of the oscillation (compare with Fig. 6.3) is to be accounted for the higher phase speed of external Kelvin waves.

Exp. 2 (Fig. 6.7) is the same as Exp. 1, except that now the run is performed with an active baroclinic mode with constant density. Despite the identical physical problems described by the two simulations, the numerical solutions yield small differences: this is because the geostrophic currents in this second case are depth-independent, as in the barotropic case, but depth-dependent ageostrophic effects (related to the parameterization of the top and bottom boundary layers) are now present, while they are

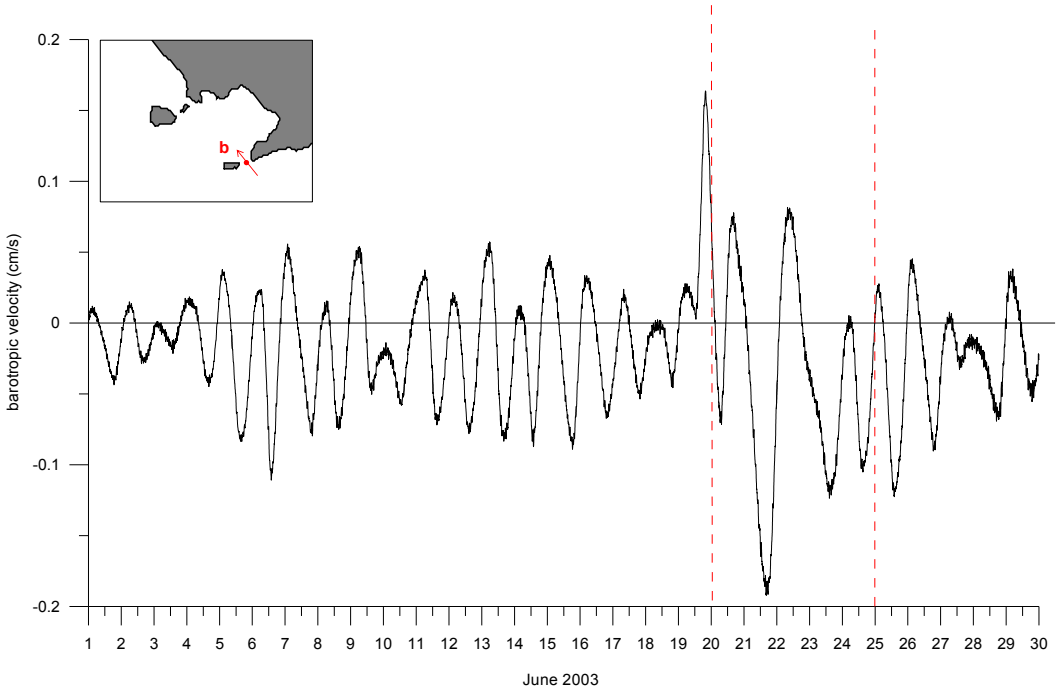

Figure 6.6: Time series of the projected barotropic velocity taken in the mooring location at z = -25 m for Exp. 1.

absent when only the barotropic mode is integrated (this causes the small differences found when comparing Fig. 6.7 with 6.6).

Exp. 3 (Fig. 6.8) is the same as Exp. 2, except that now the Smagorinsky formula is used (see equation 2.12; the horizontal momentum small-scale mixing processes are parameterized as horizontal diffusion along sigma surfaces depending on the horizontal velocity shear, and on the grid spacing via the Smagorinsky, 1963 diffusion scheme). The time series of Exp. 3 is similar to that of Exp. 2, but the amplitude is now larger by almost an order of magnitude. This is to be accounted mainly for the different parameterization adopted for the horizontal eddy viscosity, that allows for larger current fluctuations.

Exp. 4 is the realistic simulation in which the baroclinic model is initialized with the June 2003 TSM stratification and forced with the June 2003

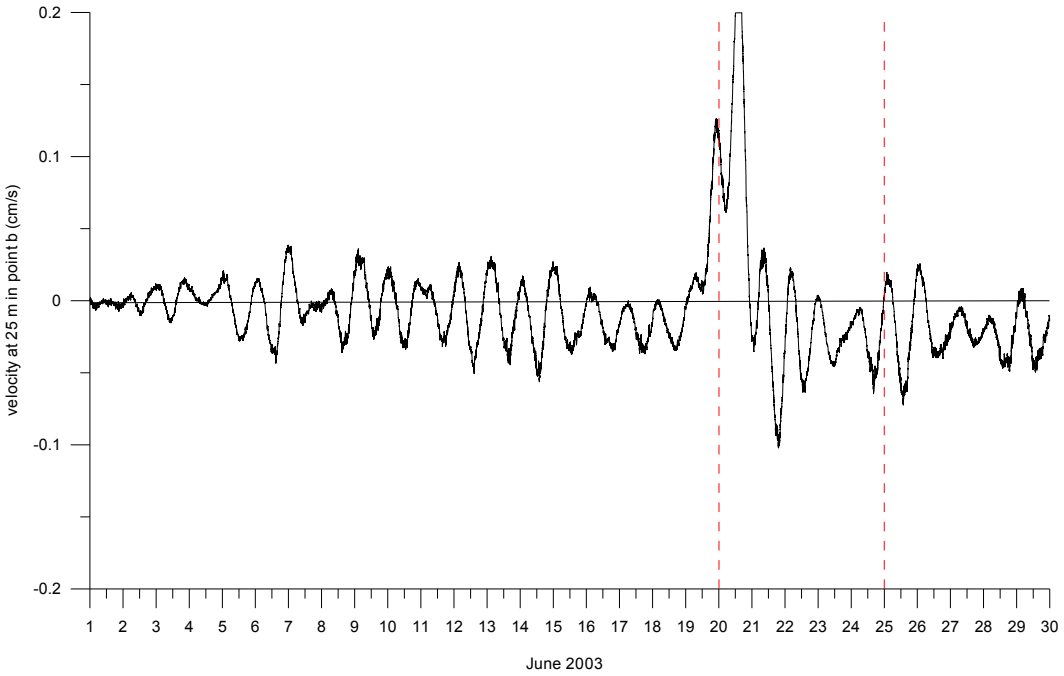

Figure 6.7: Time series of the projected barotropic velocity taken in the mooring location at z = -25 m for Exp. 2.

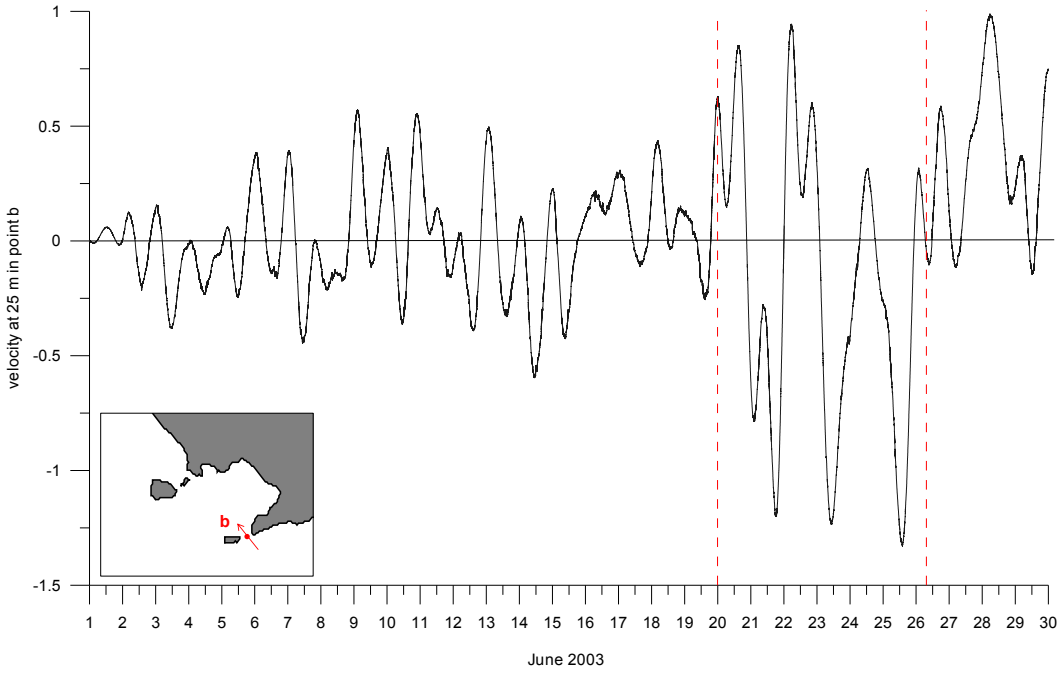

Figure 6.8: Time series of the projected barotropic velocity taken in the mooring location at z = -25 m for Exp. 3.

ECMWF winds. The corresponding time series is given by the red line of Fig. 6.9, which can be compared with the measured current given by the blue line. The two oscillations are in good agreement within the vertical dashed lines both as far as the timing and the amplitude are concerned, except for a $\sim$ 1-day time lag during the ascending phase of the oscillation.

To analyze the importance of the stratification, the "unrealistic" Exp. 5 is carried out. It differs from Exp. 4 only in that the initial stratification is now arbitrarily provided by the February 2009 TSM initialization (Fig. 6.10 shows the two initial stratifications). The resulting projected baroclinic velocity is shown by the green line in Fig. 6.9: the response is now completely unrealistic during the observed oscillation. This is because the Kelvin wave phase speed and cross-shore structure depend crucially on the stratification through the internal Rossby deformation radius R_i; these dynamical features in turn determine the wave evolution. Thus, the unrealistic weakly stratified winter (February 2009) conditions inevitably produce unrealistic flows. This points to the fundamental importance of a correct initialization to achieve a realistic simulation.

Finally, Exp. 6 (Fig. 6.11) is the same as the realistic Exp. 4, but now the simulation covers the two-month period May-June 2003 (with the same June 2003 initialization) with the aim of testing whether a more realistic evolution preceding the crucial event can produce a more realistic oscillation. This is, in fact, the case, as now the modeled oscillation captures the real one even better than Exp. 4 (the 1-day time lag reduces to few hours, see Fig. 6.11). The zooming of the oscillation is shown in Fig. 6.12, in which the same model-data comparison obtained by Pierini et al. (2005) with the model of Pierini et al., 2004(see Fig.s 1.20-1.21) is also shown.

It is interesting to note that a relatively idealized adiabatic three-layer

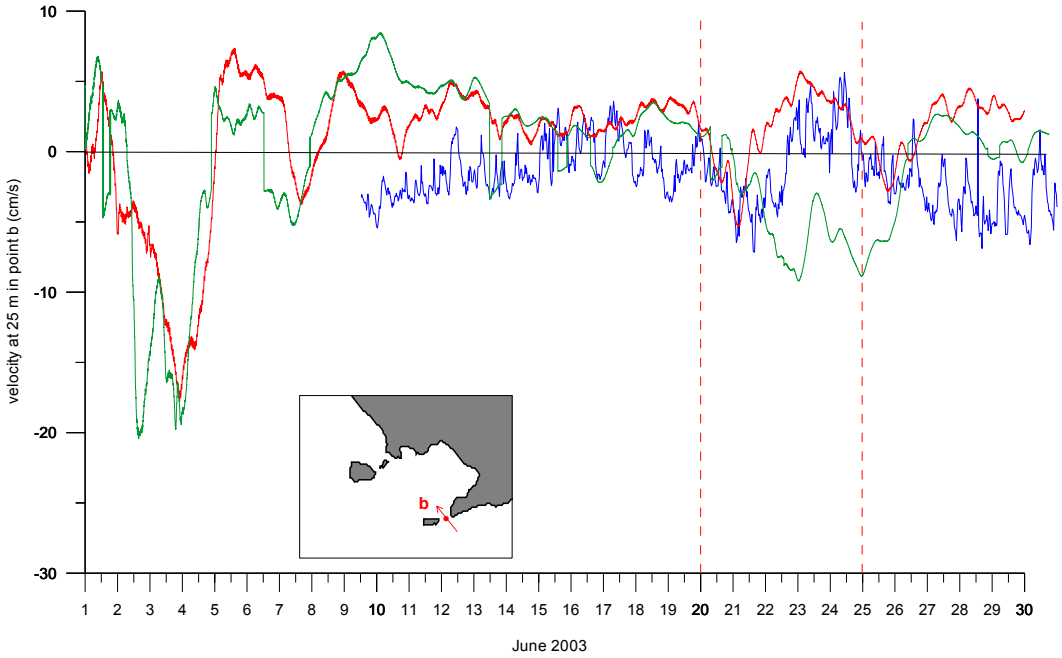

Figure 6.9: Time series of the projected baroclinic velocity taken in the mooring location at z = -25 m for Exp. 4 (red line) and Exp. 5 (green line). The blue line denotes the measured currents.

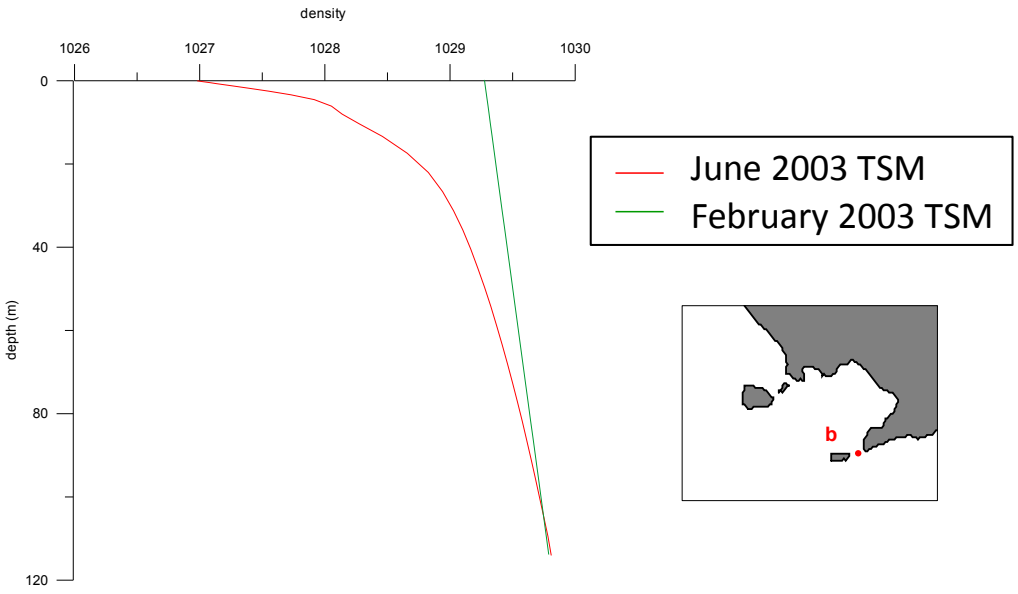

Figure 6.10: Initial stratification in the mooring location for June 2003 (red line, Exp. 4) and February 2003 (green line, Exp. 5).

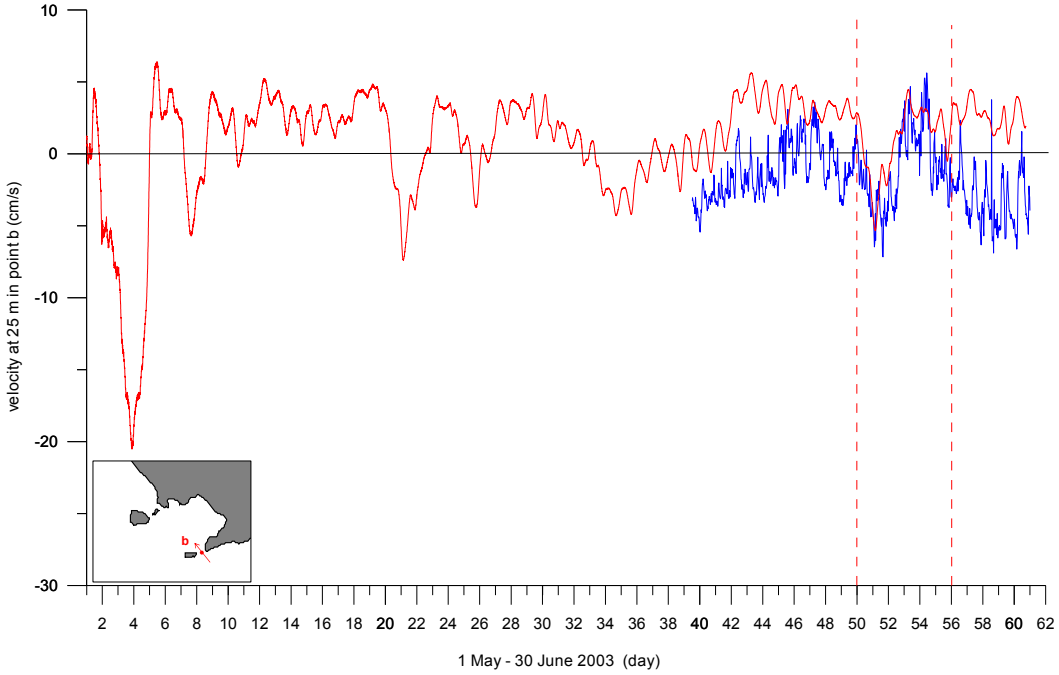

Figure 6.11: Time series of the projected baroclinic velocity taken in the mooring location at z = -25 m for Exp. 6 (red line). The blue line denotes the measured currents.

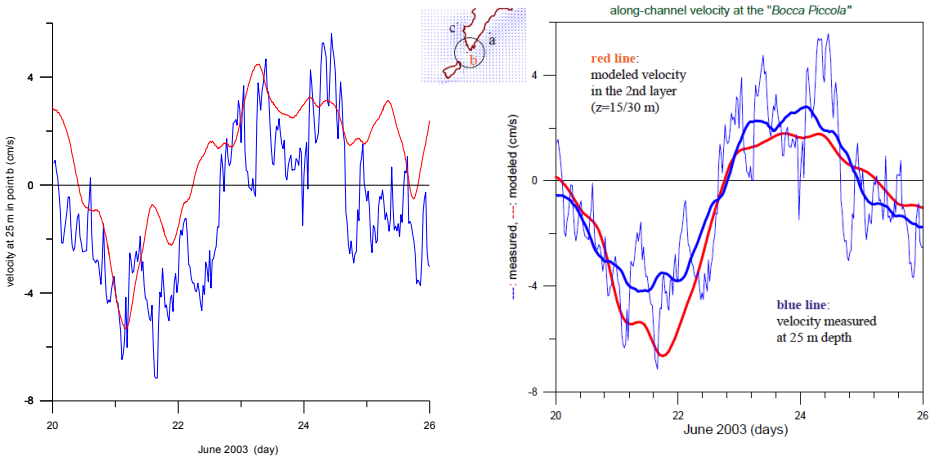

Figure 6.12: Left panel: the red and blue lines are the same as in Fig. 6.10. Right panel: same model-data comparison made with the result of the three-layer shallow water model of Pierini et al. (2005).

shallow water model provides a simulation whose degree of realism is comparable to that of COSM, which is definitely a more sophisticated modeling tool. This suggests that the dynamical feature that shapes this ocean response (the internal Kelvin wave) is very robust, in that it strongly depends on the geometry of the basin but only slightly on the fine structure of the vertical stratification (provided R_i has the correct value, as happened with the model of Pierini et al., 2005; de Ruggiero et al., 2013).

Another interesting conclusion can be drawn by considering that both model simulations were performed with closed boundary conditions along the open boundaries. Although this limitation may appear as a severe drawback of the modeling approach, the locality of the upwelling, and consequent triggering of the internal Kelvin wave is evidently a phenomenon localized on a regional scale, so that the main feature of the oscillation can emerge even without nesting.

6.2 Experimental validation with CODAR data

In this section we present a significant experimental validation of the simulation of November 2010 (section 5.3). That simulation incorporates the most realistic model implementation and, at the same time, allows one to assess -within the limits of the available wind data- the capability of COSMO-SkyMed SAR data to improve coastal circulation modeling.

First of all, the experimental apparatus is now presented. Surface current data in the area of the Gulf of Naples are provided by a HF coastal radar system permitting the real-time, synoptic monitoring of the basin. This system is operated by the Department of Environmental Sciences (DiSAm) of the Universitá degli Studi di Napoli "Parthenope" on behalf of the Centre for

the Analysis and Monitoring of Environmental Risk (AMRA Scarl). Composed of three antennas and a central site, the system (a SeaSonde, manufactured by CODAR Ocean Sensors of Mountain View, California, USA) works in the 25 MHz band, measuring surface currents relative to the first 1 m of the water column. The temporal resolution is 1 h, the spatial resolution is 1 km, while the range is approximately 35 Km from the coast. The original network installed in 2004 comprised two remote stations (in Portici and in Massa Lubrense); in 2008 a third antenna was set up in Castellammare di Stabia; this implementation improved both the spatial coverage and the resolution (Uttieri et al., 2011; Cianelli et al., 2011; Serafino et al., 2012).

The validation compares a snapshot of the surface currents provided by the simulation of section 5.3 with the corresponding field measured by the CODAR apparatus at the same time. The modeled field is that of 20 November 2010 at 6:00 h, and is shown in Fig. 5.15. The maps are limited to the north-western part of the domain (red rectangle of Fig. 5.14), where the difference between the flows obtained from ECMWF and blended wind products differ most, since it is in that window that SAR data are contained. On the other hand, the measured currents are limited to the Gulf of Naples, which is quite far from that area, so this comparison does not allow us to directly validate the effect of SAR winds on the modeled circulation. However, validation of the model implementation can nonetheless be obtained.

The centre panel of Fig. 6.13 shows a zoom of the surface currents obtained on 20 November 2010 at 6:00 h with the nested November 2010 simulation with CSM SAR data described in section 5.3, while the bottom panel shows the same field as observed with CODAR. The strong north-westward flowing jet originating from the Bocca Piccola (and aligned along the Bocca Grande) measured by CODAR is extremely well reproduced by the model;

the anticyclonic overshooting observed past the strait is also present in the simulation. This provides a very significant validation of the model implementation. The circulation inside the gulf, on the contrary, does not show a good model-data comparison. Since the local dynamics is substantially determined by small scale wind features, and since ECMWF winds, due to their limited resolution, are well known to fail to provide correct atmospheric information in that area surrounded by very strong orographic features, such effects could be expected in advance.

It is very interesting to note that the instantaneous circulation in the Gulf of Naples depends crucially on the coupling with the large-scale Tyrrhenian circulation. The upper panel of Fig. 6.13 shows the result of the same simulation relative to the centre panel, but with closed boundary conditions along the open lateral boundaries. Comparison with the upper and centre panels of Fig. 6.13 is striking: the agreement with observations is excellent with nesting and absent without nesting. This stresses to the importance of the nesting procedure for a correct and realistic modeling of our coastal area (although, as we noticed at the end of section 6.1, this is not necessarily true in all cases).

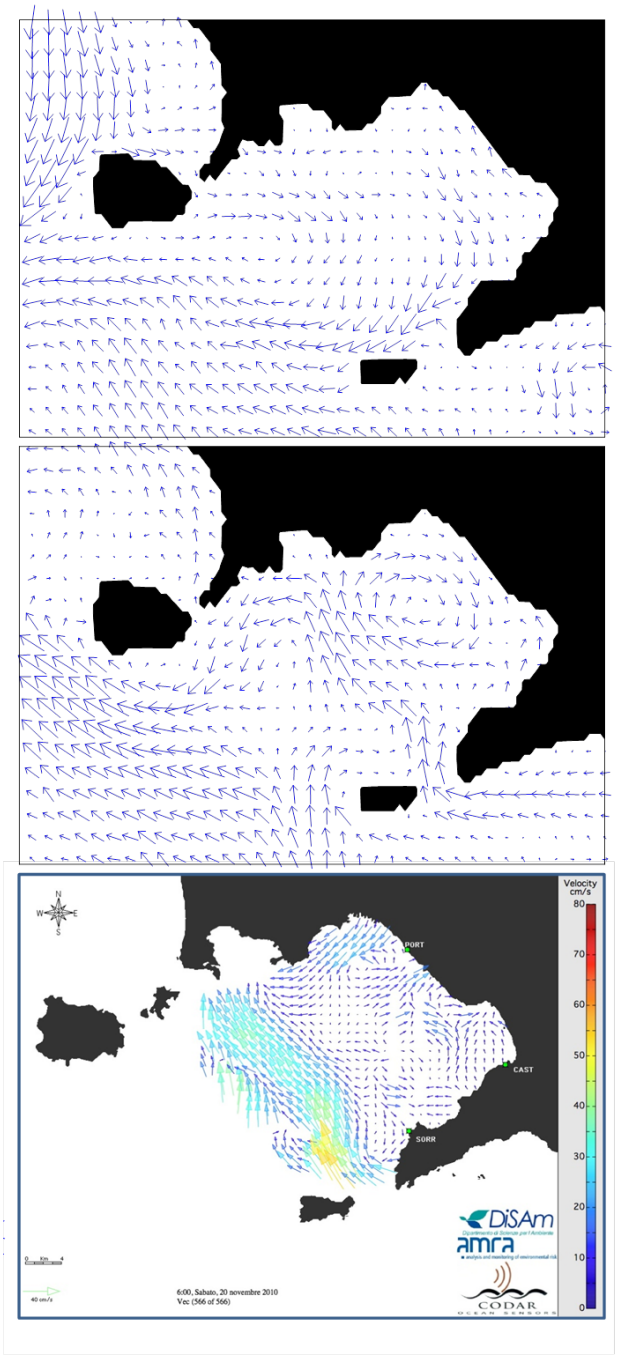

Figure 6.13: Centre panel: zooming over the Gulf of Naples of the map of surface currents (only the arrows at each every 3 grid points along both x and y are shown) on 20 November 2010 at 06:00 h, obtained with the nested November 2010 simulation with CSM SAR data described in section 5.3. Upper panel: same, but without nesting. Bottom panel: map of surface currents measured with CODAR at the same instant (courtesy of Prof. E. Zambianchi and his collaborators).

Conclusion

The main aim of this PhD research was to study some fundamental aspects of the circulation in a wide South Tyrrhenian coastal area that includes the Gulf of Naples. The primitive equation sigma-coordinate POM was implemented with high-resolution in that area, and was nested with a circulation model of the whole Tyrrhenian Sea.

A review of the observational and modelling studies concerning the Tyrrhenian Sea and related coastal areas (Chapter 1) has evidenced the limitations of the previous modeling implementations. The model developed during this PhD research is highly innovative to this respect, since its resolution is very high, the nesting with a Tyrrhenian Sea model is carried out, and experimental validation is performed as well.

The implementation was developed gradually, so that the sensitivity to various model characteristics could be assessed. Comparison between circulation scenarios obtained with and without dynamic boundary conditions along the outer boundaries of the coastal model has evidenced the fundamental role of the large-scale Tyrrhenian circulation in determining the dynamics inside the gulf.

Modeling the wind-driven circulation was the main task of our study. Surface ECMWF analysis wind data have been used throughout, but also wind data obtained from X-band SAR data (of the Italian Space Agency

COSMO-SkyMed satellite constellation) have been used, showing that they provide a potentially valuable tool for improving coastal circulation modeling.

Circulation scenarios typical of different seasons have been simulated. In two cases (June 2003 and November 2010) experimental validation has been successfully performed. In the first case available currentmeter measurements in the Bocca Piccola of Capri (showing a large amplitude oscillation lasting 2 days following a strong meteorological anomaly) have been reproduced quite accurately in our simulations. That signal was interpreted in terms of a baroclinic Kelvin wave propagating northward along the Campania coasts. In the second case, the surface currents obtained by a CODAR system operating in the Gulf of Naples were found in very good agreement with our simulation as far as the flow induced by the large scale Tyrrhenian circulation is concerned. These significant validations insure the correct implementation and the high degree of realism of this modeling tool.

Future developments include: (i) a systematic simulation of the prevailing circulation scenarios corresponding to the different seasons (and consequent construction of the local climatology), (ii) the analysis of local thermohaline effects by imposing also sensible and latent heat fluxes at the air-sea interface, (iii) the analysis of the effect of river discharges in the gulfs, (iv) the development of Lagrangian techniques to describe mass exchange between the gulfs and the open sea.

References of papers related to this PhD research

MONTUORI A., DE RUGGIERO P., MIGLIACCIO M., PIERINI S. and SPEZIE G., (2013), X-band COSMO-SkyMed wind field retrieval, with application to coastal circulation modeling. Ocean Sci., 9, 121-132.

DE RUGGIERO P., (2013), A high-resolution ocean circulation model of the Gulf of Naples and adjacent areas. Il Nuovo Cimento C, submitted (invited paper following a ”Menzione” received as one of the best oral communications presented at the XCVIII National Congress of the Italian Physical Society, 17-21 September 2012, Naples).

DE RUGGIERO P., NAPOLITANO E., IACONO R., PIERINI S., and SPEZIE G., (2013), High-resolution model studies of the circulation in coastal areas of the Tyrrhenian Sea (including the Gulf of Naples). in preparation.

Bibliography

Artale, V., Astraldi, M., Buffoni, G., and Gasparini, G. P. (1994). Seasonal variability in the northern Tyrrhenian Sea. *J. Geophys. Res.*, 99(C7):14127–14138.

Astraldi, M. and Gasparini, G. P. (1992). The seasonal characteristics of the circulation in the North Mediterranean basin and their relationship with the atmospheric-climatic conditions. *J. Geophys. Res.*, 97:9531–9540.

Astraldi, M., Gasparini, G. P., and S., S. (1994). The seasonal and interannual variability in the Ligurian-Provencal Basin. *Coastal and Estuarine Stud.*, 46:3–113.

Bentamy, A., Queffeulou, P., Quilfen, Y., and Katsaros, K. (1999). Ocean surface wind fields estimated from satellite active and passive microwave istruments. *IEEE T. Geosci. Remote*, 37:2469–2486.

Béranger, K., Mortier, L., Gasparini, G. P., Gervasio, L., Astraldi, M., and Crepon, M. (2004). The dynamics of the Sicily Strait: a com-prehensive study from observations and model. *Deep Sea Res. II*, 51:411–440.

Berntsen, J. and Oey, L.-Y. (2010). Estimation of the internal pressure gradient in sigma-coordinate ocean models: comparison of second-, fourth-, and sixth-order schemes. *Ocean Dynamics*, 60:317–330.

Blumberg, A. F. and Mellor, L. G. (1987). A description of a three-dimensional coastal ocean circulation model, in Three-Dimensional Coastal Ocean Models. *A. G. U.*, vol. 4:208.

Carrada, O. C., Hopkins, T. S., Bonaduce, O., Ianora, A., Marino, D., Modigh, M., and Ribera D'alcalá, M. (1980). Variability in the hydrographic and biological features of the Gulf of Naples. *P.S.Z.N.L: Marine Ecology*, 1:105–120.

Chu, P. C. and Fan, C. W. (2001). An accuracy progressive sixth-order finite difference scheme. *J. Atmos. Oceanic Technol.*, 18:1245–1257.

Chu, P. C. and Fan, C. W. (2003). Hydrostatic correction for sigma coordinate ocean models. *J. Geophys. Res.*, 108:3206.

Cianelli, D., Uttieri, M., Buonocore, B., Falco, P., Zambardino, G., and Zambianchi, E. (2011). Dynamics of a very special mediterranean coastal area: the Gulf of Naples. *In: Columbus F. (Editor) Mediterranean Ecosystems: Dynamics, Management and Conservation. Nova Science Publishers, Inc, New York.*

De Maio, A., Moretti, M., Sansone, E., Spezie, G., and Vultaggio, M. (1979). Dinamica delle acque nel Golfo di Napoli. *Atti del Convegno Scientifico Nazionale P. F. Oceanografia e Fondali Marini II*, pages 1033–1045.

De Maio, A., Moretti, M., Sansone, E., Spezie, G., and Vultaggio, M. (1981). Circolazione costiera. Analisi dinamica e idrologica di una situazione osservata nel Golfo di Napoli. *Annali Ist. Univ. Nav.*, 49:1–305.

De Maio, A., Moretti, M., Sansone, E., Spezie, G., and Vultaggio, M. (1983). Dinamica delle acque nel Golfo di Napoli e adiacenze. Risultati ottenuti dal 1977 al 1980. *Annali Ist. Univ. Nav.*, 51:1–58.

De Maio, A., Moretti, M., Sansone, E., Spezie, G., and Vultaggio, M. (1985). Outline of marine currents in the Bay of Naples and some considerations on pollutant transport. *Il Nuovo Cimento*, 3(C8):955–969.

de Ruggiero, P. (2013). A high-resolution ocean circulation model of the gulf of naples and adjacent areas. *Il Nuovo Cimento C, submitted (invited paper following a "Menzione" received as one of the best oral communications presented at the XCVIII National Congress of the Italian Physical Society, 17-21 September 2012, Naples)*.

de Ruggiero, P., Napolitano, E., Roberto, I., Pierini, S., and Spezie, G. (2013). High-resolution model studies of the circulation in coastal areas of the tyrrhenian sea (including the gulf of naples). *in preparation*.

Düing, W. (1965). Strömungsverhältnisse im Golf von Neapel. *Pubbl. Staz. Zool. Napoli*, 34:256–316.

Ezer, T. (1994). On the interaction between the Gulf Stream and the new England seamount chain. *J. Phys. Oceanogr.*, 24:191–204.

Ezer, T., Arango, H., and Shchepetkin, A. F. (2002). Developments in terrain following ocean models: Intercomparisons of numerical aspects. *Ocean Model.*, 4:249–267.

Ezer, T. and Mellor, G. L. (1992). A numerical study of the variability and the separation of the Gulf Stream induced by surface atmospheric forcing and lateral boundary flows. *J. Phys. Oceanogr.*, 22:660–682.

Flather, R. A. (1976). A tidal model of the northwest European continental shelf. *Mém. Soc. R. Sci. Liége*, 6:141–164.

Fletcher, C. A. J. (1987). Computational tecniques for fluid dynamics. *Springer-Verlag*, Vol. 1 and 2.

Gabersek, S., Sorgente, R., Natale, S., Ribotti, A., Olita, A., Astraldi, M., and Borghini, M. (2007). The Sicily Channel regional model forecasting system: initial boundary conditions sensitivity and case study evaluation. *Ocean Sci.*, 3:31–41.

Galperin, B. and Mellor, G. L. (1990a). A time-dependent, three-dimensional model of the delaware bay and river. Part i: Description of the model and tidal analysis. *Estuarine Coastal Shelf Sci.*, 31:231–253.

Galperin, B. and Mellor, G. L. (1990b). A time-dependent, three-dimensional model of the delaware bay and river. Part ii: Three-dimensional flow fields and residual circulation. *Estuarine Coastal Shelf Sci.*, 31:255–281.

Gary, J. M. (1973). Estimate of truncation error in transformed coordinate, primitive equation atmospheric models. *J. Atmos. Sci.*, 30:223–233.

Gravili, D., Napolitano, E., and Pierini, S. (2001). Barotropic aspects of the dynamics of the Gulf of Naples (Tyrrhenian Sea). *Continental Shelf Res.*, 25:711–728.

Grieco, L., Tremblay, L., and Zambianchi, E. (2005). A hybrid approach to transport processes in the Gulf of Naples: an application to phytoplankton and zooplankton population dynamics. *Continental Shelf Res.*, 25:711–728.

Haidvogel, D., Beckman, A., and Hedstrom, K. (1991). Dynamical simulations of filament formation and evolution in the coastal transition zone. *J. Geophys. Res.*, 96:15017–15040.

Haney, R. (1991). On the pressure gradient force over steep topography in sigma coordinate ocean models. *J. Phys. Oceanogr.*, 21:610–619.

Hapgood, H. W. (1959). Hydrographic observations in the Bay of Naples (Golfo di Napoli). *Pubbl. Staz. Zool. Napoli*, 31:337–371.

Hopkins, T. S. (1988). Recent observations on the intermediate and deep water circulation in the Southern Tyrrhenian Sea. *In: Océanographie pélagique méditerranéenne*, pages 41–50.

Hopkins, T. S. (2001). Currents system in the Mediterranean Sea. *In: Steele J. H. (Ed.), Encycl. Ocean Sci., Academic press, Oxford*, pages 605–612.

Iacono, R., Napolitano, E., Marullo, S., Artale, V., and Vetrano, A. (2012). Seasonal variability of theTyrrhenian Sea surface circulation as assessed by Altimeter data. *submitted*.

Jackson, C. R. and Apel, J. R. (2004). Synthetic Aperture Radar (SAR) marine user's manual, National Oceanic and Atmospheric Administration (NOOA). *Washington, DC.*

Janjic, Z. I. (1997). Pressure gradient force and advection scheme used for forecasting with steep and small-scale topography. *Contrib. Atmos. Phys.*, 50:186–199.

Kantha, L. H. and Clayson, C. (1994). An improved mixed layer model for geophysical applications. *J. Geophys. Res*, 99.

Kliem, N. and Pietrzak, J. (1999). On the pressure gradient error in sigma coordinate ocean models: a comparison with a laboratory experimenty. *J. Geophys. Res.*, 104:29781–29799.

Krivosheya, V. G. and Ovchinnikov, I. M. (1973). Peculiarities in the geostrophic circulation of the waters of the Tyrrhenian Sea. *J. Geophys. Res.*, 13:822–827.

Lascaratos, A. (1993). Estimation of deep and intermediate water mass formation rates in the Mediterranean Sea. *Deep Sea Res. II*, 40:1327–1332.

Lee, P. H. Y., Barter, J. D., Beach, K. L., Hindman, C. L., Lake, B. M., Rungaldier, H., Shelton, J. C., Williams, A. B., Yee, R., and Yuen, H. C. (1995). X band microwave backscattering from ocean waves. *J. Geophys. Res.*, 100:2591–2611.

Madala, R. V. and Piacsek, S. A. (1977). A semi-implicit numerical model for baroclinic oceans. *J. Comput. Phys.*, 23:167–168.

Maraschiello, P., McWilliams, J. C., and Shchepetkin, A. (2001). Open boundary conditions for long-term integration of regional oceanic models. *Ocean Model.*, 3:1–20.

Mellor, G. L. (2004). Users guide for a three dimensional, primitive equation, numerical ocean model. *Technical report, Princeton University*.

Mellor, G. L., Ezer, T., and Oey, L.-Y. (1994). The pressure gradient conundrum of sigma coordinate ocean model. *J. Atmos. Ocean Technol.*, 11:1122–1131.

Mellor, G. L. and Wang, X. H. (1996). Pressure compensation and the bottom boundary layer. *J. Phys. Oceanogr.*, 26:2214–2222.

Mellor, G. L. and Yamada, T. (1982). Development of a turbulence closure model for geophysical fluid problems. *Rev. Geophys. Space Phys.*, 20:851–875.

Menna, M. (2007). Misure di correnti superficiali nel golfo di napoli eseguite con radar costiero. *Tesi di Dottorato in Scienze e Ingegneria del Mare, Universitá di Napoli Federico II, Napoli*.

Menna, M., Mercantini, M., Uttieri, M., Buonocore, B., and Zambianchi, E. (2008). Wintertime transport processes in the Gulf of Naples investigated by HF radar measurements of surface currents. *Il Nuovo Cimento*, 30C:605–622.

Mesinger, F. (1982). On the convergence and error problems of the calculation of the pressure gradient force in sigma coordinate models. *Geophys. Astrophys. Fluid Dyn.*, 19:105–117.

Migliaccio, M. and Reppucci, A. (2006). A review of sea wind vector retrievals by means of microwave remote sensing. *Proceedings of the European Microwave Association*, 2:136–140.

Millot, C. (1987). Circulation in the western Mediterranean Sea. *Oceanol. Acta*, 10:143–149.

Molcard, A., Pinardi, N., Iskandarani, M., and Haidvogel, D. (2002). Wind driven general circulation of the Mediterranean Sea simulated with a spectral element ocean model. *Dynam. Atmos. Oceans.*, 35:97–130.

Montuori, A., de Ruggiero, P., Migliaccio, M., Pierini, S., and Spezie, G. (2013). X-band COSMO-SkyMed wind field retrieval, with application to coastal circulation modeling. *Ocean Sci.*, 9:121–132.

Moretti, M., Sansone, E., Spezie, G., and De Maio, A. (1977). Alcuni aspetti del movimento delle acque nel golfo di Napoli. *Annali Ist. Univ. Nav.*, 46:207–217.

Moretti, M., Spezie, G., and Vultaggio, M. (1985). Observation of near inertial period oscillations in the Gulf of Naples. *Bollettino di Oceanologia Teor. Appl.*, 3:145–152.

Napolitano, E., Iacono, R., and Marullo, S. (2013). The 2009 surface and intermediate circulation of the Tyrrhenian Sea as assessed by an operational model. *in: The Mediterranean Sea: Temporal Variability and Spatial Patterns, AGU Book Series, Borzelli G., Malanotte-Rizzoli P., Gacic M., and Lionello P. (Editors), in press.*

Napolitano, E., Sannino, G., Artale, V., and Marullo, S. (2003). Modeling the baroclinic circulation in the area of the Sicily channel: The role of stratification and energy diagnostics. *J. Geophys. Res.*, 108(C7).

Nunziata, F., Gambardella, A., and Migliaccio, M. (2007). A simulator for SAR sea surface waves imaging. *in: Proceedings of IEEE Int. Geosci. Remote Sensing. 2007, Barcellona, Spain, 23-27 July2007*, pages 786–789.

Oddo, P., Adani, M., Pinardi, N., Fratianni, C., Tonani, M., and Pettenuzzo, D. (2009). A nested Atlantic-Mediterranean Sea general circulation model for operational forecasting. *Ocean Sci.*, 5:461–473.

Oey, L.-Y., Mellor, G. L., and Hires, R. I. (1985a). A three-dimensional simulation of the Hudson-Raritan estuary. *J. Phys. Oceanogr.*, 15:1676–1692.

Oey, L.-Y., Mellor, G. L., and Hires, R. I. (1985b). A three-dimensional simulation of the Hudson-Raritan estuary. Part i: Description of the model and model simulations. *J. Phys. Oceanogr.*, 15:1693–1709.

Perusini, V., Purini, R., Moretti, M., and De Maio, A. (1992). Modelli di circolazione costiera. primi risultati per la costa campana. *Annali Ist. Univ. Nav.*, LIX:65–76.

Pierini, S. (1996). Topographic Rossby modes in the Strait of Sicily. *J. Geophys. Res.*, 101:6429–6440.

Pierini, S. (2003). A model of the wind-driven seasonal variability in the tropical North Pacific, with validation through altimeter data. *J. Geophys. Res.*, 33:2156–2172.

Pierini, S., Ferretti, R., Veneziani, C., and Visconti, G. (2004). Eulerian and lagrangian model studies of the wind-driven circulation in the Gulf of Naples (Tyrrhenian Sea). *E.G.U. General Assembly, Geophys. Res. Abs.*, 6:01548.

Pierini, S., Roselli, L., and Spezie, G. (2005). Evidence of coastal trapped waves propagating along a Southern Tyrrhenian coastal zone: modeling results and validation with currentmeter measurements. *E.G.U. General Assembly, Geophys. Res. Abs.*, 7:02058.

Pierini, S. and Rubino, A. (2001). Modeling the oceanic circulation in the area of the Strait of Sicily: the remotely-forced dynamics. *J. Phys. Oceanogr.*, 31:1397–1412.

Pierini, S. and Simioli, A. (1998). A wind-driven circulation model of the Tyrrhenian Sea area. *J. Mar. Sys.*, 18:161–178.

Robinson, A. R., Sellschopp, J., Warn-Varnas, A., Leslie, W. G., Lozano, C. J., Haley, P. J., Anderson, L. A., and Lermusiaux, P. F. J. (2001). The Atlantic-Ionian stream. *J. Mar. Sys.*, 20:129–156.

Roselli, L. (2003). Interazioni dinamiche alla Bocca Piccola di Capri. *Tesi di Dottorato in Scienze e Ingegneria del Mare, Universitá di Napoli Federico II, Napoli*.

Roselli, L., Manno, C., and Spezie, G. (2007). Inertial oscillations and particle flux interactions in a marine protected area in Gulf of Naples. *Chemis. and Ecology*, 23:177–190.

Rousseau, D. and Pham, H. L. (1971). Premiers resultats d'un model de prevision numerique a courte echeance sur l'Europe. *La Meteorologie*, 20:1–12.

Sannino, G., Bargagli, A., and Artale, V. (2004). Numerical modeling of the semidiurnal tidal exchange through the Strait of Gibraltar. *J. Geophys. Res.*, 109:C05011.

Schroeder, K., Borghini, M., Cerrati, G., Difesca, V., Delfanti, R., Santinelli, C., and Gasparini, G. P. (2008). Multiparametric mixing analysis of the deep waters in the western Mediterranean Sea. *Chem. Ecol.*, 24:47–56.

Serafino, F., Lugni, C., Ludeno, G., Arturi, D., Uttieri, M., buonocore, B., Zambianchi, E., Budillon, G., and Soldovieri, F. (2012). REMOCEAN: a flexible X band radar system for sea state monitoring and surface current estimation. *Geoscience and Remote Sensing Letters*.

Shchepetkin, A. and McWilliams, J. (2003). A method for computing horizontal pressure-gradient force in an oceanic model with a non-aligned vertical coordinate. *J. Geophys. Res.*, 108:3090.

Signell, R. P., Carniel, S., Cavaleri, L., Chiggiato, J., Doyle, J., Pullen, J., and Sclavo, M. (2005). Assessment of wind quality for oceanographic modeling in semi-enclosed basins. *J. Mar. Sys.*, 53:217–233.

Simons, T. J. (1974). Verification of numerical models of lake Ontario, Part 1. Circulation in spring and early summer. *J. Phys. Oceanogr.*, 4:507–523.

Smagorinsky, J. (1963). General circulation experiments with primitive equations: I. The basic experiment. *Mon. Weather Rev.*, 91:99–164.

Song, Y. (1998). A general pressure gradient formulation for ocean models. Part I: scheme design and diagnostic analysis. *Mon. Weather Rev.*, 126:3213–3230.

Song, Y. and Wright, D. (1998). A general pressure gradient formulation for ocean models. Part II: energy, momentum and bottom torque consistencys. *Mon. Weather Rev.*, 126:3231–3247.

Sparnocchia, S., Gasparini, G. P., Astraldi, M., Borghini, M., and Pistek, P. (1999). Dynamics and mixing of the Eastern Mediterranean outflow in the Tyrrhenian basin. *J. Mar. Sys.*, 20:301–317.

Stelling, G. and Van Kester, J. (1994). On the approximation of horizontal gradients in sigma coordinates for bathymetry with steep bottom slopes. *Int. J. Numer. Methods Fluids*, 18:915–935.

Uttieri, M., Cianelli, D., Nardelli, B. B., Buonocore, B., Falco, P., Colella, S., and Zambianchi, E. (2011). Multiplatform observation of the surface circulation in the Gulf of Naples (Southern Tyrrhenian sea). *Ocean Dyn.*, 61:779–796.

Vallis, J. K. (2006). Atmospheric and oceanic fluid dynamics. *Cambridge University Press*.

Vetrano, A., Napolitano, E., Iacono, R., Schroeder, K., and Gasparini, G. P. (2010). Tyrrhenian Sea circulation and water mass fluxes in spring 2004: Observations and model results. *J. Geophys. Res.*, 115:C06023.

Wendicke, F. (1916). letter. *Mitth. Zool. Stat. Neapel*, 22:229–362.

Yang, X., Li, X., Pichel, W. G., and Li, Z. (2011). Comparison of ocean surface winds from ENVISAT ASAR, MetOp ASCAT Scatterometer, buoy measurements, and NOGAPS Model. *IEEE Geosci. Remote*, 49:4743–4750.

Zavatarelli, M. and Pinardi, N. (2003). The Adriatic Sea modelling system: a nested approach. *Ann. Geophys.*, 21:345–364.

Acknowledgements

The authoress would like to thank her research supervisor, Prof. Stefano Pierini, for his sharp thinking, constructive criticism and continued support during the course of this research project, and her co-tutor, Prof. Giancarlo Spezie, for his valuable support provided through the PROMETEO Project of the University of Naples Parthenope. She would also like to thank Prof. Enrico Zambianchi for having kindly provided a CODAR map of surface currents used in the course of model validation. She is also very grateful to Dr. Ernesto Napolitano and Dr. Roberto Iacono for their scientific and technical advice and for many insightful discussions and suggestions.

She will forever be thankful to Giovanni Sgubin, Pasquale Castagno, Claudia Ferrara and Renato, Gianfranco Quattrocchi, Giovanni Liguori, Manuela Sansiviero, Anna Fragliasso and Giuseppe Aulicino, colleagues and all her friends. She also warmly thanks to her family, especially her grandmother and Ester, for always supporting her and believing in her. Finally, she thanks to Angelo because "...I know my heart can stay with my love, it's in the hands of my love, and my love does it good, only my love does it good to me..." [Paul McCartney - My Love].